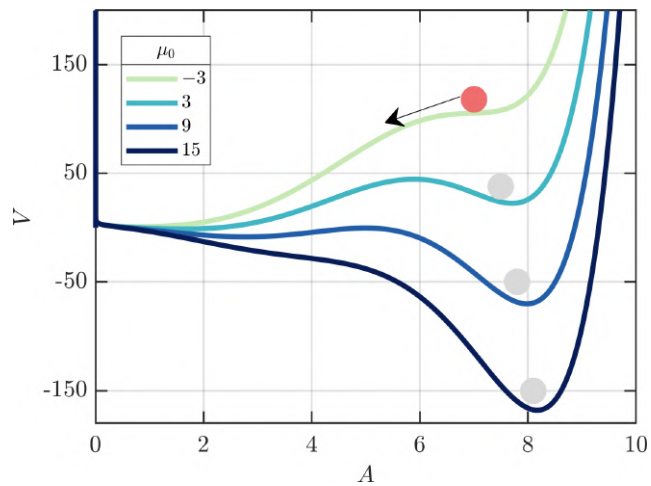




DEPARTMENT OF AEROSPACE ENGINEERING
INDIAN INSTITUTE OF TECHNOLOGY MADRAS
CHENNAI – 600036

Transitions to high amplitude oscillatory instabilities in aero-thermoacoustic systems



A Thesis

Submitted by

RAMESH SIDDARUDA BHAVI

For the award of the degree

Of

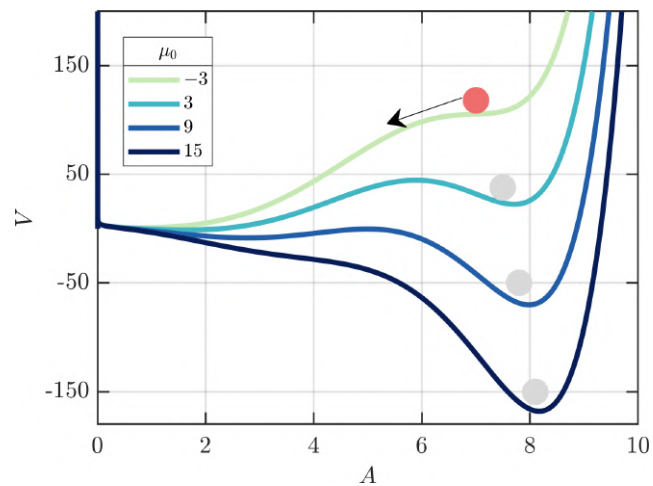
DOCTOR OF PHILOSOPHY

December 2024



DEPARTMENT OF AEROSPACE ENGINEERING
INDIAN INSTITUTE OF TECHNOLOGY MADRAS
CHENNAI – 600036

Transitions to high amplitude oscillatory instabilities in aero-thermoacoustic systems



A Thesis

Submitted by

RAMESH SIDDARUDA BHAVI

For the award of the degree

Of

DOCTOR OF PHILOSOPHY

December 2024

स॒ह ना॑वतु । सह नो॑ भुनक्तु । saha nāvavatu | saha nau bhunaktu |
स॒ह वी॒र्यं॑ करवावहे । saha vīryam karavāvahai |
ते॒ज॒स्विना॒वधी॑तमस्तु॒ मा वि॑द्विष॒वहै॑ ॥ tejasvināvadhītamastu mā vidviṣavahai ॥
ॐ शान्तिः॑ शान्तिः॑ शान्तिः॑ ॥ om śāntiḥ śāntiḥ śāntiḥ ॥

*Let us together be protected and let us together be
nourished by God.*

*Let us together join our mental forces in strength for the
benefit of humanity.*

*Let our efforts at learning be luminous and filled with
joy, and endowed with the force of purpose. Let us never
be poisoned with the seeds of hatred for anyone.*

Let there be peace and serenity in all the three universes.

– Taittiriya Upanishad , Chapter 2, Verse 1

*To my parents
For their support and sacrifices*

THESIS CERTIFICATE

This is to undertake that the Thesis titled **TRANSITIONS TO HIGH AMPLITUDE OSCILLATORY INSTABILITIES IN AERO-THERMOACOUSTIC SYSTEMS**, submitted by me to the Indian Institute of Technology Madras, for the award of **Doctor of Philosophy**, is a bona fide record of the research work done by me under the supervision of **Dr. R. I. Sujith**. The contents of this Thesis, in full or in parts, have not been submitted to any other Institute or University for the award of any degree or diploma.

In order to effectively convey the idea presented in this Thesis, the following work of other authors or sources was reprinted in the Thesis with their permission:

1. Figures 2.1 : Image from Ananthkrishnan *et al.* (1998). Reproduced with permission from Elsevier Ltd.
2. Figures 2.2 : Image from Nair *et al.* (2014). Reproduced with permission from Cambridge University Press.
3. Figures 2.3 : Image from Godavarthi *et al.* (2020). Reproduced with permission from AIP Publishing House.

Chennai 600036

Ramesh Siddaruda Bhavi

Date: December 2024

Prof. R. I. Sujith
Research advisor
D. Srinivasan Institute Chair Professor
Department of Aerospace Engineering
IIT Madras

LIST OF PUBLICATIONS

I. REFEREED JOURNALS BASED ON THESIS

1. **Bhavi, R. S.**, Pavithran, I., Roy, A., and Sujith, R. I. (2023). Abrupt transitions in turbulent thermoacoustic systems. *Journal of Sound and Vibration*, **547**, 117478.
2. **Bhavi, R. S.**, Pavithran, I., and Sujith, R. I. (2024). Dynamical states associated with the shift in whistling frequency in aeroacoustic system. *Journal of Sound and Vibration*, **592**, 118606.
3. **Bhavi, R. S.**, S. Sudarsanan, M. Raghunathan, A. Bhaskaran, and Sujith, R. I. (2024). Canard explosions in turbulent thermo-fluid systems. *Chaos: An Interdisciplinary Journal of Nonlinear Science*, **34**, 103133.

II. REFEREED JOURNALS (others)

1. Singh, S., **Bhavi, R. S.**, Raghunath, M. P., Bhaskaran, A., Mishra, P., Chaudhuri, S., and Sujith, R. I. (2024). Intermittency transition to azimuthal instability in a turbulent annular combustor. *International Journal of Spray and Combustion Dynamics*, **16(3)**, 119136.

III. PRESENTATIONS IN CONFERENCES

1. **Bhavi, R. S.**, Pavithran, I., Roy, A., and Sujith, R. I., Study of secondary bifurcations in turbulent thermoacoustic systems. *Conference on Nonlinear Systems and Dynamics*, (2022).
2. **Bhavi, R. S.**, Pavithran, I., Roy, A., and Sujith, R. I., Abrupt transitions in turbulent thermoacoustic systems. *7th International Conference on Complex Dynamical Systems and Applications*, (2024).
3. **Bhavi, R. S.**, S. Sudarsanan, M. Raghunathan, A. Bhaskaran, and Sujith, R. I. (2024), Canards: Continuous rapid transitions in turbulent combustors. *20th Conference on Complex Systems*, (2024).

ACKNOWLEDGEMENTS

I am ever indebted to my parents for the support and sacrifices they have made for the journey I chose.

I am grateful to Prof. R. I. Sujith for his guidance and for helping me learn the pursuit of research and professional skills. It is his work style and the philosophy which he clings to that inspire me to take a purposeful research career. His guidance has helped me in the development of my overall personality. My humble thanks for the helpful support from the head of the department, Dr. H. S. N. Murthy, and the doctoral committee members—Dr. Srinivasan K., Dr. Sunetra Sarkar, Dr. Nagabhushana Rao V.

I sincerely thank my seniors Dr. Induja Pavithran, Dr. Amitesh Roy, Dr. Praveen Kasthuri, and Dr. Manikanadan Raghunathan for helping me understand every aspect of what we pursue in research. I would like to thank labmates Dr. Samarjeet Singh, Dr. Ankit Sahaya, Dr. Abhishek Kushwaha, Shri Vignesh K., and Jayesh M. Dhadphale for their helpful suggestions in my research. There is always a joyful curiosity and eagerness when it comes to discussions in complex systems in the lab, and I thank the juniors for influencing me with such an inspiring attitude; thanks to Shruti Tandon, Beeraiah Thonti, Rohit, and Sanket Ambedkar. My special thanks to Sivakumar for sharing his PhD journey with me and standing on my behalf for all the ups and downs.

Thanks to all my juniors, Pruthiraj, Sandra, Logesh, Athira, Arya and Praveenkumar, for their helpful insights in experiments and managing lab work. Learning is more joyful when we have technical arguments and debates, and I was fortunate to get this atmosphere of learning from all the B. Tech and Masters students in the lab. I am grateful to all those students whom I met in my PhD journey: Alan J, Sneha Srikanth, Aswin Balaji, Aneesh Sreevasthav, Nidhi Sonwane, Andrea, Manaswini, Shubham Dhadal, Rohan Nakade and Siddharth. I thank Dr. Anupam, Dr. Somnath, Dr. Ankan, Dr. Satish and Dr. Gaurav

for their helpful advice on turbulence, combustion dynamics and dynamical systems. Experiments are a major part of my Ph.D., and I am very grateful to the technical staff, Midhun, Anand, Thilagaraj, Anaswara, Sruthibhai, Prasanna and Ariakutty for their support and discussions. I am thankful to the executive secretaries Jabasteena, Shanmugapriya and Jegetha for their helpful support in lab work and documentation. I am thankful to Sudha Akka, Varun sir and all my MS batch mates for the help that I have received from them. Finally, I am grateful to the Department of Aerospace, IIT Madras, for providing a beautiful learning experience on campus.

ABSTRACT

KEYWORDS Thermoacoustic instability; Aeroacoustic instability; Intermittency; Limit cycle oscillations; Abrupt transitions; Fokker-Planck equation; Canard explosions; Synchronization theory; Phenomenological modelling; Nonlinear dynamics

Pleasant sound from a wind instrument, such as a flute, results from self-sustained periodic oscillations arising from the interactions between an acoustic source and the acoustic field. However, such oscillations cause catastrophic damage in engineering systems such as, gas transport systems, combustors of rockets and land-based gas turbine engines. These high amplitude oscillations correspond to the state of thermoacoustic instability in combustors and are caused due to positive feedback between the fluctuating heat release rate from the burning fuels and the acoustic field. Similarly, in large segmented solid rocket motors, the positive feedback between the turbulent flow of hot gases passing through the channel of segments and the acoustic field leads to aeroacoustic instability. These oscillatory instabilities cause structural damage, reduce performance, and even cause complete operational failure of the entire system. In turbulent combustors, past studies were focused on the gradual transitions to the state of oscillatory instability via the state of intermittency. Most recently, the discovery of abrupt transitions in turbulent reactive flow systems has been a highlight, which is a contrasting scenario of a gradual transition. At certain conditions, the system abruptly transits to the state of oscillatory instability when a control parameter, such as fuel flow rates in gas turbines, is varied. Thus, it is crucial to understand the underlying mechanism of such transitions to forewarn about impending oscillatory instabilities.

Using a low-order stochastic thermoacoustic model, we show that the reported abrupt transitions occur when an initially stable, supercritical limit cycle becomes unstable, leading to a secondary bifurcation to a large amplitude limit cycle solution. Through

amplitude reduction, we analyze the underlying potential functions affecting the stability of the observed dynamical states. We make use of the Fokker-Planck equation, reducing the effect of stochastic fluctuations on subcritical and secondary bifurcation. We conclude that a high enough intensity of stochastic fluctuations, which transforms a subcritical bifurcation into an intermittency-facilitated continuous transition, may have little effect on the abrupt nature of secondary bifurcation. Our findings imply the high likelihood of abrupt transitions in turbulent combustors possessing higher-order nonlinearities where turbulence intensities are lower compared to the large amplitude limit cycle solution.

Upon further investigation of sudden transitions at different experimental conditions in turbulent combustors, we discovered canard explosions where we observed a continuous bifurcation with a rapid rise in the amplitude of the fluctuations within a narrow range of control parameters. The observed transition is facilitated via a state of bursting, consisting of the epochs of large amplitude periodic oscillations amidst epochs of low amplitude periodic oscillations. The amplitude of the bursts is higher than the amplitude of the bursts of intermittency state in a conventional gradual transition, as reported in turbulent reactive flow systems. Using the model and experimental results, we explain that the large amplitude bursts occur due to the slow-fast dynamics at the bifurcation regime of the canard explosion.

We further investigate the similarity of these transitions to oscillatory instabilities in an aeroacoustic system. Self-sustained aeroacoustic oscillations are perceived as a whistle. The whistling corresponds to the state of limit cycle oscillations (LCO) in dynamical systems theory. An aeroacoustic system exhibits different dynamical states when the bulk flow velocity is varied as a control parameter. Previous studies have shown that as a control parameter varies, the whistling frequency shifts in an aeroacoustic system having a flow through orifices. We show that such a change in frequency occurs via three different scenarios— (1) a direct transition between two LCOs as an abrupt transition, (2) via a state of intermittency, and (3) via a state of aperiodicity. In the current aeroacoustic

system, the abrupt transition between the LCOs is manifested as a bursting behaviour where the amplitude of the acoustic pressure fluctuations abruptly switches between the high and low-amplitude LCOs. Further, we use synchronisation theory to investigate the coupled behaviour of the velocity (u') and the acoustic pressure (p') fluctuations during the different dynamical states. Finally, our findings imply that u' and p' exhibit phase synchronisation (PS) during the state of LCO, corresponding to whistling. In contrast, u' and p' are desynchronised during the state of aperiodicity, corresponding to stable operation.

CONTENTS

	Page
ACKNOWLEDGEMENTS	i
ABSTRACT	iii
LIST OF TABLES	xi
LIST OF FIGURES	xiii
GLOSSARY	xxiii
ABBREVIATIONS	xxv
NOTATION	xxvii
CHAPTER 1 INTRODUCTION	1
1.1 Thermoacoustic systems	1
1.1.1 Thermoacoustic instability	2
1.1.2 Traditional approach for analysis of thermoacoustic instability	3
1.1.3 Dynamical systems and complex systems approach	5
1.1.4 Dynamics of turbulent combustors	8
1.1.5 Nonlinear oscillator models to describe thermoacoustic system	9
1.1.6 Noise-induced oscillations in thermoacoustic systems	10
1.2 Dynamics of Aeroacoustic systems	12
1.2.1 Aeroacoustic systems under the purview dynamical systems theory	15
1.3 Motivations and resolutions	16
1.4 Objectives of the work	20
1.5 Overview of the thesis	21
CHAPTER 2 METHODS AND ANALYSIS TO STUDY DYNAMICAL SYSTEMS	23
2.1 Mathematical model for transitions in thermoacoustic systems	23
2.1.1 Derivation of slow flow amplitude and phase evolution equations	28
2.1.2 Stochastic averaging of the slow flow equations	30
2.2 Recurrence Analysis	36
2.2.1 Recurrence quantification analysis (RQA)	37
2.3 Synchronisation analysis	39
2.3.1 Joint recurrence matrix	41
2.3.2 Probability of recurrence	42

CHAPTER 3	EXPERIMENTAL SETUPS AND DIAGNOSTICS	45
3.1	Thermoacoustic systems	45
3.1.1	Backward facing step combustor configurations	46
3.1.2	Annular combustor	48
3.2	Aeroacoustic system	50
3.3	Acoustic decay rate	52
CHAPTER 4	ABRUPT TRANSITIONS IN TURBULENT THERMOACOUSTIC SYSTEMS	55
4.1	Experimental observation of abrupt secondary bifurcations	56
4.2	Slow flow representation of the stochastic system	59
4.3	Stationary solution of the Fokker-Planck equation	61
4.4	Effect of noise levels on the transition	62
4.4.1	Potential landscape of the secondary bifurcation	65
4.5	Concluding remarks	68
CHAPTER 5	CONTINUOUS RAPID TRANSITIONS IN TURBULENT THERMOACOUSTIC SYSTEMS	71
5.1	Canard explosions in turbulent combustors	72
5.2	Modelling canard explosion in thermoacoustic system	78
5.2.1	Bursting behaviour due to underlying canard explosion	82
5.3	Concluding remarks	84
CHAPTER 6	TRANSITIONS IN AEROACOUSTIC SYSTEMS	87
6.1	Dynamical states associated with shifts in whistling frequency	88
6.1.1	The phenomenon of lock-in between the acoustic and hydrodynamic modes	93
6.1.2	Characterizing the dynamical states using recurrence	98
6.1.3	Investigating the synchronised dynamics of the acoustic and hydrodynamic field	103
6.2	Concluding remarks	109
CHAPTER 7	CONCLUSIONS AND FUTURE PROSPECTS	111
APPENDIX A	CANARD EXPLOSIONS AND GRADUAL TRANSITIONS	117
A.1	Hopf bifurcation: Emergence of LCO from the silent state	117
A.2	Comparison between the canard explosion and the gradual transition	118
APPENDIX B	NATURAL MODES AND TIME SERIES OF AEROACOUSTIC SYSTEMS	123
B.1	Eigenmodes of the aeroacoustic system and the mode shapes excited during whistling	123
B.2	Time series of acoustic pressure during the states of LCO and intermittency	124

APPENDIX C	RECURRENCE ANALYSIS FOR THE AEROACOUSTIC SYSTEM	127
C.1	Recurrence plots for the states of LCO and intermittency	127
C.2	Joint recurrence plots for the states of LCO and intermittency	127
APPENDIX D	SYNCHRONISATION ANALYSIS FOR THE AEROACOUSTIC SYSTEM	131
BIBLIOGRAPHY		135
CURRICULUM VITAE		151
DOCTORAL COMMITTEE		153

LIST OF TABLES

Table

Caption

Page

LIST OF FIGURES

Figure	Caption	Page
2.1	Representation of the types of bifurcation obtained by augmenting the driving term η of Eq. (2.9) with the higher order nonlinear terms. (a) Supercritical Hopf bifurcation with a single stable branch of LCO. (b) Subcritical Hopf bifurcation with a single unstable LCO branch. (c) Subcritical Hopf bifurcation to a stable LCO branch. (d) Secondary bifurcation depicting a supercritical followed by a sudden discontinuous secondary transition to a large amplitude stable LCO. Open circles represent the unstable solutions, and the solid circles represent the stable solutions. This figure is replicated with approval from Ananthkrishnan <i>et al.</i> (1998)	26
2.2	Representation of the patterns from the recurrence matrix for the states of (a) chaos, (b) intermittency and (c) LCO. This figure is reproduced with permission from Nair <i>et al.</i> (2014), <i>J. Fluid Mech.</i> 756, 470–487 (2014), published by Cambridge University Press.	38
2.3	Representation of the variation of the probability of recurrence $P(\tau)$ as a function of time lag τ . $P(\tau)$ variations for two different signals, represented as black and blue curves are overlapped to identify the type of synchronisation at different time intervals for the states of intermittency. (b) During an aperiodic epoch, there is no overlap in the variations of $P(\tau)$ for the blue and black signals, implying there is no relationship between the two signals. However, during the (c) periodic epoch, there is an overlap between the curves of $P(\tau)$, implying a phase synchronisation between the two signals. This figure is reproduced with permission from Godavarthi <i>et al.</i> (2020), <i>Chaos</i> 30, 033121 (2014), published by AIP Publishing.	42
3.1	Schematic of (a) a backward facing step combustor which can be operated in two different configurations based on the flame holding mechanisms. (b) The swirler and (c) the bluff body are used as two different flame holders for the backward facing step combustor. The design of this combustor was adapted from Komarek and Polifke (2010)	47
3.2	Schematic of (a) the annular combustor comprising sixteen burners. At the exit of each burner, (b) a swirler is used as a flame holder.	49
3.3	Schematic of the aeroacoustic system, which has a confined flow through the double orifices.	51
3.4	The representation of the acoustic pressure oscillations under no-flow conditions, both before and after the abrupt shutdown of the loudspeaker. We extract the envelope of the decaying pressure oscillations and fit an exponential curve, represented in the form of $p' = m \exp^{-\alpha t}$. Here, α represents the decay rate corresponding to the decaying portion of the acoustic signal immediately after turning off the loudspeaker	53

4.1	<p>Characteristics of secondary bifurcation in the annular combustor. (a) The variation of p'_{rms} as a function of the control parameter ϕ. Panels (b-e) shows the time series, the PDF $\mathcal{P}(p')$ and the amplitude spectrum $\hat{p}(f)$ of pressure fluctuations p' observed during the states of (b) combustion noise, (c) intermittency, (d) low amplitude limit cycle oscillations and (e) large amplitude limit cycle oscillations, as indicated in panel (a). Note the increase in the abscissa limits for the time series and distribution in panels (b) to (e).</p>	58
4.2	<p>The variation of p'_{rms} as a function of ϕ during secondary bifurcation in (a) the swirl-stabilized backward facing step combustor and (b) the bluff-body stabilized backward facing step combustor with preheated air.</p>	59
4.3	<p>Bifurcation characteristics of the stochastic thermoacoustic system. Variation in the amplitude of fluctuations for (a) subcritical and (b) supercritical bifurcation followed by a secondary bifurcation to a large amplitude limit cycle. The bifurcation diagram for the deterministic system ($\Gamma = 0$, cf. Eq. 4.3) is indicated by the black line. The difference in the abscissa in (a) and (b) indicates the significant difference between the amplitude of limit cycles due to subcritical and secondary bifurcation. The solid lines correspond to the stable solution, while the broken lines indicate an unstable solution. The contour shows the variation in probability density function $\mathcal{P}(A)$ with parameter μ_0, estimated according to Eq. ((4.11)). The noise intensity is fixed at $\Gamma = 10^{6.5}$. The other model parameters are: (a) $\mu_2 = -10$, $\mu_4 = 3$, $\mu_6 = 0$; and (b) $\mu_2 = 7$, $\mu_4 = -0.6$, $\mu_6 = 0.01$. Labels μ_H, μ_F, and μ_S indicate the parameter value μ_0 at which Hopf, fold, and secondary bifurcations occur.</p>	60
4.4	<p>Simulated time series of $\eta(t)$, probability density function $\mathcal{P}(\eta)$ and the spectrum $\hat{\eta}(f)$ from the stochastic model during the state of (a) combustion noise ($\mu_0 = -20$), (b) intermittency ($\mu_0 = -5$), (c) low-amplitude thermoacoustic instability ($\mu_0 = 5$) and (d) high-amplitude thermoacoustic instability ($\mu_0 = 20$). The simulation parameters are: $\mu_6 = 0.01$, $\mu_4 = -0.6$, $\mu_2 = 7$ and $\Gamma = 10^{6.5}$.</p>	63
4.5	<p>Effect of stochastic fluctuations on the properties of secondary bifurcation for (a) $\Gamma = 10^{6.5}$ and (b) $\Gamma = 10^{7.5}$. The contours show the variation in the distribution $\mathcal{P}(A)$ as a function of μ_0. Panels (c) and (d) depict the potential functions $V(A)$ (top panel) and distribution $\mathcal{P}(A)$ (bottom panel). The bold line indicates the potential V. The contributions of individual terms of Eq. (4.6) are also indicated. $V(A)$ and $\mathcal{P}(A)$ are shown at $\mu_0 = -5$, 4 and 12, marked by the dotted lines in panels (a) and (b). Other simulation parameters are the same as that in Fig. 4.3(b).</p>	66
4.6	<p>Illustration of hysteresis observed during the secondary bifurcation. Plot shows the variation of the potential function $V(A)$ when the value of the parameter is decreased from $\mu_0 = 15$ to $\mu_0 = -3$.</p>	67

5.1	Representation of a sudden transition to high amplitude periodic oscillations via canard explosion in the bluff body stabilized dump combustor. (a, b & c) The bifurcation diagrams for the variation of the rms value of the acoustic pressure fluctuations (p'_{rms}) as a function of the equivalence ratio ϕ . (d-i) The corresponding time series of the acoustic pressure signal during canard explosion. (a) Sudden transition from a low amplitude (d) ($p'_{\text{rms}} = 420$ Pa) to very high amplitude (e) ($p'_{\text{rms}} = 3525$ Pa) acoustic pressure fluctuations as ϕ is varied. When ϕ is varied in finer steps between these apparently abrupt transition points, we observe a (b) continuous transition (f-i) to high amplitude fluctuations via (g) bursting dynamics. (c) The transition retraces the forward path when ϕ is varied in the reverse direction, implying the absence of the hysteresis. Thus, a transition with a rapid increase in the magnitude of acoustic pressure fluctuations is observed within a very narrow range of the control parameter.	73
5.2	Representation of the sudden transition via canard explosion in a swirl stabilized dump combustor. (a) The forward and reverse path of the transition via the canard explosion. The equivalence ratio (ϕ) in the forward path is varied from 0.783 to 0.532. It is noticed that the transition occurs via the state of large amplitude bursting (a1-a3)	74
5.3	Representation of the sudden transition via canard explosion in an annular combustor. (a) The forward and reverse path of the transition via the canard explosion. The equivalence ratio (ϕ) in the forward path is varied from 1.4 to 0.9. We notice that the transition occurs via the state of large amplitude bursting (b1-b3)	75
5.4	(a) Representation of the variation of the exhaust gas temperature (T') along with the acoustic pressure fluctuations (p') for a swirl stabilized dump combustor, measured during the state of bursting via canard explosions ($\phi = 0.657$). (b-c) The amplitude spectrum of the envelope of acoustic pressure fluctuations (\hat{p}'_{env}) and the temperature fluctuations (\hat{T}'_{env}) have the same dominant frequency at 6 Hz. (d) The variation of T' along with p' for an annular combustor, measured during the state of bursting via canard explosions ($\phi = 1$). Notice the pattern of variations in T' and the envelope of p' ; the maxima of T' is in the region of minimum p' , and the minima of T' is in the region of maximum p'	77

- 5.5 **(a-d)** Representation of the effects of ϵ on the evolution of the solutions for Eq. (5.3), which is of the form $\dot{A} = f(\mu_0, A) - f(A^3, A^5, A^7)$. The ordinate denotes the values of $f(A^3, A^5, A^7)$ (thick orange curve), and the abscissa represents the values of A . The contributions from A^3 , A^5 , and A^7 are presented in the coloured thin solid curves. The dashed blue lines represent the control parameter curve $f(\mu_0, A)$ for $\mu_0 = 0$ and 1. Geometrically, the solutions are the points of intersections of $f(A^3, A^5, A^7)$ and $f(\mu_0, A)$. **(e)** Bifurcation diagram to represent the effect of ϵ on the continuous bifurcation curve obtained by fixing $\mu_2 = 6.7$, $\mu_4 = -0.5$, and $\mu_6 = 0.01$. The variation of μ_0 is shown on the abscissa and the solutions of Eq. (5.3) are shown on the ordinate. In the bifurcation diagram, thick lines are for stable solutions and the broken line is for unstable solutions. Notice that as ϵ is decreased from 1 to 0.001, the range of parameters to reach the high amplitude oscillations after the bifurcation decreases to a very narrow span. 79
- 5.6 Representation of the canard explosion by numerically integrating Eq. (5.2). The curves represent the variation of η_{rms} as a function of μ_o . When the control parameter μ_o is varied in steps of 1, we notice an abrupt jump in **(a)** the bifurcation diagram. The abrupt nature of the transition is due to a lack of resolution in the variation of the control parameter. The abrupt jump is also evident from the amplitude of the time series **(a1)** before and **(a2)** after the transition. However, when we vary the control parameter in finer steps, we have **(b)** stable dynamics at each of these finer steps. Thus, the model captures a rapid continuous transition **(b1-b3)**, where the amplitude rises significantly with a negligible change in μ_0 81
- 5.7 Representation of the time series for bursting behaviour at the bifurcation regime of the canard explosion, obtained by numerical integration of Eq. (5.4). **(a)** Time series analogous to the bursting behaviour of a bluff body stabilized dump combustor. **(b)** Time series analogous to the bursting behaviour of a swirl stabilized dump combustor. **(c)** Time series analogous to the bursting behaviour of an annular combustor. We notice large amplitude bursts at the bifurcation regime due to the underlying canard explosion 84

6.1	(a) rms of the acoustic pressure oscillations p'_{rms} (Pa) as a function of Re . The corresponding average flow velocity \bar{u} (m/s) of the airflow across the orifice is marked on the top abscissa. (b) The dominant whistling frequency of p' as Re is varied. The regions corresponding to the particular dominant frequency of p' signal are categorized as R1, R2, R3, R4, and R5. The shifts in dominant frequency are observed as Re is varied. (c) The time series corresponding to the transition via the state of intermittency during the shift in whistling frequency from 461 to 411 Hz; (ci) LCO, (cii) intermittency, and (ciii) LCO. (d) Time series of LCOs corresponding to the abrupt transition from one LCO to another (transition from point iv to v, marked in p'_{rms} variation) with a slight shift in dominant frequency. (e-h) Waterfall diagram of the amplitude spectrum for a particular range of Re during the shift in dominant frequency from regions R1-2, R2-3, R3-4, and R4-5.	91
6.2	Representation of the state of bursting, having sudden shifts between high and low-amplitude LCOs during the frequency shift. (a) Variation of p'_{rms} with Re . (b) The times series of p' corresponds to the state of abrupt switching between the high and low-amplitude LCOs. (c) The zoomed-in view of the high-amplitude LCO and its corresponding amplitude spectrum. (d) The zoomed-in view of the low-amplitude LCO and its corresponding amplitude spectrum.	92
6.3	Representation of the state of aperiodicity when there is no lock-in between the acoustic and hydrodynamic modes. (a) Variation of p'_{rms} for the range of Re varying from 13,000 to 20,000 and the corresponding (b) waterfall plot to show the variation of the amplitude spectrum with Re . The mint blue coloured patches represent ($Re = 14,700-15,500$ and $18,200-18,600$) the states of intermittency. The pastel red patch denotes ($Re = 15,500$ to $18,200$) the aperiodic state, where the amplitude spectrum is a broad band in nature. A large shift in frequency from 540 Hz to 920 Hz is observed for a transition via the state of aperiodicity. The time series for the states of (c) intermittency, (d) aperiodicity, (e) intermittency, and (f) LCO.	94
6.4	Representation of the variation of DET_j and p'_{rms} as a function Re (a) for the range of Re varying from 4,000 to 13,000 where the states of intermittency and abrupt transition is observed; (b) The corresponding variation in the dominant frequency. The variation of DET_j and p'_{rms} with Re (c) for the range of Re varying from 14,000 to 21,200 where we observe the states of aperiodicity, and (d) the corresponding variation in the dominant frequency. We observe a decrease in the values of DET_j during the frequency shifts for the state of intermittency and the state of aperiodicity (in the brown background). A very negligible change in DET_j is observed during the abrupt transition between the LCOs at $Re \approx 13,000$	95

- 6.5 The plots for p' fluctuations and the corresponding recurrence matrix obtained during (a,b) the state of intermittency ($Re \approx 5, 100$), (c,d) the state of abrupt switching between the limit cycle oscillations ($Re \approx 12,000$) and (e,f) the state of aperiodic oscillations ($Re \approx 16, 800$). The recurrence plots are plotted based on choosing a fixed value for the threshold $\epsilon = \lambda/5$, where λ is the maximum diameter of the reconstructed attractor in the phase space. The recurrence plot for the state of intermittency (b) has black patches, which correspond to the low amplitude aperiodic oscillations relative to λ . The recurrence plot for the abrupt switching between the LCOs (d) has the variation in the spacing between the diagonal lines (zoomed-in view, d), indicating the temporal switching of frequencies corresponding to LCOs. The presence of short, broken diagonal lines in the recurrence plots for aperiodicity (e) indicates the deterministic behaviour of the aperiodic oscillations. 99
- 6.6 Representation of the variation of the recurrence quantification measure RR during the transitions corresponding to the shifts in whistling frequency via the state of intermittency (peach-coloured box), via an abrupt switching from one LCO to another LCO (green box), and via the state of aperiodicity (light blue box). (a-e)i The variation of p'_{rms} is shown in the first column ($Re \approx 4,600-5,500, 7,000-8,000, 7,800-8,600, 11,500-12,500$ and $14,000$ to $19,800$). (a-e)ii The corresponding variation in the dominant frequency f is shown in the second column. The shaded region represents the absence of dominant frequency (eii). The variation in the RQA measure (a-e)iii recurrence rate RR is shown in the third column. The RQA measure is computed for an embedding dimension of 7 and the optimal τ of 0.7 ms. At each control parameter, the signal of length 1,00,000 points is parted into sections of 5,000 points, and the mean values of RQA are plotted. The error bar represents the standard deviation. We observe a rise and dip in the value of the RQA measure RR for the transitions via the states of intermittency and aperiodicity. 102

- 6.7 The representation of the JRP for (a) the state of intermittency at $Re \approx 5, 100$, (c) the state of LCO at $Re \approx 12, 000$ and (e) the state of aperiodicity $Re \approx 16, 800$. The corresponding signal of p' superimposed on u' oscillations during the (b) state of intermittency, (d) LCO and (f) aperiodicity are shown in the right subfigures. The presence of black dots in the joint recurrence plots represents the simultaneous recurrence of u' and p' . Diagonal lines are observed for the simultaneous recurrence of periodic u' and p' ; discontinuous diagonal lines are observed for the weakly coupled phase synchronised periodic limit cycle oscillations. During the periodic epochs of the state of intermittency as well, we observe discontinuous diagonals in the JRP. The density of the black dots is minimum during the desynchronous state of aperiodicity and the desynchronous epoch of the intermittency as a result of the very low simultaneous recurrence of u' and p' . A fixed RR of 0.1 is chosen to compute the recurrence matrix of the individual subsystems. 104
- 6.8 Representation of the variation of the RQA measures for JRP during the shifts in whistling frequency via the state of intermittency (peach-coloured box), through abrupt switching between the LCOs (green box) and through the state of aperiodicity (light blue box). (a-e)i The variation of p'_{rms} is shown in the first column for the ranges of $Re \approx 4,600-5,500, 7,000-8,000, 7,800-8,600, 11,500-12,500, \text{ and } 14,000-19,800$, respectively. (a-e)ii The corresponding variation in the dominant frequency f_{dom} is shown in the second column. The shaded region represents the absence of dominant frequency (eii). The variation in the RQA measures (a-e)iii determinism DET_J and (a-e)iv recurrence rate RR_J for JRP are shown in the third and fourth columns correspondingly. The RQA measure is calculated from the JRM. The JRM is computed as the dot product of the two recurrence matrices obtained with an embedding dimension of 7, an optimal τ of 0.7 ms and a fixed RR of 0.1. At each Re , the signal of 1,00,000 points is parted into sections of 5,000 points, and the mean values of RQA measures are plotted. The error bar represents the standard deviation. A dip in the variation of RQA measure signifies a decrease in synchronisation strength during the shift in whistling frequency. 107
- 6.9 Characterization of the type of synchronisation observed during the states of LCO, aperiodicity and the states of intermittency using the RPs where we observe the variation of $P(\tau)$ with the time lag τ . The plots of $P(\tau)$ for u' and p' show (a) the state of phase synchronisation between u' and p' during the state of LCO, (b) the state of desynchronisation between u' and p' during the state of aperiodicity. (c) The state of phase synchronisation during the periodic epochs of the intermittency, and (d) the state of desynchronisation during the aperiodic regime of the intermittency. The corresponding normalized signals of u' and p' are shown in the bottom row of each subfigure. 108

- A.1 Representation of the states of stable operation, intermittency, large amplitude bursting and limit cycle oscillations for the transition corresponding to canard explosion in a bluff body stabilized dump combustor. **(a)** Bifurcation diagram for the variation of p'_{rms} as a function of the equivalence ratio (ϕ). **(b)** Time series and phase space trajectory of low amplitude chaos during the stable operation. **(c)** Representation of the time series corresponding to the state of intermittency. **(d)** Time series corresponding to the state of bursting. We have also shown a zoomed-in region of the time series and phase space trajectories of certain epochs. Here, we present the epochs corresponding to high amplitude limit cycles (LCO, $p' \approx 3000Pa$), low amplitude LCO ($p' \approx 500 Pa$) and low amplitude chaos $p' \approx 200$. The observation implies that a low-amplitude LCO is born out of low-amplitude chaos, and the transition is continuous but rapid in nature. The existence of all the ranges of the amplitude of LCOs, including low amplitude chaos, is possibly due to the fluctuation of the system parameter across the steep rise of the canard explosion. **(e)** Time series corresponding to the state of LCO and the phase space trajectory. 120
- A.2 **(a)** Representation of a sudden transition to high amplitude periodic oscillations via canard explosion in a bluff body stabilized dump combustor. We present the bifurcation diagram for the variation of the rms value of the acoustic pressure fluctuations (p'_{rms}) as a function of the equivalence ratio ϕ . The airflow rate, which governs the control parameter, varies in steps of 5 SLPM during the canard explosion regime. **(b)** The corresponding results of canard explosions obtained from the model. **(c)** Representation of the gradual bifurcation obtained in the bluff body stabilized combustor by modifying the fuel flow rate (46 SLPM) and the distance of the bluff body from the dump plane (30 mm). **(d)** The corresponding results of gradual bifurcation obtained from the model. We notice that for a canard explosion, the amplitude rise is much steeper than the gradual transition. 121

B.1	(a) The variation of the p'_{rms} of acoustic pressure when the system is excited using a loudspeaker from 50 Hz to 1000 Hz. We observe a large peak at 536 Hz. (b) Acoustic mode shapes were obtained by locating the microphones along the duct length during the experiments. Mode shapes were obtained for the Re of 4500, 6700, 7600, 10900, and 11900. The ordinate represents the maximum amplitude of the signal from the amplitude spectrum (represented as the black dots), and the abscissa represents the position of the microphones along the length of the duct. The red curve in the plots indicates the theoretical mode shape for an open-open boundary condition of the duct, obtained using the equation $\hat{p}(x) \approx p_{max} \sin(kx) $. Where k is the wave number, and x is the distance from the duct inlet face. The expression for k is given as $k = n\pi/L$, where n is the mode number and L is the length of the duct. The frequencies corresponding to these mode shapes range from 400 to 535 Hz. We observe that these mode shapes correspond to the second mode of the duct having an open-open boundary condition.	125
B.2	Acoustic pressure fluctuations during (a) the state of intermittency at $Re \approx 7500$, (b) the state of LCO at $Re \approx 8100$, and (c) the state of intermittency at $Re \approx 8400$. According to the bifurcation diagram of figure 6.1 in the main text, the states of intermittency are found at the minima of p'_{rms} curve during the frequency shift. The maxima of p'_{rms} corresponds to the state of LCO.	126
C.1	Recurrence plots for the dynamical states observed with variation in Re . (a) LCO at $Re \approx 4800$. (b) LCO at $Re \approx 7300$. (c) Intermittency at $Re \approx 7500$. (d) LCO at $Re \approx 8100$. (e) Intermittency at $Re \approx 8400$. (f) LCO at $Re \approx 12200$. During the states of intermittency, we observe the black patches amidst the white region of RP. In contrast, during the state of LCO, we observe equally spaced continuous diagonal lines in the RP.	128
C.2	Joint recurrence plots of the dynamical states that are observed with variation in Re . (a) LCO at $Re \approx 4800$. (b) LCO at $Re \approx 7300$. (c) Intermittency at $Re \approx 7500$. (d) LCO at $Re \approx 8100$. (e) Intermittency at $Re \approx 8400$. (f) LCO at $Re \approx 12200$. We observe diagonal lines in the JRP when there is higher synchronisation strength between the two periodic signals. We observe sparsely spaced black dots, interspersed with broken diagonal lines, in JRPs when the synchronisation strength is low during the states of intermittency.	129
D.1	The fluctuations in the signal from the microphone and hotwire measured during the experiments when the bulk flow velocity is 13.4 m/s based on the diameter of the orifice ($Re = 17800$). Here, (a) we observe that there is slight periodicity in the acoustic pressure fluctuation, which is observed (b) as a peak in the amplitude spectrum. In contrast, the spectrum of the velocity fluctuations is broad without having any sharp peaks.	132

D.2 The fluctuations in the signals from the microphone and hotwire measured during the experiments. We present the time series and their zoomed-in versions in the first column and the respective amplitude spectrum in the second column. The measurements are taken when the bulk flow velocity is 9.07 m/s based on the diameter of the orifice ($Re = 12077$). . 133

GLOSSARY

Aeroacoustic instability	Self-sustained, large amplitude oscillations of acoustic pressure and velocity due to the positive feedback between the unsteady fluctuations of the turbulent flow and the acoustic field.
Intermittency	Dynamical state consisting of epochs of periodic oscillations amidst the aperiodic fluctuations.
Limit Cycle	An isolated closed trajectory in the phase space. When the system exhibits the state of limit cycle oscillations, every other trajectory in the phase space spirals into the limit cycle either as the time approaches infinity or as the time approaches negative infinity.
Phasespace trajectory	A space whose coordinates are the state variables of the dynamical system, representing the evolution of the solutions of the system.
Subcritical Hopf bifurcation	An abrupt discontinuous transition from a stable fixed equilibrium point to a finite amplitude oscillatory state. The hysteresis phenomenon generally accompanies the bifurcation due to bistable region.
Supercritical Hopf bifurcation	A gradual transition from a stable fixed equilibrium point to an oscillatory state..
Thermoacoustic instability	Self-sustained, large amplitude oscillations of acoustic pressure and velocity arising primarily through an interaction of sound waves in a confined space with the unsteady heat release rate caused by combustion.

ABBREVIATIONS

AVM Average Mutual Information.

CN Combustion Noise.

FFT Fast Fourier Transform.

FNN False Nearest Neighbours.

GS Generalized Synchronization.

GS Liquid Petroleum Gas.

JRM Joint Recurrence Plot.

LCO Limit Cycle Oscillations.

MFC Mass Flow Controllers.

NO_x Nitrogen Oxides.

PDF Probability Density Function.

PLV Phase Locking Value.

PS Phase Synchronization.

rms Root Mean Square.

RP Recurrence Plot.

SLPM Standard Liters Per Minute.

TAI Thermoacoustic Instability.

NOTATION

\bar{u}	average velocity of the bulk flow
$\Delta\phi$	phase difference
\dot{m}_a	air flow rate
\dot{m}_f	fuel flow rate
$\dot{Q}'(t)$	temporal variation of global heat release rate fluctuations
Γ	noise intensity
γ	specific heat ratio
Λ	dynamic viscosity
λ	wavelength of acoustic mode
\mathcal{P}	probability density function
Ω	variation of the phase of the envelope A , a slow variable in comparison to the system oscillations ω
ω	frequency of the harmonic oscillator in the model
ϕ	equivalence ratio
ρ	density
τ	delay or time lag
Υ	ratio of the rate of the mass flow of the fuel and the air
ξ	white noise
A	Amplitude of the envelope of the time series, a slow variable in comparison to the system oscillations ω

DET determinism

f frequency of the oscillations, in experiments

L length of the acoustic duct

P probability of recurrence

$p', p'(t)$ acoustic pressure fluctuations

p'_{rms} root mean square value of acoustic pressure fluctuations during the state of thermoacoustic instability

R transition amplitude factor

Re Reynolds number

RR recurrence Rate

t time

$u', u'(t)$ acoustic velocity fluctuations

V potential function

CHAPTER 1

INTRODUCTION

The industrial revolution in the mid-18th century embarked on extracting heat energy by burning fuels. The heat energy so extracted was channelized through an engine to obtain mechanical work or electrical power. Engineers soon increased these engines' efficiency and power output by exploiting thermodynamic principles. The heat engines' increased efficiency and power output encouraged humankind to build rockets and gas turbine engines. These power-producing engineering systems face the problem of oscillatory instabilities damaging the crucial components of the engine and sometimes even causing the failure of the engine. These systems involve large mass flow rates of the turbulent flow in which there is an active interaction between the vorticity, dilation, entropy, and acoustic pressure fields. Therefore, these systems are also referred to as aero-thermoacoustic systems (Mawardi, 1956). Majorly these systems are studied under two categories: (1) thermoacoustic systems and (2) aeroacoustic systems. Thermoacoustic systems involve the interaction between the hydrodynamic field, unsteady heat release rate fluctuations and the acoustic field. In aeroacoustic systems, the interactions are between the hydrodynamic field and the acoustic field in the absence of the effect of heat energy. The current thesis deals with the investigation of the transition to high amplitude oscillatory instabilities in these thermoacoustic and aeroacoustic systems.

1.1 THERMOACOUSTIC SYSTEMS

The history of thermoacoustic systems dates back to 18th century when Higgins (1802) reported a sound from a tube having a hydrogen flame. Later, Leconte (1858) reported the relationship between sound and flames when he noticed that flames responded synchronously to music. Since then, the dynamics of thermoacoustics systems evolved

from being a mere academic curiosity to a significant concern with the advent of high-intensity combustion systems. Disastrous thermoacoustic oscillations were discovered in blast furnaces, boilers, and heating systems that were fired by oil, coal and gas (Putnam, 1971). The aftermath of World War II saw the power dominance race among Western powers, leading to the development of advanced combustion systems such as rockets, gas turbines and air-breathing engines. These advanced combustion systems were haunted by catastrophic thermoacoustic instability (Culick and Yang, 1995). For instance, the rocket engines of the Saturn-V in the Apollo mission faced severe combustion instability, which was then technically resolved after numerous trial and error attempts (Oefelein and Yang, 1993). The problems of thermoacoustic oscillations were also found in soviet union rockets RD-170 and RD-171 (Dranovsky, 2007). The detrimental oscillations of combustion instability were observed even in missile systems (Blomshield, 2001).

Further, in land-based power plants, gas turbines play a crucial role due to their reliability in producing uninterrupted power. However, this reliability comes at the cost of exhaust emissions, including environmental pollutants such as carbon monoxide (CO), nitrogen oxides (NO_x) and unburnt hydrocarbons (UHC) (Sawyer, 2009). Specifically, NO_x emissions sought the higher concerns due to their tendency to impact the ozone layer and cause acid rains (Koo, 2011). Thus, several studies proposed to operate the combustors at fuel-lean conditions, which reduce the NO_x emissions (Lefebvre and Ballal, 2010). However, the lean limit conditions increased the probability of combustion instability (Lieuwen and Yang, 2005).

1.1.1 Thermoacoustic instability

Thermoacoustic instability is characterized by the undesirable high amplitude acoustic pressure fluctuations and heat release rate fluctuations present in the combustion chamber. The pressure waves are amplified by the unsteady heat release rate fluctuation, which forms the acoustic source. After reflections from the wall boundaries, these pressure waves influence the heat release rate fluctuations.

A positive feedback loop is established when the heat release rate by flame is in phase with acoustic pressure fluctuations (Rayleigh, 1878). Here, energy addition and retraction by heat release fluctuations occur at the compression and rarefaction of the pressure wave, respectively. Thus, the fluctuations can exponentially grow until a nonlinearity takes over, resulting in the saturation of the acoustic pressure amplitude. The saturation in the amplitude growth occurs due to the balance between energy addition and energy losses in the combustion chamber, resulting in self-sustained oscillations (Sujith and Pawar, 2021). These large amplitude oscillations lead to loss of structural integrity through mechanical vibrations and cause the failure of thermal protection systems due to enhanced heat transfer (Lieuwen and Yang, 2005). Thermoacoustic instabilities are also a major problem in other engineering systems such as liquid rocket engines (Anderson and Yang, 2012), solid rocket motors (Summerfield *et al.*, 1992), ramjet and scramjet engines (Byrne, 1983; Ouyang *et al.*, 2016, 2017; Liou *et al.*, 1997; Davis, 1981). Despite decades of active research, the appearance of thermoacoustic instability has remained a serious problem in the design and development of modern combustors. Thus, predicting and controlling such oscillatory instabilities requires an understanding of the underlying physics of the nonlinear interactions between fluctuations in acoustic pressure and heat release rate of thermoacoustic systems.

1.1.2 Traditional approach for analysis of thermoacoustic instability

According to the classical analysis, when the combustor dynamics change from desired stable operation to undesired high amplitude pressure fluctuations, the thermoacoustic system is considered to be linearly unstable. In linear stability analysis, small perturbations are deliberately given to the system, and the evolution of these perturbations is examined to determine whether the system is linearly stable or not. If a perturbation grows exponentially, the system is linearly unstable. If all the given perturbations decay exponentially, the system is linearly stable. For a system without any energy source, the acoustic field is represented by the classical wave equation (Dowling and Williams, 1983; Hirschberg and Rienstra, 2004). The solutions to the wave equation are obtained

by representing the acoustic oscillations as harmonic waves, $p' = \text{Re}(\hat{p}e^{i\omega t})$ and $u' = \text{Re}(\hat{u}e^{i\omega t})$. Upon solving the differential equation with appropriate boundary conditions, we obtain the acoustic mode shape and the corresponding eigenfrequency.

The eigenfrequencies so obtained are complex in nature. The real part corresponds to the oscillation frequency, while the imaginary part reflects the rate at which the oscillations grow or decay. For systems without any energy sources or sinks, the imaginary part is zero. However, when a flame is present—acting as a source of acoustic energy—certain eigenfrequencies may exhibit a negative imaginary part, depending on the configuration of the system. This negative imaginary component indicates that the acoustic oscillations grow exponentially over time.

A quantitative representation of the interaction between time-varying heat release and acoustic waves is crucial in determining the oscillation frequency. One of the widely known approaches for representing this interaction is the $n - \tau$ model, proposed by Crocco and Cheng (1956). The model involves empirically obtaining a linear relationship between the acoustic field and the heat release rate fluctuations (\dot{q}') of the system. Mathematically, the relationship is expressed as $\dot{q}' = \eta u'(t - \tau)$. Here, u' represents the velocity fluctuations of the acoustic field, τ is the delay, and η is the strength of growth or decay of the oscillations (Bloxsidge *et al.*, 1988; Macquisten, 1995; Dowling, 1997). This model has been widely applied to investigate combustion instabilities in liquid propellant rocket engines (Culick, 1988).

One of the prominently established methods for studying flame dynamics is through flame transfer functions. This technique relates the flame's heat release response to acoustic perturbations at a given excitation frequency f , assuming a fixed amplitude of the input disturbance. Here, the relationship between the flame and the acoustic pressure fluctuations is obtained using a flame transfer function (FTF) at a particular forcing frequency ω . FTF measures the linear response of the heat release rate perturbations (\dot{q}')

to the external velocity perturbations (u') at different values of forcing frequency and is given as,

$$FFT(\omega) = \frac{\dot{q}'(\omega)/\bar{q}}{u'(\omega)/\bar{u}} \quad (1.1)$$

where \bar{q} and \bar{u} represent the mean of the heat release rate fluctuations and the velocity, respectively. Thus, this method can investigate the interaction between the flame and the acoustics field to a certain extent. The response of the interaction is then utilized to derive low-order models. Numerous studies have used FTF to perform linear stability analysis in theoretical models (Bloxsidge *et al.*, 1988; Fleifil *et al.*, 1996; Candel, 2002) and experimental systems ranging from laminar (Baillot *et al.*, 1992; Ducruix *et al.*, 2000) to turbulent flames (Külsheimer and Büchner, 2002).

Further, a thermoacoustic system can also be modelled as a network of interconnected acoustic elements. Each component—such as the air/fuel supply, flame, combustion chamber, and exit nozzle—is characterized by a linear relationship that links the acoustic variables. By combining the transfer functions of these individual elements, similar to that of control systems, a system of linear equations can be constructed. The eigenvalues of this system determine the stability characteristics, while the corresponding eigenfunctions define the acoustic mode shapes. Several studies have utilized this approach in studying thermoacoustic systems (Krebs *et al.*, 1999; Polifke *et al.*, 2001; Paschereit *et al.*, 2002).

1.1.3 Dynamical systems and complex systems approach

Linear stability analysis predicts the exponential growth of infinitesimally small disturbances when a system is linearly unstable. However, in real combustors, once instability sets in, the oscillation amplitude does not grow indefinitely but instead saturates into a limit cycle. While linear theories, along with studies on flame response, offer a strong basis for analyzing thermoacoustic instabilities and provide critical insights, they fall short of capturing the full scope of the dynamics. Due to the inherent nonlinearities in thermoacoustic systems, the actual behaviour can be far more complex than just growth and saturation (Dowling, 1997; Kabiraj, 2012; Balasubramanian and

Sujith, 2008a).

Hopf bifurcations and the phenomenon of triggering

A systematic way to study thermoacoustic instability is through numerical simulations or laboratory experiments that explore how changes in system parameters influence overall dynamics Kabiraj (2012). This process helps in isolating the impact of individual parameters on system stability, often resulting in stability maps, and provides insight into the behaviour of the system when it becomes unstable (Etikyala and Sujith, 2017; Singh *et al.*, 2021). This approach, formally known as bifurcation analysis (Strogatz, 2018), has been widely used in both academic settings—such as studies on electrically heated Rijke tubes (Matveev, 2003; Subramanian *et al.*, 2010; Juniper, 2011)—and industrial combustion systems (Knoop *et al.*, 1997; Lieuwen, 2002). These investigations primarily focus on how a system transitions from a stable steady state to instability, typically marked by the onset of limit cycle oscillations.

The qualitative change in the behaviour of a dynamical system is referred to as a bifurcation (Strogatz, 2018). Similarly, in combustors, a transition from a stable operating condition to an unstable operating condition is referred to as a bifurcation (Lieuwen, 2002). Limit cycle oscillations emerge due to underlying nonlinearities of thermoacoustic systems. The transition of a dynamical system from a fixed point to a limit cycle solution owing to a change in the control parameter is referred to as a Hopf bifurcation (Strogatz, 2018). If, during the transition, the amplitude of the limit cycle increases gradually, then it is referred to as a supercritical Hopf bifurcation. If, on the contrary, the transition is abrupt, it is called a subcritical Hopf bifurcation. The subcritical nature of the transition gives rise to phenomena like hysteresis and triggering, particularly within the subcritical instability regime (Matveev, 2003; Mariappan *et al.*, 2010; Juniper, 2012). These behaviours are especially undesirable in practical combustion systems due to the potential for sudden and difficult-to-control oscillations

One of the intriguing nonlinear behaviours observed in thermoacoustic systems is the phenomenon of triggering instability. This refers to the onset of instability in a system that is linearly stable but becomes unstable when subjected to finite amplitude disturbances. If one observes the subcritical bifurcation, there are three main regimes for the control parameter: region of global stability, bistable regime (fixed point and limit cycle) and the stable regime of limit cycle oscillations. The thermoacoustic system can exhibit a silent (normal operating condition) state when the control parameter is at a stable fixed point in the bistable regime. However, at the same control parameter value, any perturbations that kick the pressure amplitude of the system near the limit cycle regime cause the system to exhibit thermoacoustic instability. Such disturbances may arise, for instance, during spark plug ignition or small explosions in the combustion chamber. In such a scenario, the probability of not having thermoacoustic instability depends on the amplitude of initial disturbances falling below a certain threshold value. These initial disturbances, in general, depend on the flow conditions, distribution of the local equivalence ratio and the geometry of the combustor.

In the 1960s, a common method for evaluating the stability of the combustion system of liquid and solid propellant rocket engines involved introducing pressure pulses through controlled explosions and analyzing the response of the system. These experiments revealed that such finite-amplitude perturbations could induce instability, a behaviour that became known as pulse-triggered or triggering instability (Anderson and Yang, 1995). Several studies have included the velocity coupling with the nonlinear combustion model in order to analytically describe the triggering instability (Levine and Baum, 1983; Wicker *et al.*, 1996; Burnley and Culick, 2000).

Hysteresis is another critical nonlinear phenomenon in combustion systems, alongside triggering. It arises in systems that undergo a subcritical Hopf bifurcation, where the system's stability depends not only on the current operating conditions but also on its past states. Because of this, returning to previously stable operating parameters does

not necessarily restore stability unless the system fully exits the hysteresis zone. As subcritical bifurcations are commonly observed in thermoacoustic systems, hysteresis has been reported in multiple studies (Knoop *et al.*, 1997; Matveev, 2003; Mariappan *et al.*, 2010; Gopalakrishnan and Sujith, 2014)

More than Hopf bifurcations

The view of thermoacoustic systems, however, is more than a mere Hopf bifurcation from fixed points or limit cycles. Although more complex pressure oscillations had been observed in the context of thermoacoustic instability, these findings initially received limited attention (Jahnke and Culick, 1994; Sterling, 1993; Lei and Turan, 2010; Keanni *et al.*, 1989). However, more of these non-linear behaviours of thermoacoustic systems came to light by the work of Kabiraj *et al.* (2012*b,a*); Kabiraj and Sujith (2012); Kabiraj (2012), who employed nonlinear time series analysis to systematically investigate bifurcations in laminar thermoacoustic systems involving simple ducted flames. Their studies revealed that, beyond reaching a limit cycle, thermoacoustic systems can undergo additional bifurcations, leading to states such as quasiperiodicity, frequency locking, period- n oscillations, intermittency, and even chaos. In another study by Guan *et al.* (2020) a distinct route to chaos via intermittency in a laminar thermoacoustic setup was discovered. More recently, strange nonchaotic attractors were observed in both laminar and turbulent thermoacoustic systems Premraj *et al.* (2020); Thonti *et al.* (2024). These findings underscore that thermoacoustic systems can exhibit more complex dynamics. In the following section, we extend this discussion to complexity in turbulent reacting flow systems.

1.1.4 Dynamics of turbulent combustors

Turbulence greatly increases the complexity of thermoacoustic systems by introducing a wide spectrum of interacting scales and many degrees of freedom. Additionally, these systems are influenced by other intricate phenomena such as chemical reactions, molecular mixing, and their coupling with acoustic fields. Thus, thermoacoustic instabilities

in turbulent combustors often exhibit characteristics that go beyond the traditional interpretation based on Hopf bifurcation theory (Sujith and Unni, 2020). The state of stable combustor operation is seldom a fixed point. This state is better characterised by aperiodic fluctuations arising due to turbulence and is referred to as combustion noise (Candel *et al.*, 2009; Gotoda *et al.*, 2011). In fact, the aperiodic pressure fluctuations during combustion noise have high dimensional chaos and multifractal signatures (Nair *et al.*, 2013; Tony *et al.*, 2015; Nair and Sujith, 2014).

Nair *et al.* (2014) reported that the change of the state of a system from combustion noise to limit cycle oscillation takes place through the state of intermittency. Intermittency is an intermediate state characterised by bursts of periodic high-amplitude oscillations amidst epochs of aperiodic low-amplitude fluctuations. Thus, intermittency has the imprint of both combustion noise and TAI. Transition to TAI through intermittency has been confirmed in many studies since (Gotoda *et al.*, 2014; Huang, 2015; Kabiraj *et al.*, 2015a; Kheirkhah *et al.*, 2017). The occurrence of intermittency leads to a smooth variation of statistical measures of the system, such as the root-mean-squared (rms) or Fourier amplitude, as the state of a system changes from a state of combustion noise to TAI. Thus, we see that the transition to thermoacoustic instability occurs from a state of chaos to limit cycle oscillations via a state of intermittency. Further, several studies have attempted to model the behaviour of turbulent combustors from the state of stable operating condition (low amplitude aperiodic oscillations) to thermoacoustic instability (high amplitude limit cycle oscillations), which will be discussed in the following section.

1.1.5 Nonlinear oscillator models to describe thermoacoustic system

In modelling the transitions to thermoacoustic instability, the state of combustion noise is often assumed to be of stochastic origin (Clavin *et al.*, 1994; Burnley and Culick, 2000) in view of the difficulty in modelling pressure fluctuations that have chaotic and multifractal characteristics. Thus, modeling studies incorporate the fluctuations as additive (Burnley and Culick, 2000; Noiray and Schuermans, 2013; Clavin *et al.*, 1994; Noiray and Denisov,

2017; Bonciolini *et al.*, 2017; Gopalakrishnan *et al.*, 2016) and multiplicative noise (Kasthuri *et al.*, 2019; Clavin *et al.*, 1994; Burnley and Culick, 2000) in models of supercritical and subcritical bifurcation. These stochastic models are then analyzed by deriving the Fokker-Planck equation from which a stationary solution is obtained (Gopalakrishnan *et al.*, 2016; Bonciolini *et al.*, 2017; Noiray and Denisov, 2017). The solution of the Fokker-Planck equation yields the evolution of the probability density function (PDF) of the envelope of the amplitude of fluctuations during the transition (Noiray and Schuermans, 2013; Noiray and Denisov, 2017).

Further, some of the models have incorporated explicit slow and fast time scales in lower-order models to capture the amplitude-modulated dynamics such as mixed mode oscillations and bursting dynamics (Kasthuri *et al.*, 2019; Tandon *et al.*, 2020). Varghese *et al.* (2021) used the fractional order differential equation counterpart for the Van der Pol oscillator to model the multifractal characteristics of the acoustic pressure oscillations of the turbulent combustor. Another approach to model transitions in thermoacoustic systems is by a kicked oscillator model given by Matveev and Culick (2003). The model considers that vortices emerging from unstable shear layers are shed into the combustion chamber and ignite intensely after a certain delay. The resulting transient heat release acts as a source of acoustic energy, exciting the chamber's natural modes. These acoustic oscillations, in turn, influence the vortex-shedding process—altering both the frequency and strength of the vortices. This interaction forms a feedback loop that can destabilize the system. Later, studies have incorporated the kicked oscillator model to describe the intermittency route to thermoacoustic instability (Nair and Sujith, 2015; Seshadri *et al.*, 2016).

1.1.6 Noise-induced oscillations in thermoacoustic systems

Practical thermoacoustic systems are inherently noisy due to various internal fluctuations. These noise sources may include turbulence-induced variations in the flow field, flow separation, irregularities in the fuel-air supply, and unsteady heat release

during combustion. As a result, pressure signals in combustors always exhibit noise-driven characteristics (Kabiraj *et al.*, 2020).

In a sub-threshold regime (globally stable fixed-point regime) of the Hopf bifurcations, noise plays a major role in the practical purpose of prediction and control of thermoacoustic instability. These prediction methods are based on the concepts of stochastic resonance (SR) and coherence resonance (CR). In SR, a weak periodic input to the system is amplified due to the presence of noise, enhancing the system's ability to detect or respond to the signal (Benzi *et al.*, 1981; Douglass *et al.*, 1993). Coherence resonance (CR) is a similar phenomenon, but it occurs without any external forcing. In CR, noise enhances the system's intrinsic frequencies, resulting in intermittent and nearly periodic damped bursts (Ushakov *et al.*, 2005; Zakharova *et al.*, 2010).

In systems undergoing subcritical Hopf bifurcations, the CR resonances emerge before the onset of bistability, i.e. before the saddle-node point or before the bistable regime. In supercritical bifurcations, they appear prior to the Hopf threshold. As a result, these behaviours can serve as early warning signs for transitions into practically dangerous dynamical states. Recent studies have experimentally demonstrated coherence resonance and associated P-bifurcations in thermoacoustic systems (Kabiraj *et al.*, 2015c; Saurabh *et al.*, 2017), as well as in simplified models of such systems (Gupta *et al.*, 2017), underscoring their relevance in the predictive analysis of combustion instability. A recent study by Li *et al.* (2019) showed that as the intensity of external noise was gradually increased, the system exhibited a stochastic P-bifurcation, which is evident from the smooth transitions observed in the stationary probability density functions (PDFs). In a recent experimental study, Vishnoi *et al.* (2024b,a) investigated an electroacoustic Rijke tube simulator exhibiting a subcritical Hopf bifurcation, focusing on the influence of noise characteristics in the subthreshold regime. Their analysis examined variations in the coherence factor and Hurst exponent, revealing that the coherence factor serves as a dependable early indicator of impending instability.

However, higher noise-induced perturbations take a disadvantageous ground when they are at the bistable region, leading to the phenomenon of triggering. Waugh and Juniper (2011) examined how different types of additive noise—white, blue, and pink—can trigger thermoacoustic instability in a Rijke tube operating within the bistable regime. Their results showed that pink noise was the most effective at inducing instability. They also found that a minimum threshold amplitude of noise was necessary to trigger the transition, and this threshold varies depending on the spectral nature of the noise. The triggering phenomenon causes intermittent bursting. Unlike oscillations in CR, the bursting oscillations in triggering have high amplitude and are not damping in nature. The interval of these bursts increases as one approaches the Hopf point (Bonciolini *et al.*, 2017). This effect is seen as a gradual transition in the root mean square (rms) value of the acoustic pressure oscillations. For instance, Gopalakrishnan *et al.* (2016) showed that abrupt subcritical bifurcation in a laminar thermoacoustic system becomes continuous at high enough noise intensity.

Further, oscillatory instabilities are an emergent phenomenon in fluid flows, often accompanied by a high degree of coherence in turbulent flows. This behaviour is an indication of the characteristics of complex systems. The self-organization in turbulent flow leads to the development of an ordered acoustic field, occurring without any need for external forcing (Sujith and Unni, 2020). The approaches and techniques from complex system theory used to study thermoacoustic systems can also be utilised to investigate flow-induced oscillatory instabilities in other fluid mechanical systems. Thus, in the spirit of complex systems, we would like to explore the generic nature of the transitions in fluid flows of thermoacoustic and aeroacoustic systems.

1.2 DYNAMICS OF AEROACOUSTIC SYSTEMS

The whistling sound produced when a flow jet passes through the consecutive plates with holes is called a hole tone (Chanaud and Powell, 1965). A flow separation from the

edge or a cavity induces an unsteady flow with shear layer instabilities. The disturbances downstream of the flow propagate toward the source of the flow separation, acting as positive feedback and giving rise to self-sustained oscillations (Rockwell, 1983). These self-sustained oscillations are heard as a whistling sound. Based on the types of shear layers and impingement geometries, the tones are classified as hole tone, ringtone, edge tone, and shear tones (Rockwell and Naudascher, 1979). The first hole tone was reported by Sondhauss (1854). Since then, various experiments have been performed on the hole tone produced in the flow across consecutive orifices (Hourigan *et al.*, 1990; Huang and Weaver, 1991; Billon *et al.*, 2005; Matsuura and Nakano, 2011; Sano and Oyaizu, 2008)

The self-sustained acoustic pressure oscillations in engineering systems, having a confined flow through cavities, cause fatigue and damage the structural integrity. The whistle sound is often referred to as aeroacoustic instability. In many large solid propellant rocket motors, the segmented grains are separated by inhibitors, which remain unburnt as the propellant burns. These unburnt residual structures cause shear layers which, when impinging on a similar upcoming residual structure, give rise to self-sustained oscillations (Nomoto and Culick, 1982; Shanbhogue *et al.*, 2003). Aeroacoustic instabilities in combustion chambers were first studied by Flandro and Jacobs (1973). Past studies have shown that a significant increase in the magnitude of the acoustic wave occurs when the vortex shedding frequency is comparable with the fundamental acoustic mode of the cavities in the chamber (Flandro and Jacobs, 1973; Dunlap and Brown, 1981).

Self-sustained oscillations in a confined flow through gas pipeline systems induce cracks, thereby causing mechanical failures (Bruggeman *et al.*, 1986; Tonon *et al.*, 2011; Nakiboğlu and Hirschberg, 2012; Mohammed Al-Muslim *et al.*, 2013). Double orifices are applied to avoid cavitation and turbulence noise in the pipelines; however, they are subjected to aeroacoustic instabilities (Sano and Oyaizu, 2008). On the contrary, self-sustained oscillations are the source of pleasant music from the flue instruments such as the flute, recorder, flue organ pipe, and human whistling (Fabre *et al.*, 2012;

Howe, 1975)

Several known theories are put forth to explain the phenomenon of whistling. Rayleigh proposed the feedback mechanism for the hole tone generation (Chanaud and Powell, 1965; Rockwell and Naudascher, 1979). According to this mechanism, there are a series of subsidiary processes, such as the origination of the disturbances in the jet shear layer, transport and amplification of these disturbances leading to the formation of the vortices, pressure wave generation due to the impingement of the vortices, upstream propagation of the pressure waves that influence the disturbances through feedback. Anderson (1952) proposed that the separated shear flow at the leading edge of the orifice plate produces fluctuations in the effective orifice area due to the growth and periodic shedding of vortices. He then conjectured that these effective area fluctuations lead to pressure fluctuations, giving rise to the tonal sound.

Hourigan *et al.* (1990) experimentally and numerically investigated the generation and feedback of the sound on the vortex shedding in a flow-through two consecutive baffles in a duct. In this study, they showed that the generation of acoustic energy is dependent on the phase of the acoustic cycle corresponding to the vortex passing the baffle. They have also modelled the source of acoustic energy due to vortex street using Howe's theory of aerodynamic sound (Howe, 1975, 1980). According to Howe's theory, the acoustic power generated by a vortex as it passes through a sound field is proportional to the scalar triple product of the vorticity, the velocity of the vortex, and the acoustic particle velocity. Sano and Oyaizu (2008) experimentally investigated the generation of sound through a pipe containing two closely spaced orifices. They used hotwire anemometer to determine the convective velocities of the vortices. They showed that vortex shedding frequency is locked with the acoustic modes of the pipe but increases slightly with the bulkflow velocity.

As the Reynolds number Re , based on the bulk flow velocity, varies in a flow-through

orifice, the frequency of the self-sustained oscillations shifts (Rockwell, 1983; Huang and Weaver, 1991). The variation in Re is associated with a variation in the sound pressure level (SPL) in a particular trend. As Re increases initially, the SPL rises to reach a local maximum and then decreases to a local minimum at the time of frequency switching. An increase in Re again leads to a rise in SPL to reach another local maximum and further decrease to a local minimum for the next frequency shift (Sano and Oyaizu, 2008; Tonon *et al.*, 2011; Karthik *et al.*, 2008; Testud *et al.*, 2009). Past studies have shown that a clear whistle tone corresponding to a particular frequency is heard at the maxima of the sound pressure level.

1.2.1 Aeroacoustic systems under the purview dynamical systems theory

Recent studies have performed time series analysis with the perspective of dynamical systems theory to investigate the dynamics of aeroacoustic systems (Nair and Sujith, 2016; Boujo *et al.*, 2020; Pavithran *et al.*, 2020; Bourquard *et al.*, 2021). The self-sustained oscillations during the clear tone of whistling correspond to limit cycle oscillations in dynamical systems. Nair and Sujith (2016) used a model-free approach to predict the onset of aeroacoustic instability by making use of certain properties of the observed acoustic pressure signal prior to the onset of instability. In their study, unsteady pressure signals were acquired from an initially silent state to the state of aeroacoustic instability. It was shown that signals display intermittent temporal bursts before the onset of instability. Other studies have also reported the state of intermittency in turbulent flow through orifices (Pavithran *et al.*, 2020) and grazing flow (Bourquard *et al.*, 2021). Bourquard *et al.* (2021) have modelled the supercritical bifurcation observed in their system, which has turbulent grazing flow, using stochastic differential equations.

As mentioned earlier, aeroacoustic systems that have confined flow through orifices have frequency shifts. However, what is the dynamical state of the system during this frequency shift has not been addressed in past studies. Often, the statistical measure rms of the pressure signal is represented as a continuous curve in aeroacoustic systems (Stubos *et al.*,

1999; Karthik *et al.*, 2008, 2001). There are instances where the abrupt jump is observed in the rms of the pressure signal (Kriesels *et al.*, 1995; Tonon *et al.*, 2011). However, a study focusing on abrupt transitions is found to be lacking in aeroacoustic systems. In the fluid mechanical systems which are studied under the purview of dynamical systems theory, such as thermoacoustic systems with turbulent flow, abrupt transitions are observed from one LCO to another LCO via secondary bifurcations (Singh *et al.*, 2021). Is there a possibility of having such abrupt transitions from one LCO to another LCO in an aeroacoustic system that has a flow through consecutive orifices? The current study reports the observation of the state of intermittency during the frequency shift as Re increases. Upon further increase in Re , the abrupt transition from high amplitude LCO to low amplitude LCO is also observed.

Feedback from the acoustic field plays a major role in aeroacoustic instabilities. Huang and Weaver (1991) found that the shear layer instability could be driven to higher sound pressure levels or completely eliminated by an acoustic signal as feedback, depending on the phase shift given to the feedback signal. Acoustic perturbations, as feedback, influence the structure of nonlinear unsteady wake (Ffowcs and Zhao, 1989). Henceforth, it is important to consider a framework that helps in investigating the coupling behavior of the acoustic and hydrodynamics to explain the dynamics observed in aeroacoustic systems. The self-sustained oscillations emerging from the interactions between the acoustics and the hydrodynamics of the present aeroacoustic system under consideration allow us to make use of synchronisation theory.

1.3 MOTIVATIONS AND RESOLUTIONS

The nonlinear interactions between the chemically reactive flow and the acoustic field make a thermoacoustic system a complex system. Hence, it is practically easier to observe and substantiate several theoretically known complex systems phenomena using thermoacoustic systems (Kabiraj *et al.*, 2012*b*; Sujith and Unni, 2020). These phenomena

are also helpful in developing computationally efficient low-order models to tackle the problems of thermoacoustic instability. One such phenomenon is the abrupt transition via secondary bifurcation. Ananthkrishnan *et al.* (1998, 2005) hypothesized the possibility of a secondary bifurcation from an initially stable primary limit cycle to a large amplitude secondary limit cycle solution in practical systems having higher-order nonlinearities. In secondary bifurcation, as the control parameter varies, the system exhibits a primary supercritical bifurcation to low amplitude limit cycle oscillation followed by an abrupt secondary transition to high amplitude limit cycle oscillation. Interestingly, albeit dangerous in nature, secondary bifurcation was then experimentally confirmed in laminar (Mukherjee *et al.*, 2015) and, very recently, in turbulent (Roy *et al.*, 2021; Singh *et al.*, 2021; Wang *et al.*, 2021) thermoacoustic systems.

In turbulent thermoacoustic systems, the stable operating condition is characterized by chaotic oscillations (Gotoda *et al.*, 2011), and the unstable operation condition corresponds to an ordered state of periodic oscillations (Mondal *et al.*, 2017). The emergence of order via the state of intermittency is predominantly observed as a gradual change in the root mean square (rms) value, a statistical measure of acoustic pressure oscillations. Hence, in turbulent systems, the bifurcation is viewed as a gradual emergence of order from a state of chaos (Mondal *et al.*, 2017; Pavithran *et al.*, 2020). In contrast to this gradual transition via the intermittency state, there are reports of abrupt transitions—a sudden discontinuous jump in the rms of the acoustic pressure oscillations. The occurrence of both abrupt and continuous transitions in thermoacoustic systems makes apparent the significant challenge in their modelling. In addition, the observation of abrupt secondary transition (Roy *et al.*, 2021; Singh *et al.*, 2021; Wang *et al.*, 2021) in highly turbulent thermoacoustic systems is not understood clearly. Specifically, the explanation for what makes a transition continuous and another abrupt has been found lacking in the literature. In this study, we illustrate the conditions for the contrasting scenarios of gradual and abrupt transitions in turbulent combustors.

Further, abrupt transitions are also referred to as explosive transitions and are characterized by the phenomenon of hysteresis (Kumar *et al.*, 2015). The occurrence of hysteresis is due to the simultaneous presence of multiple stable regimes for a range of control parameters (Zou *et al.*, 2014). However, in practical engineering systems, there are exceptions where a genuine steep rise in the statistical measure of the oscillations is observed, but the transition is not discontinuous (Brøns and Bar-Eli, 1991). Such transitions, where a rapid rise in the magnitude of the fluctuation occurs for a minute increment in the control parameter, were primarily investigated in the Van der Pol oscillator model and are referred to as canard explosions (Krupa and Szmolyan, 2001). A canard explosion is one of the most remarkable dynamical behaviours observed in systems with distinct time scale separation. It describes a rapid transition, occurring over a very narrow parameter range, from small oscillations emerging from a Hopf bifurcation to large relaxation-type oscillations characterized by alternating slow and fast phases.

Canard explosions have been reported in many real-world systems such as chemical oscillations (Brøns and Bar-Eli, 1991), ground dynamics of an aircraft (Rankin *et al.*, 2011), neuronal activity (Moehlis, 2006), predator-prey food chains (Deng, 2004), and light emitting diodes (Marino *et al.*, 2011). The dynamics of the system during this transition become highly sensitive to variation in the control parameter. There is a significant growth in the magnitude of the oscillation for an exponentially small range of values of the control parameter at the canard explosion regime (Brøns and Bar-Eli, 1991). The phenomenon describes a rapid transition occurring over a very narrow parameter range; the small oscillations emerge from a Hopf bifurcation to large relaxation-type oscillations characterized by alternating slow and fast phases. A family of periodic orbits can be observed following a segment of the unstable inner branch of the critical manifold for a significant duration. These trajectories are known as canard orbits, giving rise to the term canard explosion (Eckhaus, 1983).

Since the transition is rapid and occurs at an infinitely small range of parameters, a

canard explosion appears abrupt if there is a lack of resolution in the variation in system parameters (Diener, 1984). A continuous transition comprising a canard explosion, albeit appears abrupt, traces the same forward and reverse path in the control parameter variation (Börger, 2017). Further, large magnitude bursts and mixed-mode oscillations are observed when the system exhibits slow-fast dynamics at the canard explosion regime (Han and Bi, 2012; Desroches *et al.*, 2013).

Here, we report the observation of canard explosions in thermo-fluid systems for the first time, to the best of our knowledge. The current thesis presents the experimental results for the rapid rise in the magnitude of the acoustic pressure oscillations within a minute range of the control parameter, a principal feature of the canard explosion. The transition is continuous in nature and exhibits no hysteresis. A bursting behaviour comprising bursts of large amplitude acoustic pressure oscillations near the canard explosion regime is also observed. Through experimentally measuring the exhaust gas temperature during the state of bursting, the current study shows that a system parameter fluctuates at a time scale slower than the system oscillations. Further, the observed transition of the canard explosion is described using a phenomenological thermoacoustic model. Using the model, we attribute the bursting behaviour during the canard explosion to a coupling between a slow oscillatory term and a system variable which drives the system towards oscillatory instability.

Further, in aeroacoustic systems, whistling corresponds to the state of limit cycle oscillations (LCO) in dynamical systems theory. An aeroacoustic system exhibits different dynamical states when the bulk flow velocity is varied as a control parameter. Understanding the dynamical states and the transitions between them, as the control parameter is varied, is crucial in designing control strategies for such aeroacoustic oscillations. Previous studies have shown that as a control parameter varies, the whistling frequency shifts in an aeroacoustic system that has a flow through orifices. We show that such a change in frequency occurs via three different scenarios— (1) a direct transition

between two LCOs as an abrupt transition, (2) via a state of intermittency, and (3) via a state of aperiodicity. In the current aeroacoustic system, the abrupt transition between the LCOs is manifested as a bursting behaviour where the amplitude of the acoustic pressure fluctuations abruptly switches between the high and low-amplitude LCOs. The current study further shows that the dynamical state and the transition between them during the frequency shift have a correlation with the magnitude of the frequency shift. Using recurrence theory we show that there is a change in the dynamical state of the system during the frequency shift. Further, we use synchronisation theory to investigate the coupled behaviour of the velocity (u') and the acoustic pressure (p') fluctuations during the different dynamical states. Our findings imply that u' and p' exhibit phase synchronisation (PS) during the state of LCO, corresponding to whistling. In contrast, u' and p' are desynchronised during the state of aperiodicity, corresponding to stable operation. Furthermore, the bursts of periodic oscillations during intermittency correspond to the phase-synchronised epochs of periodic u' and p' , and the aperiodic epochs correspond to the desynchronised aperiodic u' and p' .

1.4 OBJECTIVES OF THE WORK

The primary aim of the thesis is to investigate the transitions in turbulent thermoacoustic and aeroacoustic systems. The current thesis discovers the underlying physics-based mechanisms for the transitions observed. The specific objectives of this thesis are:

1. Perform experiments in different configurations of turbulent thermoacoustic and aeroacoustic systems to obtain sudden transitions upon control parameter variation.
2. Characterize the dynamical states and the nature of the transitions when the control parameter is varied in turbulent thermoacoustic and aeroacoustic systems.
3. Obtain a low-order thermoacoustic model to illustrate the transitions and the dynamics observed in turbulent combustors.
4. Investigate the transitions in the aeroacoustic system during shifts in whistling

frequency by performing experiments.

5. Investigate the dynamics of the aeroacoustic system under the purview of synchronisation theory.

1.5 OVERVIEW OF THE THESIS

The methods and analysis used to study the turbulent fluid mechanical systems are presented in Chapter 2. In this chapter, we present the derivation to arrive at the self-excited harmonic oscillator used to represent the dynamics and transitions in turbulent thermoacoustic systems. We then present the method of averaging to extract the dynamics of the amplitude of the envelope from the stochastic second-order differential equation. Subsequently, the theory of recurrence analysis used for nonlinear time series analysis is introduced. The coupling between the hydrodynamics and acoustic field is studied using synchronisation theory. Therefore, we give a brief introduction to synchronisation theory and the methods to investigate the synchronisation phenomenon in this chapter.

Chapter 3 provides information on the experimental setups and the experimental procedures used to study the transitions in thermoacoustic and aeroacoustic systems. We conduct experiments in three different configurations of turbulent combustors and an aeroacoustic setup.

In Chapter 4, the experimental observations of abrupt transitions via secondary bifurcations are presented. We explain the effect of stochastic fluctuations on the nature of the transition. Further, the stability of different dynamical states is visualized with the help of a potential function. We also illustrate the dynamics of hysteresis using the potential function.

In Chapter 5, we present the experimental observations for rapid continuous transitions, referred to as canard explosions. We present the modifications for a Van der Pol oscillator model to obtain significant steepening of the bifurcation regime to represent the transition

having a canard explosion. We show that the transition occurs via a phenomenon of large-amplitude bursting. Using experimental results and the model, we show that a system parameter oscillates in correlation with the envelope of the acoustic pressure fluctuations during bursting.

The experimental results for transitions in the aeroacoustic system are presented in Chapter 6. We describe the state of intermittency, LCO, and aperiodicity using recurrence theory in this chapter. We further study the coupled dynamics of the velocity and acoustic pressure fluctuations from the perspective of synchronisation theory. Finally, the conclusions of the thesis and the scope for future work are summarized in Chapter 7.

CHAPTER 2

METHODS AND ANALYSIS TO STUDY DYNAMICAL SYSTEMS

2.1 MATHEMATICAL MODEL FOR TRANSITIONS IN THERMOACOUSTIC SYSTEMS

In thermoacoustic systems, a change in the behaviour of oscillations of the system is observed from stable operating conditions to thermoacoustic instability upon variation in control parameters. The stable operating conditions consist of very low amplitude aperiodic acoustic pressure fluctuations, and the state of thermoacoustic instability (TAI) consists of limit cycle oscillations. From a broader perspective, this behaviour is analogous to a simple self excited harmonic oscillator having a net effect of nonlinear driving. Studying thermoacoustic systems in the form of self-excited harmonic oscillators offers a simplified way to analyze the stability of the dynamical states.

In this study, we are concerned with modelling the dynamics of the acoustic pressure amplitude of the combustor as a control parameter varies. The thermoacoustic system considered here is one-dimensional, where the axial modes are excited. The effects of mean flow and temperature gradient are neglected (Nicoud and Wieczorek, 2009; Balasubramanian and Sujith, 2008b). The nonlinear acoustic terms are considered insignificant as the pressure fluctuations with respect to the mean are negligible. Thus, the dynamics of the energy release in terms of heat release rate and the acoustic field fluctuations inside the combustion chamber is governed by the linearized momentum and energy conservation equations (Balasubramanian and Sujith, 2008b), which are given as,

$$\frac{1}{\bar{\rho}} \frac{\partial p'(z, t)}{\partial z} + \frac{\partial u'(z, t)}{\partial t} = 0, \quad (2.1)$$

$$\frac{\partial p'(z, t)}{\partial t} + \gamma \bar{p} \frac{\partial u'(z, t)}{\partial z} = (\gamma - 1) \dot{Q}'(z, t) \delta(z - z_f). \quad (2.2)$$

Here, t is time, z is the distance along the axial direction of the duct, and γ is the specific heat ratio. $\bar{\rho}$ and \bar{p} indicate the mean density and pressure, while p' and u' are the pressure and velocity fluctuations, respectively. We assume the chemical reaction zone, comprising heat release rate fluctuations \dot{Q}' , to be of smaller volume majorly restricted at a location z_f and is represented by a Dirac-delta (δ) function (McManus *et al.*, 1993). Equations (2.1) and (2.2) can be appropriately modified to obtain the wave equation in an inhomogeneous form as (Lieuwen, 2021):

$$\begin{aligned} c^2 \frac{\partial^2 p'(z, t)}{\partial z^2} - \frac{\partial^2 p'(z, t)}{\partial t^2} \\ = -(\gamma - 1) \frac{\partial \dot{Q}'(z, t)}{\partial t} \delta(z - z_f), \end{aligned} \quad (2.3)$$

where, $c = \sqrt{\gamma \bar{p} / \bar{\rho}}$ is the acoustic speed. An ordinary differential equation by simplifying Eq. (2.3) using a Galerkin modal expansion is obtained (Lores and Zinn, 1973). u' and p' are rewritten in terms of a set of spatial basis functions (sines and cosines). The temporal coefficients of the basis functions are η and $\dot{\eta}$, and are represented as:

$$\begin{aligned} p'(z, t) &= \bar{p} \sum_{j=1}^n \frac{\dot{\eta}_j(t)}{\omega_j} \cos(k_j z) \quad \text{and} \\ u'(z, t) &= \frac{\bar{p}}{\bar{\rho} c} \sum_{j=1}^n \eta_j(t) \sin(k_j z), \end{aligned} \quad (2.4)$$

where j represent the eigenmodes. The basis functions satisfy the acoustic boundary conditions - i.e., $u' = 0$ at the closed end and $p' = 0$ at the open end of the duct. The chosen basis functions are orthogonal in nature. These basis functions also form the eigenmodes of the self-adjoint part of the linearized equations (Balasubramanian and Sujith, 2008b). Here, for a given length of the combustor L , k_j is the wavenumber ($k_j = (2j - 1)\pi/2L$). The wavenumber is related to the natural frequency as $\omega_j = ck_j$. After substituting for Eq. (2.4), Eq. (2.3) can be written as,

$$\begin{aligned} \sum_{j=1}^n \frac{\ddot{\eta}_j(t)}{\omega_j} \cos(k_j z) + \frac{\gamma \bar{p}}{\bar{\rho} c} \sum_{j=1}^n \eta_j(t) k_j \cos(k_j z) \\ = \frac{\gamma - 1}{\bar{p}} \dot{Q}' \delta(z - z_f). \end{aligned} \quad (2.5)$$

By integrating Eq. (2.5) over the volume of the combustor, after computing the inner product along each of the basis functions, one can obtain

$$\frac{\ddot{\eta}_j(t)}{\omega_j} + ck_j\eta_j(t) = \frac{2(\gamma - 1)}{L\bar{p}} \int_0^L \dot{Q}' \delta(z - z_f) \cos(k_j z) dz. \quad (2.6)$$

Here, we choose the number of eigenmodes to be $j = 1$, which is adequate for analysing the characteristics of the transition discovered in the experiments conducted in the current study. Further, the observed dynamics in combustors is a result of the nonlinear interaction of the flame to the fluctuations in the acoustic field. Therefore, \dot{Q}' is denoted by a nonlinear function of η and $\dot{\eta}$. Thus, Eq. (2.6) simplifies to a harmonic oscillator, expressed as

$$\ddot{\eta} + \omega^2\eta = f(\eta, \dot{\eta}), \quad (2.7)$$

where, $f(\eta, \dot{\eta}) = f(\dot{Q}') - \alpha\dot{\eta}$ is the nonlinear driving function. An additional term $\alpha\dot{\eta}$ is included to account for the acoustic damping, where α is the coefficient of damping (Noiray, 2017). Thus, the source term $f(\eta, \dot{\eta})$ represents the nonlinear damping and driving behaviour of the oscillator. Further, $f(\eta, \dot{\eta})$ can be expanded with nonlinear terms such that Eq. (2.7) represents a Hopf bifurcation to thermoacoustic oscillations (Bonciolini *et al.*, 2021). The modified form of Eq. (2.7) is given as,

$$\ddot{\eta} + (\mu_2\eta^2 - \mu_0)\dot{\eta} + \omega^2\eta = 0, \quad (2.8)$$

where μ_0 is the control parameter and μ_2 is the coefficient of the second order nonlinear term. Equation (2.8) also represents the Van der Pol oscillator, which is a paradigm for systems exhibiting limit cycle oscillations (Minorsky, 1962). When μ_2 is positive, one can obtain a stable limit cycle branch denoting a supercritical Hopf bifurcation (refer to Fig. 2.1a). When μ_2 is negative, one obtains an unstable subcritical limit cycle branch (refer to Fig. 2.1b). The nonlinear coefficients associated with the driving term $\dot{\eta}$ in Eq. (2.8) can be augmented with higher order nonlinear coefficients to produce multiple limit cycle branches (Ananthkrishnan *et al.*, 1998). This augmentation helps represent the multiple high amplitude limit cycle oscillations (LCO) in thermoacoustic systems

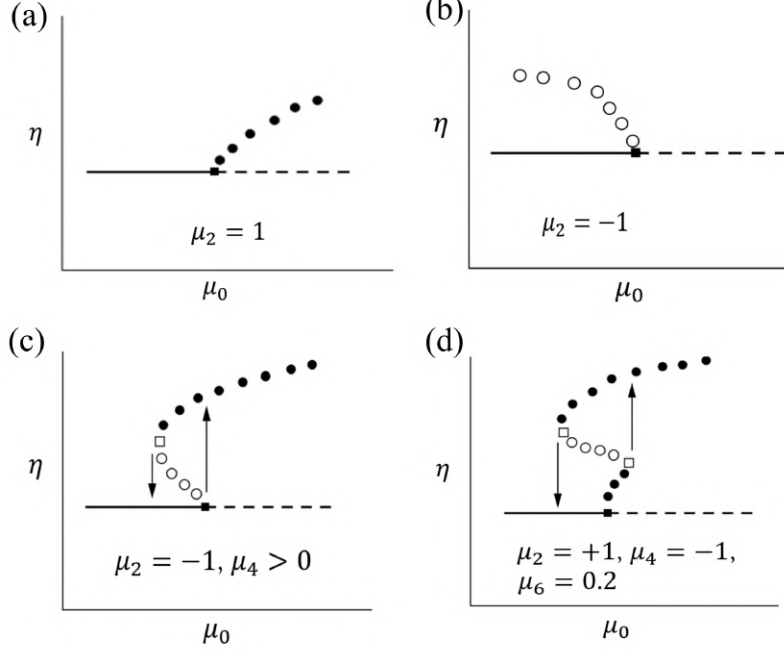


Figure 2.1: Representation of the types of bifurcation obtained by augmenting the driving term $\dot{\eta}$ of Eq. (2.9) with the higher order nonlinear terms. **(a)** Supercritical Hopf bifurcation with a single stable branch of LCO. **(b)** Subcritical Hopf bifurcation with a single unstable LCO branch. **(c)** Subcritical Hopf bifurcation to a stable LCO branch. **(d)** Secondary bifurcation depicting a supercritical followed by a sudden discontinuous secondary transition to a large amplitude stable LCO. Open circles represent the unstable solutions, and the solid circles represent the stable solutions. This figure is replicated with approval from Ananthkrishnan *et al.* (1998)

(Bhavi *et al.*, 2023). Therefore, we modify Eq. (2.8) as,

$$\ddot{\eta} + \left(\mu_6 \eta^6 + \mu_4 \eta^4 + \mu_2 \eta^2 \right) \dot{\eta} - \mu_0 \dot{\eta} + \omega^2 \eta = 0, \quad (2.9)$$

where μ_4 and μ_6 are the coefficients of the higher order nonlinear terms. The constants μ_0 , μ_2 , μ_4 , and μ_6 are model parameters where μ_o is the linear driving term (Noiray and Schuermans, 2013). However, please note that the model reproduces experimental results only in a qualitative sense. This limitation arises because the heat release rate expression employed in the model does not accurately reflect the physical conditions present in the experiments. Specifically, the model's heat release formulation does not represent the actual heat transfer dynamics from the turbulent flame of the combustors.

Additionally, the model neglects the influence of mean flow, which further contributes to quantitative discrepancies between simulation and experimental observations. As a result, the parameter values required in the model to replicate the experimental dynamics differ significantly from those used in the experiments. Despite these simplifications, the chosen expression for the nonlinear terms in Eq. (2.9) captures the essential characteristics of abrupt transitions in a thermoacoustic system. Past studies have reproduced the subcritical nature of the system in the model by introducing the third- and fifth-order nonlinear terms for heat release rate expression in place of a more generalized nonlinear function (Noiray and Schuermans, 2013; Gopalakrishnan *et al.*, 2016; Noiray, 2017). The higher-order nonlinear terms are selected to ensure the model exhibits the bistable behaviour observed in the experiments Ananthkrishnan *et al.* (1998). Notably, the form of the heat release rate used here aligns with those adopted in earlier works by Clavin *et al.* (1994); Campa and Juniper (2012).

By fixing $\mu_2 = -1$, $\mu_4 > 0$ and $\mu_6 = 0$, one can obtain an unstable LCO branch followed by a stable LCO branch representing a subcritical Hopf bifurcation (Fig. 2.1c). Similarly, by fixing $\mu_2 > 0$, $\mu_4 < 0$ and $\mu_6 > 0$, one obtains a secondary bifurcation as shown in Fig. 2.1d (Ananthkrishnan *et al.*, 1998). Thus, from Fig. 2.1, note that the coefficients μ_2 , μ_4 and μ_6 govern the stability and the amplitude of the LCO branches in the bifurcation curve. Further, in order to take the effects of turbulence into account, one can add additive Gaussian white noise, and Eq. (2.9) is modified as,

$$\ddot{\eta} + \left(\mu_6 \eta^6 + \mu_4 \eta^4 + \mu_2 \eta^2 - \mu_0 \right) \dot{\eta} + \omega^2 \eta + \xi = 0, \quad (2.10)$$

where ξ is delta correlated in time: $\langle \xi(t) \xi(t + \tau) \rangle = \Gamma \delta(\tau)$, where Γ is the noise intensity. The symbol $\langle \cdot \rangle$ represents the ensemble of realizations of the stochastic process. Thus, the overall dynamics is governed by the second-order stochastic differential equation.

2.1.1 Derivation of slow flow amplitude and phase evolution equations

The stability of the dynamical states for the stochastic differential equation (2.10) can be approximately analyzed using linear stability analysis. In linear stability analysis, the system is perturbed by infinitesimally small perturbations at a fixed point state of the system, and then the perturbations are allowed to evolve in time (Strogatz, 2018; Sujith and Pawar, 2021). If the perturbations grow, then the fixed point state is unstable. If the perturbations decay to zero, then the fixed point state is stable. Thus, linear stability analysis is a useful tool for analyzing the stability of the state of the system. However, Eq. (2.10) is a second-order differential equation which has limit cycle solutions and is a limiting condition for linear stability analysis. Therefore, we utilize the method of averaging to extract the amplitude-envelope of the oscillations of the system. We proceed with assuming the dynamics, represented by white noise, is a stationary process in our derivation. Using Krylov-Bogoliubov (KB) method of decomposition (Krylov and Bogoliubov, 2016; Balanov *et al.*, 2009), the general solution for the Eq. (2.10) is of the form

$$\eta(t) = A(t) \cos(\omega t + \Omega(t)), \quad (2.11)$$

here, $A(t)$ and $\Omega(t)$ are of slow time scale and ω is of fast time scale. The first derivative $\dot{\eta}$ for the general solution Eq. (2.11) is given as

$$\dot{\eta}(t) = \dot{A}(t) \cos [\omega t + \Omega(t)] - A(t)\omega \sin [\omega t + \Omega(t)] - A(t)\dot{\Omega}(t) \sin [\omega t + \Omega(t)], \quad (2.12)$$

By representing the general solution for $\eta(t)$ in the form of Eq. (2.11) we are considering that $A(t)$ and $\Omega(t)$ are slow variables in comparison to the fast oscillations of the system with frequency ω , i.e. $\dot{A}(t) \ll A(t)\omega$ and $\dot{\Omega}(t) \ll \omega$. Therefore, we further set an additional condition that the derivative of $\eta(t)$ in Eq. (2.12) is a simple expression of the form

$$\dot{\eta} = -A(t)\omega \sin [\omega t + \Omega(t)] \quad (2.13)$$

which would imply

$$\dot{A}(t) \cos [\omega t + \Omega(t)] - A(t) \dot{\Omega}(t) \sin [\omega t + \Omega(t)] = 0. \quad (2.14)$$

Writing the general solution in exponential form, one can get

$$\eta = A \cos (\omega t + \Omega) = A \left(\frac{e^{i(\omega t + \Omega)} + e^{-i(\omega t + \Omega)}}{2} \right) = \frac{ae^{i\omega t} + a^*e^{-i\omega t}}{2}, \quad (2.15)$$

where $a = Ae^{i\Omega}$ and $a^* = Ae^{-i\Omega}$. In a similar manner we can write Eq. (2.13), Eq. (2.14) and $\dot{\eta}$ as

$$\dot{\eta} = \frac{i\omega(ae^{i\omega t} - a^*e^{-i\omega t})}{2}, \quad (2.16)$$

$$\dot{a}e^{i\omega t} + \dot{a}^*e^{-i\omega t} = 0, \quad (2.17)$$

$$\ddot{\eta} = i\omega\dot{a}e^{i\omega t} - \frac{\omega^2}{2}(ae^{i\omega t} + a^*e^{-i\omega t}), \quad (2.18)$$

respectively, where $\dot{a} = \dot{A}e^{i\Omega} + iA\dot{\Omega}e^{i\Omega}$ and $\dot{a}^* = \dot{A}e^{-i\Omega} - iA\dot{\Omega}e^{-i\Omega}$. Substituting for η , $\dot{\eta}$ and $\ddot{\eta}$ in Eq. (2.10) and letting $ae^{i\omega t} + a^*e^{-i\omega t} = \beta$ we get

$$i\omega\dot{a}e^{i\omega t} - \frac{\omega^2}{2}\beta + \left(\frac{\mu_6}{64}\beta^6 + \frac{\mu_4}{16}\beta^4 + \frac{\mu_2}{4}\beta^2 - \mu_0 \right) \times \frac{i\omega}{2}(ae^{i\omega t} - a^*e^{-i\omega t}) + \frac{\omega^2}{2}\beta + \xi = 0, \quad (2.19)$$

where a , \dot{a} and a^* are slow functions of time as compared to $e^{(\pm n\omega t)}$, n being an integer. We further simplify Eq. (2.19) by expanding β^6 , β^4 and β^2 using binomial expansion, which is not shown here in the interest of space. In order to eliminate the terms associated with the fast time scale, we divide Eq. (2.19) with $i\omega e^{i\omega t}$ and average the whole equation over the time period, $T = 2\pi/\omega$, of fast oscillations. The terms having even integers in $e^{(\pm n\omega t)}$ will be zero after averaging. Substituting for $a = Ae^{i\Omega}$, $a^* = Ae^{-i\Omega}$ and $aa^* = |A|^2$ we get

$$\dot{A} + iA\dot{\Omega} - \frac{\mu_0}{2}A + \frac{\mu_2}{8}A^3 + \frac{\mu_4}{16}A^5 + \frac{5\mu_6}{128}A^7 - i\frac{\xi}{\omega}e^{-i(\omega t + \Omega)} = 0. \quad (2.20)$$

Separating Eq. (2.20) into real and imaginary parts, we have

$$\dot{A} - \frac{\mu_0}{2}A + \frac{\mu_2}{8}A^3 + \frac{\mu_4}{16}A^5 + \frac{5\mu_6}{128}A^7 - \frac{\xi}{\omega} \sin (\omega t + \Omega) = 0, \quad (2.21)$$

$$A\dot{\Omega} - \frac{\xi}{\omega A} \cos(\omega t + \Omega) = 0. \quad (2.22)$$

Equations (2.21) and (2.22) are the governing equations for the evolution of slowly varying amplitude and phase, respectively. The amplitude and phase equation can be explicitly written as,

$$\begin{aligned} \dot{A} &= - \left(-\frac{\mu_0}{2}A + \frac{\mu_2}{8}A^3 + \frac{\mu_4}{16}A^5 + \frac{5\mu_6}{128}A^7 \right) + \frac{\xi}{\omega} \sin(\omega t + \Omega), \\ \dot{\Omega} &= \frac{\xi}{\omega A} \cos(\omega t + \Omega) \end{aligned} \quad (2.23)$$

2.1.2 Stochastic averaging of the slow flow equations

When $\xi = 0$, Eq. (2.23) represents the deterministic evolution of the envelope-amplitude of the oscillations of the system. In order to simplify the stochastic term $\xi e^{-i\omega t}$, we make use of the procedure used by Stratonovich (1963). The method involves the use of Fokker-Planck (FP) equation that describes the time evolution of the joint PDF of amplitude $\mathcal{P}(A)$ and $\mathcal{P}(\Omega)$, simplification of the FP equation and reconstructing the stochastic differential equations that correspond to the simplified FP equation. For simplicity, if we consider a generic form representing the evolution of the amplitude and phase as,

$$\begin{aligned} \dot{A} &= G_A(A, \Omega) + H_A(A, \Omega, \xi) = F_A, \\ \dot{\Omega} &= G_\Omega(A, \Omega) + H_\Omega(A, \Omega, \xi) = F_\Omega, \end{aligned} \quad (2.24)$$

here from Eq. (2.23) we have,

$$\begin{aligned} G_A &= - \left(-\frac{\mu_0}{2}A + \frac{\mu_2}{8}A^3 + \frac{\mu_4}{16}A^5 + \frac{5\mu_6}{128}A^7 \right), \\ H_A &= \frac{\xi}{\omega} \sin(\omega t + \Omega), \\ G_\Omega &= 0, \\ H_\Omega &= \frac{\xi}{\omega A} \cos(\omega t + \Omega). \end{aligned} \quad (2.25)$$

F_A and F_Ω are the stochastic functions of amplitude and phase. Following Stratonovich (1963) and Balanov *et al.* (2009), we write the FP equation describing the joint probability

density function $\mathcal{P}(A, \Omega, t)$ as,

$$\begin{aligned}
\frac{\partial \mathcal{P}}{\partial t} = & -\frac{\partial}{\partial A} \left\{ \left(\langle F_A \rangle + \int_{t_0-t}^0 \psi \left[\frac{\partial F_A}{\partial A}, F_{A\tau} \right] d\tau + \int_{t_0-t}^0 \psi \left[\frac{\partial F_A}{\partial \Omega}, F_{\Omega\tau} \right] d\tau \right) \mathcal{P} \right\} \\
& -\frac{\partial}{\partial \Omega} \left\{ \left(\langle F_\Omega \rangle + \int_{t_0-t}^0 \psi \left[\frac{\partial F_\Omega}{\partial A}, F_{A\tau} \right] d\tau + \int_{t_0-t}^0 \psi \left[\frac{\partial F_\Omega}{\partial \Omega}, F_{\Omega\tau} \right] d\tau \right) \mathcal{P} \right\} \\
& +\frac{\partial^2}{\partial A^2} \left\{ \left(\int_{t_0-t}^0 \psi [F_A, F_{A\tau}] d\tau \right) \mathcal{P} \right\} +\frac{\partial^2}{\partial A \partial \Omega} \left\{ \left(\int_{t_0-t}^0 \psi [F_A, F_{\Omega\tau}] d\tau \right) \mathcal{P} \right\} \\
& +\frac{\partial^2}{\partial \Omega \partial A} \left\{ \left(\int_{t_0-t}^0 \psi [F_\Omega, F_{A\tau}] d\tau \right) \mathcal{P} \right\} +\frac{\partial^2}{\partial \Omega^2} \left\{ \left(\int_{t_0-t}^0 \psi [F_\Omega, F_{\Omega\tau}] d\tau \right) \mathcal{P} \right\}.
\end{aligned} \tag{2.26}$$

Here, $\psi [X, Y_\tau]$ is the cross-covariance of the two stochastic process X and Y_t at time instants t and $t + \tau$, respectively. The symbol $\langle \cdot \rangle$ represents the ensemble of realizations of the stochastic process. The covariance terms that appear in Eq. (2.26) can be simplified as follows. To begin with, we consider the first covariance term

$$\begin{aligned}
\psi \left[\frac{\partial F_A}{\partial A}, F_{A\tau} \right] &= \left\langle \frac{\partial F_A}{\partial A} \times F_{A\tau} \right\rangle - \left\langle \frac{\partial F_A}{\partial A} \right\rangle \langle F_{A\tau} \rangle \\
&= \left\langle \frac{\partial (G_A + H_A)}{\partial A} \times (G_{A\tau} + H_{A\tau}) \right\rangle \\
&\quad - \left\langle \frac{\partial (G_A + H_A)}{\partial A} \right\rangle \langle G_{A\tau} + H_{A\tau} \rangle.
\end{aligned} \tag{2.27}$$

We note that G_A and $\partial G_A / \partial A$ are deterministic functions of time, and they remain the same for any realization of a stochastic process ξ . Hence, their ensemble averages are given by

$$\langle G_A \rangle = G_A, \quad \left\langle \frac{\partial G_A}{\partial A} \right\rangle = \frac{\partial G_A}{\partial A}. \tag{2.28}$$

Considering Eq. (2.28) and the fact that the ensemble average of a product of a deterministic and a stochastic functions can be written as the product of the deterministic function and the average of the stochastic function. Eq. (2.27) can be written as

$$\psi \left[\frac{\partial F_A}{\partial A}, F_{A\tau} \right] = \left\langle \frac{\partial H_A}{\partial A} \times H_{A\tau} \right\rangle = \langle 0 \times H_{A\tau} \rangle = 0. \tag{2.29}$$

We can also calculate the averages and covariances of other terms in Eq. (2.26) as

$$\begin{aligned}
\psi \left[\frac{\partial F_A}{\partial \Omega}, F_{\Omega\tau} \right] &= \left\langle \frac{\partial H_A}{\partial \Omega} \times H_{\Omega\tau} \right\rangle \\
&= \left\langle \frac{\xi}{\omega} \cos(\omega t + \Omega) \times \left(\frac{\xi_\tau}{\omega A_\tau} \cos(\omega t + \omega\tau + \Omega_\tau) \right) \right\rangle \quad (2.30) \\
&= \langle \xi \xi_\tau \rangle \frac{1}{A_\tau \omega^2} \cos(\omega t + \Omega) \cos(\omega t + \omega\tau + \Omega_\tau).
\end{aligned}$$

Now, we evaluate an integral of $\psi[\partial F_A/\partial \Omega, F_{\Omega\tau}]$ over τ from $(t_0 - t)$ to 0 where t_0 is some initial time moment from which we start to consider the process. We set t_0 to minus infinity so as to consider an established process. Since we have already considered the noise ξ to be delta-correlated, the slow variables can be treated as constant in the time interval, implying $A_\tau = A$ and $\Omega_\tau = \Omega$. After simplifying the trigonometric terms in Eq. (2.30) we can write the integral as

$$\begin{aligned}
\int_{-\infty}^0 \psi \left[\frac{\partial F_A}{\partial \Omega}, F_{\Omega\tau} \right] d\tau &= \frac{1 + \cos(2\omega t + 2\Omega)}{2A\omega^2} \int_{-\infty}^0 \langle \xi \xi_\tau \rangle \cos(\omega\tau) d\tau \\
&\quad - \frac{\sin(2\omega t + 2\Omega)}{2A\omega^2} \int_{-\infty}^0 \langle \xi \xi_\tau \rangle \sin(\omega\tau) d\tau. \quad (2.31)
\end{aligned}$$

We have initially assumed that the noise we are considering is a stationary process, then its correlation function $\langle \xi \xi_\tau \rangle$ depends only on τ . According to Wiener-Khintchine theorem (Coffey and Kalmykov, 2012), the autocorrelation of the stationary process is the Fourier transform of the power spectral density Γ . The first integral on the right hand side of the Eq. (2.31) is half of the Fourier transform (FT) of the correlation function $\langle \xi \xi_\tau \rangle$ which is equal to $\Gamma/2$. The second integral is the imaginary part of the FT and is equal to zero. Hence, Eq. (2.31) simplifies to

$$\int_{-\infty}^0 \psi \left[\frac{\partial F_A}{\partial \Omega}, F_{\Omega\tau} \right] d\tau = \frac{\Gamma}{4A\omega^2} (1 + \cos(2\omega t + 2\Omega)). \quad (2.32)$$

We can again apply the Krylov-Bogoliubov method of averaging to Eq. (2.32) by taking A and Ω as slowly varying functions of time to obtain

$$\int_{-\infty}^0 \psi \left[\frac{\partial F_A}{\partial \Omega}, F_{\Omega\tau} \right] d\tau = \frac{\Gamma}{4A\omega^2}. \quad (2.33)$$

In a similar manner, we can simplify the other terms of the Eq. (2.26) as

$$\psi \left[\frac{\partial F_\Omega}{\partial A}, F_{A\tau} \right] = \left\langle \frac{\partial H_\Omega}{\partial A} \times H_{A\tau} \right\rangle = 0, \quad (2.34)$$

$$\psi \left[\frac{\partial F_\Omega}{\partial \Omega}, F_{\Omega\tau} \right] = \left\langle \frac{\partial H_\Omega}{\partial \Omega} \times H_{\Omega\tau} \right\rangle = 0, \quad (2.35)$$

$$\psi [F_A, F_{A\tau}] = \langle H_A H_{A\tau} \rangle = \frac{\Gamma}{4\omega^2}, \quad (2.36)$$

$$\psi [F_A, F_{\Omega\tau}] = \langle H_A H_{\Omega\tau} \rangle = 0, \quad (2.37)$$

$$\psi [F_\Omega, F_{A\tau}] = \langle H_\Omega H_{A\tau} \rangle = 0, \quad (2.38)$$

$$\psi [F_\Omega, F_{\Omega\tau}] = \langle H_\Omega H_{\Omega\tau} \rangle = \frac{\Gamma}{4\omega^2 A^2} \quad (2.39)$$

In view of the above, Eq. (2.26) can be rewritten as

$$\begin{aligned} \frac{\partial \mathcal{P}}{\partial t} = & \frac{\partial}{\partial A} \left\{ \left(G_A + \int_{-\infty}^0 \psi \left\langle \frac{\partial H_A}{\partial A}, H_{A\tau} \right\rangle d\tau + \int_{-\infty}^0 \psi \left\langle \frac{\partial H_A}{\partial \Omega}, H_{\Omega\tau} \right\rangle d\tau \right) \mathcal{P} \right\} \\ & - \frac{\partial}{\partial \Omega} \left\{ \left(G_\Omega + \int_{-\infty}^0 \psi \left\langle \frac{\partial H_\Omega}{\partial A}, H_{A\tau} \right\rangle d\tau + \int_{-\infty}^0 \psi \left\langle \frac{\partial H_\Omega}{\partial \Omega}, H_{\Omega\tau} \right\rangle d\tau \right) \mathcal{P} \right\} \\ & + \frac{\partial^2}{\partial A^2} \left\{ \left(\int_{-\infty}^0 \psi \langle H_A, H_{A\tau} \rangle d\tau \right) \mathcal{P} \right\} + \frac{\partial^2}{\partial A \partial \Omega} \left\{ \left(\int_{-\infty}^0 \psi \langle H_A, H_{\Omega\tau} \rangle d\tau \right) \mathcal{P} \right\} \\ & + \frac{\partial^2}{\partial \Omega \partial A} \left\{ \left(\int_{-\infty}^0 \psi \langle H_\Omega, H_{A\tau} \rangle d\tau \right) \mathcal{P} \right\} + \frac{\partial^2}{\partial \Omega^2} \left\{ \left(\int_{-\infty}^0 \psi \langle H_\Omega, H_{\Omega\tau} \rangle d\tau \right) \mathcal{P} \right\}. \end{aligned} \quad (2.40)$$

Substituting all the terms from Eq. (2.33)-(2.39) into Eq. (2.40) we obtain

$$\begin{aligned} \frac{\partial \mathcal{P}}{\partial t} = & - \frac{\partial}{\partial A} \left\{ \left(G_A + \frac{\Gamma}{4A\omega^2} \right) \mathcal{P} \right\} - \frac{\partial}{\partial \Omega} \{ G_\Omega \mathcal{P} \} \\ & + \frac{\partial^2}{\partial A^2} \left\{ \frac{\Gamma}{4\omega^2} \mathcal{P} \right\} + \frac{\partial^2}{\partial \Omega^2} \left\{ \frac{\Gamma}{4\omega^2 A^2} \mathcal{P} \right\}. \end{aligned} \quad (2.41)$$

Equation (2.41) is a Fokker-Planck equation which is simplified by means of averaging over the period of fast time scale $T = 2\pi/\omega$. Now, we would like to reconstruct stochastic equations in the form

$$\dot{A} = \tilde{G}_A(A, \Omega) + \tilde{H}_A(A, \Omega, \xi_1), \quad (2.42)$$

$$\dot{\Omega} = \tilde{G}_\Omega(A, \Omega) + \tilde{H}_\Omega(A, \Omega, \xi_2), \quad (2.43)$$

that would result in the simplified FP Eq. (2.41), if one wanted to construct it by following the Eq. (2.26). We find the expressions for \tilde{G}_A , \tilde{H}_A , \tilde{G}_Ω and \tilde{H}_Ω by comparing separate

terms of Eq. (2.41) with the corresponding terms of Eq. (2.40), considering that all the functions in the latter would be marked by tildes. We observe that

$$\int_{-\infty}^0 \langle \tilde{H}_A \tilde{H}_{\Omega\tau} \rangle d\tau = \int_{-\infty}^0 \langle \tilde{H}_\Omega \tilde{H}_{A\tau} \rangle d\tau = 0, \quad (2.44)$$

which can be true if the process \tilde{H}_A and \tilde{H}_Ω are not correlated. If Eq. (2.44) is true, then the two pairs of processes $\partial\tilde{H}_A/\partial\Omega$ and \tilde{H}_Ω , and $\partial\tilde{H}_\Omega/\partial A$ and \tilde{H}_A are not correlated that is

$$\int_{-\infty}^0 \left\langle \frac{\partial\tilde{H}_A}{\partial\Omega} \times \tilde{H}_{\Omega\tau} \right\rangle d\tau = \int_{-\infty}^0 \left\langle \frac{\partial\tilde{H}_\Omega}{\partial A} \times \tilde{H}_{A\tau} \right\rangle d\tau = 0. \quad (2.45)$$

Therefore we have

$$\tilde{G}_A + \int_{-\infty}^0 \psi \left\langle \frac{\partial\tilde{H}_A}{\partial A} \times \tilde{H}_{A\tau} \right\rangle d\tau = G_A + \frac{\Gamma}{4A\omega^2}, \quad (2.46)$$

$$\tilde{G}_\Omega + \int_{-\infty}^0 \psi \left\langle \frac{\partial\tilde{H}_\Omega}{\partial\Omega} \times \tilde{H}_{\Omega\tau} \right\rangle d\tau = G_\Omega. \quad (2.47)$$

Next we consider

$$\int_{-\infty}^0 \psi \langle \tilde{H}_A \times \tilde{H}_{A\tau} \rangle d\tau = \frac{\Gamma}{4\omega^2}, \quad (2.48)$$

which is an expression independent of A , and therefore $\partial\tilde{H}_A/\partial A = 0$. This leads to the disappearance of the integral in Eq. (2.46), and the final expression for \tilde{G}_A is

$$\tilde{G}_A = G_A + \frac{\Gamma}{4A\omega^2}. \quad (2.49)$$

Next, we consider

$$\int_{-\infty}^0 \psi \langle \tilde{H}_\Omega \times \tilde{H}_{\Omega\tau} \rangle d\tau = \frac{\Gamma}{4\omega^2 A^2}. \quad (2.50)$$

Here, the integral depends on A , but not on Ω , therefore the term involving $\partial/\partial\Omega$ vanishes, and \tilde{G}_Ω is given as

$$\tilde{G}_\Omega = G_\Omega. \quad (2.51)$$

Equation (2.48) and (2.50) are valid only if \tilde{H}_A and \tilde{H}_Ω can be expressed as

$$\tilde{H}_A = \frac{\sqrt{\Gamma}}{2\omega} \xi_1 \quad \text{and} \quad \tilde{H}_\Omega = \frac{\sqrt{\Gamma}}{2\omega A} \xi_2, \quad (2.52)$$

Where ξ_1 and ξ_2 represent a delta-correlated noise with zero mean and unity variance. In order for \tilde{H}_A and \tilde{H}_Ω to be uncorrelated, we need that ξ_1 and ξ_2 are uncorrelated, which is given as

$$\langle \xi_1(t)\xi_2(t + \tau) \rangle = 0. \quad (2.53)$$

Finally, we can write the simplified stochastic differential Eq. (2.23) as

$$\begin{aligned} \dot{A} &= - \left(-\frac{\mu_0}{2}A + \frac{\mu_2}{8}A^3 + \frac{\mu_4}{16}A^5 + \frac{5\mu_6}{128}A^7 \right) + \frac{\Gamma}{4A\omega^2} + \frac{\sqrt{\Gamma}}{2\omega}\xi_1, \\ \dot{\Omega} &= \frac{\sqrt{\Gamma}}{2\omega A}\xi_2. \end{aligned} \quad (2.54)$$

The objective of the reconstruction is to obtain the autonomous evolution equation for the slowly varying amplitude and the phase of the system. Here, the terms for the newly reconstructed form are obtained by equating terms of the FP equations for Eq. (2.42 & 2.43) and Eq. (2.24). We see that the final simplified form (Eq. 2.54) is helpful for stability analysis. At the beginning of the reconstructed form, the noise terms are taken as ξ_1 & ξ_2 , and upon equating the corresponding terms in FP equations (for Eq. 2.42 & 2.43 and Eq. 2.24), they turned out to be uncorrelated. Therefore, the terms \tilde{H}_A and \tilde{H}_ϕ are also uncorrelated. However, note that the reconstructed equations for amplitude A and phase ϕ are obtained in such a way that the joint probability density distribution of the original system and the reconstructed equation remain the same. Thus, despite the uncorrelated terms of \tilde{H}_A and \tilde{H}_ϕ , the equivalent nature of the reconstructed equations with the original system is ensured using the FP equation. Note that for a deterministic system ($\xi = 0$), the evolution of the phase is zero ($\dot{\Omega} = 0$), and now with the addition of noise, the phase drifts. Further, we note that the evolution of the amplitude envelope in Eq. (2.54) is a one-dimensional first-order differential equation, which can be analyzed using linear stability analysis. In further chapters, we utilize this method of stochastic averaging to illustrate the conditions for abrupt transitions.

2.2 RECURRENCE ANALYSIS

The behaviour of a dynamical system is often studied by analysing the evolution of the trajectory of the state variables (Strogatz, 2018). For instance, the behaviour of a pendulum can be investigated by visualizing the velocity of the pendulum as a function of displacement. The abstract graph, the evolution of state variables so obtained, is referred to as phase space trajectory. In order to effectively visualize this phase space trajectory, recurrence theory is used (Marwan and Kurths, 2002). A trajectory is said to be recurring at a location in phase space if it revisits the neighbourhood of the considered location (Eckmann *et al.*, 2017). A recurrence plot (RP) is constructed based on the recurrence matrix to visualize the recurrence of the system in its phase space. In this study, we use time delay embedding (Takens, 1981) to reconstruct the phase space trajectory from the signals measured during the experiments. The uniform delay embedding with a time delay τ and embedding dimension D is used to reconstruct the trajectory of the phase space. The value of τ is computed from the function of average mutual information (AMI) (Fraser and Swinney, 1986); the value of τ at the first minimum of AMI is considered as the optimum τ . The optimum dimension D is computed using the false nearest neighbourhood (FNN) method (Kennel *et al.*, 1992). Here, the delayed vector can be written as,

$$\mathbf{X}_i = [x_i, x_{i+\tau}, x_{i+2\tau} \dots x_{i+(D-1)\tau}]. \quad (2.55)$$

Here, i is varied from 1 to $N - (D - 1)\tau$, where N is the number of data points. To compute the recurrence matrix, initially, we compute the distance between the location i and all the other locations of the trajectory in phase portrait. Further, we choose a distance threshold ϵ and consider only those points to compute the recurrence matrix whose Euclidean distance is less than the threshold ϵ . The threshold ϵ can be chosen such that the number of neighbouring locations is a small part of the total span of the attractor or choose a value such that each point has a fixed number of neighbours (Marwan, 2011).

The equation for calculating the recurrence matrix R_{ij} is provided as,

$$R_{ij} = \Theta (\epsilon - \|\mathbf{X}_i - \mathbf{X}_j\|), \quad (2.56)$$

where Θ is the Heaviside step function. If the Euclidean distance $\|\mathbf{X}_i - \mathbf{X}_j\|$ is less than the threshold ϵ , then the element of the matrix R_{ij} is equal to one, else R_{ij} is equal to zero. Entry 1 in the recurrence matrix corresponds to a recurrent state, which implies that the trajectory is revisiting its neighbourhood. Thus, several distinct patterns can be observed based on the type of dynamical state (Marwan and Kurths, 2002). For instance, Fig. 2.2 represents the different patterns observed in the recurrence plot during the state of chaos (aperiodic oscillations), intermittency and limit cycle oscillations. For periodic dynamics, the recurrence plot consists of equipaced diagonal lines. The distance between the diagonal lines represents the time period of the oscillations. Furthermore, for the dynamical states such as quasi-periodic oscillations, the distance between the diagonal lines varies (Marwan and Kurths, 2002). Thus, recurrence plots help in gaining useful insights into many dynamical states exhibited by a system.

2.2.1 Recurrence quantification analysis (RQA)

In order to quantify the changes in dynamical states, we extract information from the topology of the recurrence plot using recurrence quantification measures. These measures are based on the statistics of the distribution of the points in the recurrence plots. Several RQA measures have been developed based on the type of insights required to study the dynamical systems (Marwan and Kurths, 2002). In this study, we use recurrence rate (RR) and determinism (DET) measures to illustrate the dynamics of an aeroacoustic system.

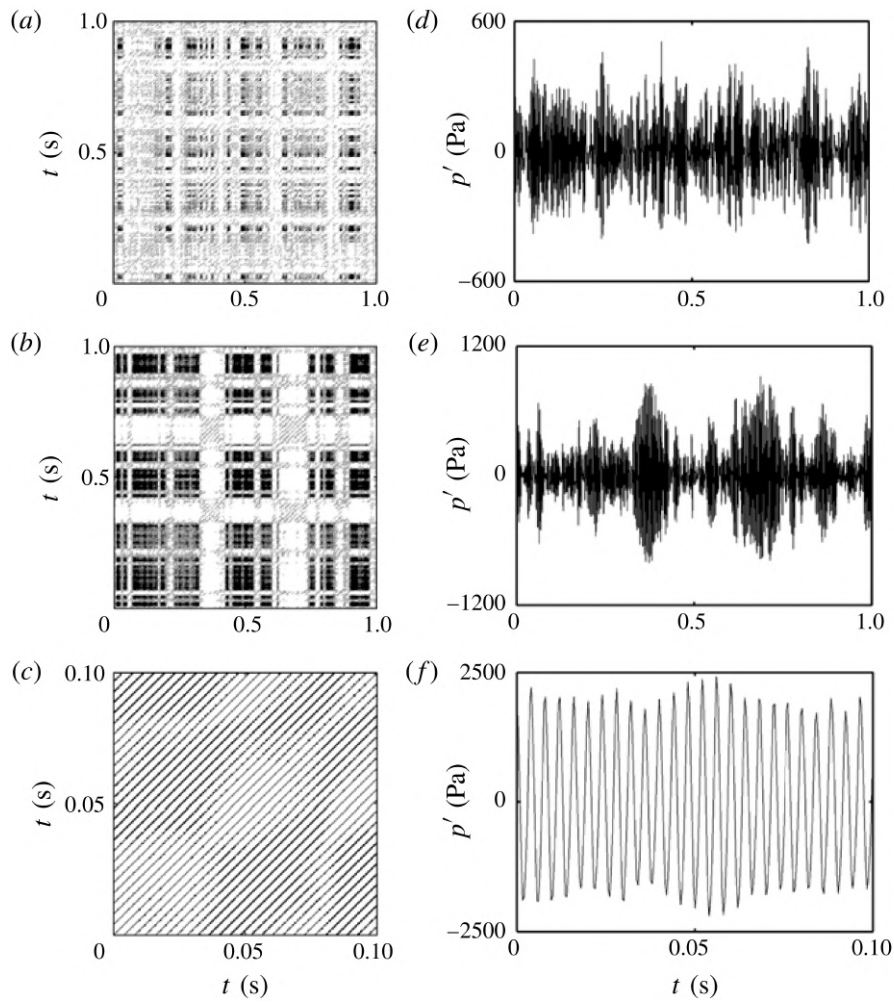


Figure 2.2: Representation of the patterns from the recurrence matrix for the states of (a) chaos, (b) intermittency and (c) LCO. This figure is reproduced with permission from Nair *et al.* (2014), *J. Fluid Mech.* 756, 470–487 (2014), published by Cambridge University Press.

Recurrence rate RR

The recurrence rate is a measure of the density of black points, i.e., the points that recur in the RP (Marwan *et al.*, 2007). The equation for RR is given as,

$$RR(\epsilon) = \frac{1}{N^2} \sum_{i,j=1}^N R_{i,j}(\epsilon). \quad (2.57)$$

Here, N is the overall number of points in the trajectory. RR attains the maximum value of 1 when the points in the phase space trajectory are recurring. For a clean limit cycle oscillations, the value of RR is near 1. In contrast, for an aperiodic signal, the points in the recurrence plot are sparsely spaced, having a very low value of $RR \approx 0$.

Determinism DET

Determinism DET quantifies the periodic dynamics of the system and is given as,

$$DET = \frac{\sum_{l=l_{min}}^N lF(l)}{\sum_{l=1}^N lF(l)}, \quad (2.58)$$

where $F(l)$ is the distribution of the length of the diagonal lines in the recurrence plot. DET represents the fraction of recurrence points in the RP that forms the diagonal lines. For clean limit cycle oscillations, the value of DET is equal to 1. DET is helpful in quantifying the difference between the periodic and quasi-periodic dynamics.

2.3 SYNCHRONISATION ANALYSIS

The phenomenon where the rhythm of the subsystems matches upon coupling is referred to as synchronisation. In 17th century, Christiaan Huygens discovered the universal phenomenon of synchronisation when he observed that pendulum clocks hung on a wall synchronised their oscillations (Huygens, 1665; Pikovsky *et al.*, 2003). In the following years, this phenomenon of synchronisation is reported in various domains, such as chemistry (Schreiber and Marek, 1982), biology (Glass, 2001), ecology (Blasius *et al.*, 1999), and engineering (Roy and Thornburg Jr, 1994; Heagy *et al.*, 1994; Pawar *et al.*, 2017). Synchronisation among the oscillators is generally confirmed by the locking of

frequency (or phase) of the oscillators. The coupling strength between the oscillators is an important parameter that decides the arrival of two oscillators to a state where they have constant phase differences.

The phenomenon of synchronisation can be observed in both periodic (Blekhman *et al.*, 1995) and chaotic oscillators (Boccaletti *et al.*, 2002). Initially, desynchronised coupled oscillators that exhibit chaotic oscillations can enter into the synchronised state of chaotic oscillations. Such chaotic synchronisation occurs by means of variation in coupling strength (Boccaletti *et al.*, 2002), or feedback (Wang *et al.*, 2001). However, the possibility of the simultaneous existence of different coupling mechanisms makes it difficult to identify the influence of individual mechanisms on the dynamics of the system.

The features of synchronisation have been observed in complex fluid mechanical systems as well (Zdravkovich, 1982; Gunnoo *et al.*, 2016). When a bluff body is placed against the fluid flow, vortices are shed in its wake region. The shedding vortex perturbs the bluff body, which in turn affects the shedding. When the natural frequency of the bluff body oscillation is near the shedding frequency of the vortex, the vortex shedding frequency locks with the bluff body oscillations. The mutual interactions between the flow and the bluff body during the lock-in control the shedding patterns of large-scale structures (Griffin and Ramberg, 1974; Blevins, 1985; Williamson and Roshko, 1988; Griffin and Hall, 1991). The synchronisation phenomenon is also reported in thermoacoustic systems (Pawar *et al.*, 2017; Godavarthi *et al.*, 2018; Kasthuri *et al.*, 2022). Here the synchronisation between the unsteady heat release rate and the chamber acoustics leads to the state of self-sustained oscillations, referred to as thermoacoustic instability. Turbulent flow systems can also be regarded as complex systems (Pavithran *et al.*, 2020). Complex systems consist of subsystems that interact with each other, giving rise to emergent dynamics. In this study, we consider acoustics and hydrodynamics as two subsystems and investigate the coupled behaviour between these two subsystems using synchronisation theory.

In the current study, we investigate whistling (aeroacoustic instability) as a synchronisation phenomenon between two nonidentical subsystems. We use velocity u' and acoustic pressure p' fluctuations measured from the aeroacoustic system to investigate the synchronisation phenomenon.

2.3.1 Joint recurrence matrix

The joint recurrence matrix (JRM) can be considered as an extension of the recurrence matrix to investigate the coupled dynamics of the two subsystems. A joint recurrence matrix helps visualize the recurrence of the phase space trajectories of two different subsystems at the same time (Goswami *et al.*, 2013; Marwan and Kurths, 2002; Romano *et al.*, 2004).

The JRM for two subsystems having the time-delayed vectors \mathbf{X} and \mathbf{Y} is calculated by computing the element-wise product of the individual recurrence matrices (R^X , R^Y). The equation for JRM can be written as,

$$JRM_{ij} = \Theta(\epsilon - \|\mathbf{X}_i - \mathbf{X}_j\|) \Theta(\epsilon - \|\mathbf{Y}_i - \mathbf{Y}_j\|). \quad (2.59)$$

If the trajectories \mathbf{X} and \mathbf{Y} of the two subsystems recur simultaneously, then $JRM_{ij} = 1$ else, $JRM_{ij} = 0$.

Further, one can also quantify the topology of the joint recurrence plots using the RQA measures recurrence rate RR_j and determinism DET_j . Note that the values and variations of these recurrence measures depend on how we define the recurrence threshold ϵ while computing the recurrence matrix. For instance, if a fixed ϵ is chosen, there are more number of recurrence points within the radius of ϵ for the low-amplitude aperiodic trajectory. Hence, we observe that the measure RR rises as the system exhibits the states of low amplitude intermittency and aperiodicity. In contrast, if ϵ is chosen as a fraction of the maximum diameter of the phase space, the measure RR decreases for the states of intermittency and aperiodic dynamics. The decrease in RR is due to the sporadic

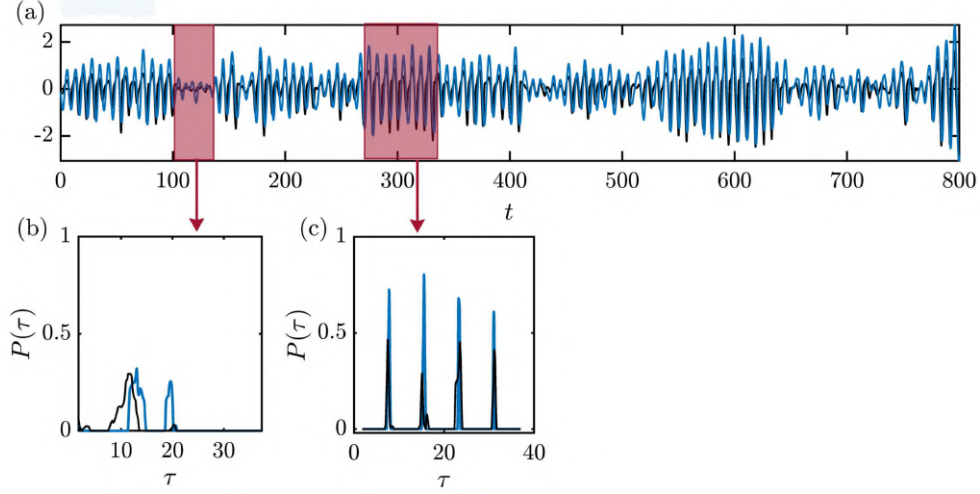


Figure 2.3: Representation of the variation of the probability of recurrence $P(\tau)$ as a function of time lag τ . $P(\tau)$ variations for two different signals, represented as black and blue curves are overlapped to identify the type of synchronisation at different time intervals for the states of intermittency. (b) During an aperiodic epoch, there is no overlap in the variations of $P(\tau)$ for the blue and black signals, implying there is no relationship between the two signals. However, during the (c) periodic epoch, there is an overlap between the curves of $P(\tau)$, implying a phase synchronisation between the two signals. This figure is reproduced with permission from Godavarthi *et al.* (2020), *Chaos* 30, 033121 (2014), published by AIP Publishing.

recurrence of the trajectory for the states of intermittency and aperiodicity (Godavarthi *et al.*, 2018).

2.3.2 Probability of recurrence

In synchronisation theory, it is important to identify the type of synchronisation that is exhibited by the system. Hence, one can make use of the probability of recurrence to identify the type of synchrony that persists between the variables or the subsystems of the system being measured. The probability of recurrence quantifies the probability with which a state vector of the trajectory recurs after a time lag τ (Romano *et al.*, 2005), and is given as,

$$P(\tau) = \frac{1}{N - \tau} \sum_{i=1}^{N-\tau} \Theta(\epsilon - \|\mathbf{X}_i - \mathbf{X}_{i+\tau}\|). \quad (2.60)$$

A recurrence of the signal is equivalent to an increment in phase by 2π (Romano *et al.*,

2005). The synchronisation of the two coupled subsystems implies the locking of their phases and frequencies. This locking of phase leads to the simultaneous appearance of the apexes of $P(\tau)$ of two signals in the plots of probability of recurrence. The state is referred to as a synchronised state (PS) when the frequencies of the two signals are locked, and their amplitude remains uncorrelated (refer to Fig. 2.3). The PS state manifests as the simultaneous occurrence of the peaks, but with unequal heights, in the plots of probability of recurrence as a function of time lag. On the contrary, if a functional relationship exists between the subsystems, the apexes of $P(\tau)$ for the subsystems occur simultaneously, and also, the magnitude of the peaks are matched; this state is referred to as generalized synchronisation (GS). For the state of GS, the RP and hence the probability of recurrence plots will be identical (Lakshmanan and Senthilkumar, 2011). The states of PS and GS are experimentally discovered by Pawar *et al.* (2017) in thermoacoustic systems

CHAPTER 3

EXPERIMENTAL SETUPS AND DIAGNOSTICS

In order to study the generic attributes of the transitions to high amplitude oscillatory instabilities in aero-thermoacoustic systems, we perform experiments in different experimental configurations of thermoacoustic and aeroacoustic systems. In this chapter, we discuss the experimental facilities and diagnostics used for conducting experiments and acquiring data related to the results presented in this thesis.

The data for studying abrupt transitions in turbulent thermoacoustic systems (Chapter 4) was obtained from the following sources:

1. Data set for a turbulent annular combustor having the abrupt transition via secondary bifurcation was acquired by a team consisting of Dr. Samarjeet Singh, Dr. Amitesh Roy, Mr. Midhun P. R. and Prof. R. I. Sujith in the year of 2019. Please refer to Singh *et al.* (2021) for more details on the data.
2. Data set for a bluff body stabilised backward-facing step combustor with preheater having the abrupt transition via secondary bifurcation was acquired by a team consisting of Dr. Samadhan A. Pawar, Dr. Manikandan Raghunathan, Mr. Midhun P. R., Ms. Reeja K. and Prof. R. I. Sujith in the year of 2019. Please refer to Pawar *et al.* (2021) for more details on the data.

3.1 THERMOACOUSTIC SYSTEMS

The transitions to undesired high-amplitude oscillatory instabilities are investigated in three different turbulent thermoacoustic systems. These systems function under turbulent conditions and represent the dynamics of combustors in modern gas turbines and rocket engines. The details of the combustor setups are discussed below.

3.1.1 Backward facing step combustor configurations

Figure 3.1(a) represents the experimental setup for the backward facing step combustor. This test rig was previously used by Nair and Sujith (2014). A fluid mixture of compressed air and liquid petroleum gas (60% Propane & 40% butane) is used for chemical reactions in a combustion chamber. The combustion chamber is 1100 mm long and has a 90×90 mm² square cross-section. The setup has three main sections along the fluid flow—a plenum chamber, a burner, and the combustion chamber. The air enters the combustor via a flow equalization chamber referred to as a plenum chamber, which helps isolate the combustion chamber from the fluctuations upstream of the flow. The fuel is injected in the burner section between the plenum chamber and the combustion chamber, where the fuel and the air are premixed. The diameter of the burner is 40 mm. The fuel-air mixture enters the combustion chamber at the dump plane, where there is a sudden increase in the cross-sectional area from the burner to the combustion chamber. The end of the combustion chamber is fixed to a large rectangular box referred to as a decoupler. The dimensions of the decoupler are set to be larger than the cross-sectional size of the combustion chamber. The utility of the decoupler is to reduce sound emissions from the combustion chamber (Zinn, 1996).

The equivalence ratio ϕ is varied as a control parameter to study the dynamics of the system. The equivalence ratio is defined as $\phi = \dot{Y}_{\text{actual}} / \dot{Y}_{\text{stoichiometric}}$, where \dot{Y} is the ratio of the rate of the mass flow of the fuel and the air. Thus, ϕ is a function of fuel and airflow rates, which are controlled using mass flow controllers (MFCs). The uncertainty in the flow rate measurement is $\pm 1\%$. The uncertainty in the computed value of ϕ is $\pm 2\%$. The control parameter (ϕ) is changed in a quasi-static manner. To minimize the error in flow rate measurement and to achieve the finer steps of variation in the control parameter (airflow rate) at the bifurcation regime, two different MFCs are connected in parallel. The maximum range of these MFCs is 2000 and 100 SLPM, and the corresponding error in their main scale reading is 4 and 0.2 SLPM, respectively. The qualitative change in the behaviour of the system is analysed by measuring the acoustic pressure fluctuations

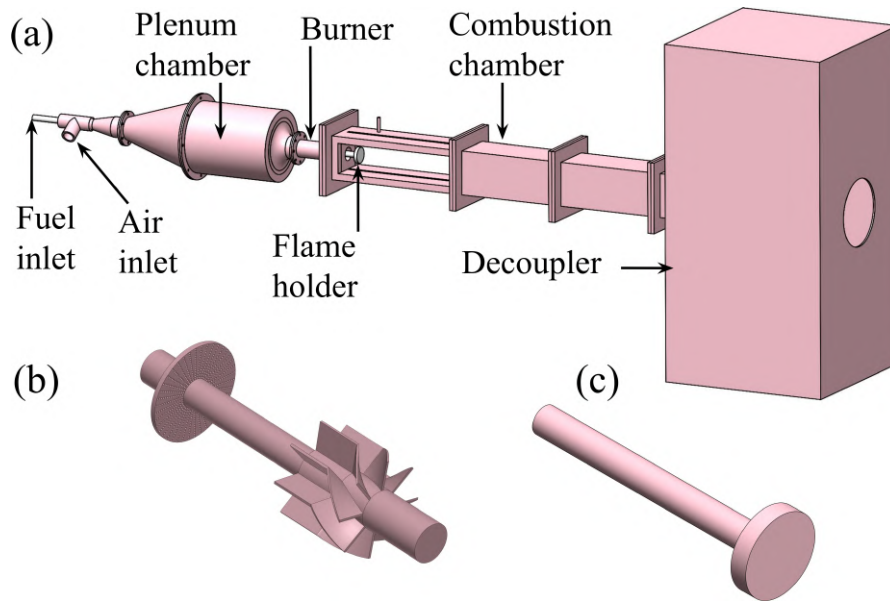


Figure 3.1: Schematic of (a) a backward facing step combustor which can be operated in two different configurations based on the flame holding mechanisms. (b) The swirler and (c) the bluff body are used as two different flame holders for the backward facing step combustor. The design of this combustor was adapted from Komarek and Polifke (2010)

in the combustion chamber. Piezoelectric pressure transducers (PCB103B02, 217.5 mV/kPa sensitivity) are used to measure acoustic field fluctuations. We acquire the acoustic pressure signal for 5 s at a rate of 10000 samples per second, after an initial waiting time of 3 s at each set point of the control parameter. The measured acoustic pressure signal has an uncertainty of 0.15 Pa in its value. We performed experiments in two different configurations of the backward facing step combustor, which will be detailed in the following subsections.

Backward facing step combustor with a swirler configuration

A swirler (refer to Fig. 3.1b), inducing swirl motion to the flow, is used at the entry of the combustion chamber. The swirling motion aids in the establishment of the flame in a compact form, stretching over a small section of the combustion chamber. The diameter (d) of the swirler is 40 mm. The swirler consists of 8 vanes, and the vane-angle is 40° relative to the direction of the bulk flow in the combustor. The location of the

swirler is such that the front part of each vane is 20 mm from the dump plane. In this swirler configuration, we maintain a constant fuel flow rate. The equivalence ratio is varied by changing the airflow rate. The Reynolds number for the system varies between $Re_d = 2 \times 10^4 \pm 220$ and $5 \times 10^4 \pm 220$. Here, the Reynolds number is defined as $Re = \rho \bar{v} D / \Lambda$, where \bar{v} is the average velocity of the fuel-air mixture entering the combustion chamber, D is the diameter of the swirler, ρ and Λ are the density and dynamic viscosity of the mixture. A K-type thermocouple is used to measure the temperature of the hot gases downstream of the flow. The signal for the temperature was acquired for 5 s at a rate of 20 samples per second.

Backward facing step combustor with a bluff body configuration

In this configuration of the backward facing step combustor, we replace the earlier flame holder (swirler) with a bluff body (refer to Fig. 3.1c). A bluff body slows the flow by creating a flow re-circulation zone, providing sufficient time for the air-fuel mixture to react in a compact zone of the combustion chamber (Chen *et al.*, 1990). The bluff body is located at a distance of 27.5 mm from the dump plane of the combustion chamber. The diameter (d) of the bluff body is 47 mm. The fuel for the combustor is introduced in the burner via a hollow shaft anchoring the bluff body. We maintain a constant fuel flow rate in this bluff body configuration. The equivalence ratio is varied by changing the airflow rate. The corresponding Reynolds number, computed using the diameter of the bluff body, varies in the range of $Re_d = 1.5 \times 10^4 \pm 220$ to $4 \times 10^4 \pm 220$.

3.1.2 Annular combustor

Figure 3.2(a) represents a swirl-stabilized annular combustor, where sixteen flames from the circumferentially arranged burners are established during the experiments. This test rig was previously used by Singh *et al.* (2021); Roy *et al.* (2021). Premixed LPG and air are used for chemical reactions. The air and the fuel initially enter a premixing chamber through an air/fuel inlet. The premixed mixture then enters into a flow-settling chamber. We incorporate a honeycomb-like structure inside the settling chamber to render the

flow in one direction. The flow through the settling chamber encounters a hemispherical flow divider that uniformly distributes the fuel-air mixtures to the 16 burner tubes. The burner tubes exit into the combustion chamber, which has an outer and inner cylindrical duct. The chemical reactions are individually established in the annulus of the outer and the inner cylindrical duct after passing through the swirler fitted at the exit of each burner tube. The swirlers consist of vanes whose vane angle β is 60° with the axial flow direction (refer to Fig. 3.2b). The burner tubes are 300 mm long and have a circular cross-section (30 mm diameter). The diameter of the inner and the outer cylindrical ducts are 400 mm and 300 mm, respectively. The length of the inner and the outer cylindrical ducts are 510 mm and 140 mm, respectively.

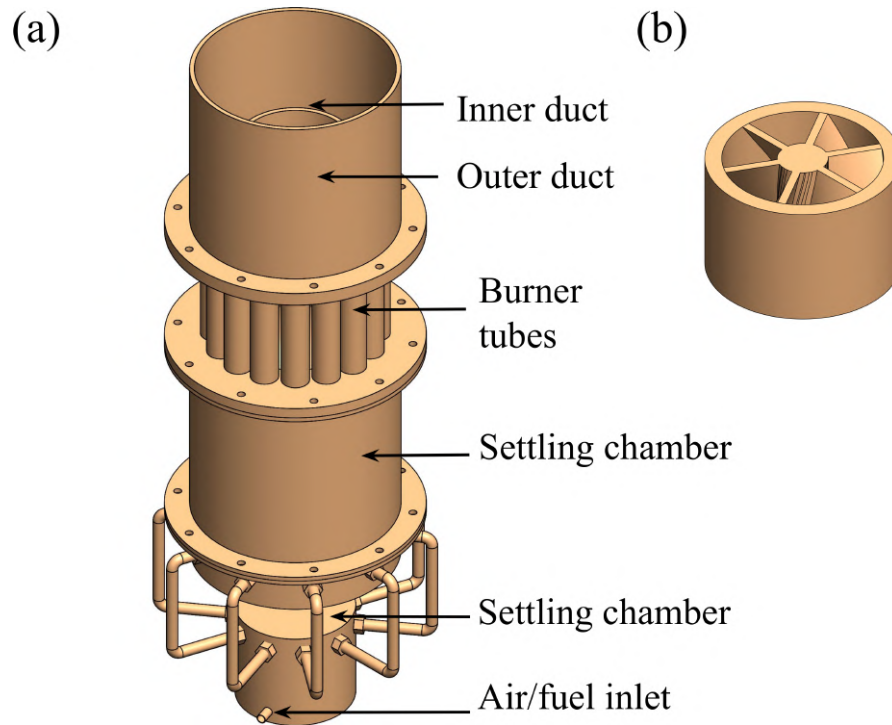


Figure 3.2: Schematic of (a) the annular combustor comprising sixteen burners. At the exit of each burner, (b) a swirler is used as a flame holder.

In this annular combustor setup, we vary the fuel flow rate to change the equivalence ratio (ϕ) at a constant airflow rate. The Reynolds number of this turbulent system is $Re_d \approx 1.01 \times 10^4 \pm 220$, computed based on the burner dimensions. The dynamics of the system is analysed by measuring the fluctuations of the acoustic field signal inside

the combustion chamber. Piezoelectric pressure transducers (PCB103B02) of sensitivity 217.5 mV/kPa are used for pressure fluctuation measurements. The pressure signal at each control parameter is acquired for 5 s at a rate of 10000 samples per second, after an initial waiting time of 3 s at each set point of the control parameter. A K-type thermocouple is used to measure the temperature of the hot gases downstream of the flow.

3.2 AEROACOUSTIC SYSTEM

In this study, we also investigate the transitions to oscillatory instabilities in an aeroacoustic system. The schematic of the experimental setup used for the study is presented in figure 3.4. The airflow enters the plenum chamber through an inlet port. The plenum chamber is connected to a circular duct (610 mm length and 50 mm diameter), which has the facility to bolster two orifices (20 mm orifice diameter and 2.5 mm thickness). The distance between the orifices is 18 mm, and the first orifice, located upstream of the flow, is 220 mm away from the plenum chamber. A hot film probe, positioned between the orifices using a mount, measures the velocity fluctuations. A microphone, mounted on the wall of the pipe at a distance of 305 mm from the plenum chamber, is utilized to quantify the acoustic pressure oscillations.

Experiments are conducted at the room temperature of 25 °C. The control parameter of the system is the Reynolds number (Re), which is varied. Re is computed using the formula $Re = (\rho \bar{u} l_c) / \Lambda$, where \bar{u} is the horizontal bulk flow velocity at the orifice, ρ is the air density (kg/m³), l_c is the characteristics length which is equal to the diameter of the orifice, and Λ is the dynamic viscosity of the air. The airflow rate is varied using an Alicat (MCR series) mass flow controller (MFC) with a measurement uncertainty of $\pm(0.8\%$ of reading + 0.2% of the full-scale reading). The maximum error in Re is ± 170 , which is associated with the measurement uncertainty of the MFC. The airflow rate is changed in a quasi-static fashion from 57 SLPM to 300 SLPM in steps of 3 SLPM. This

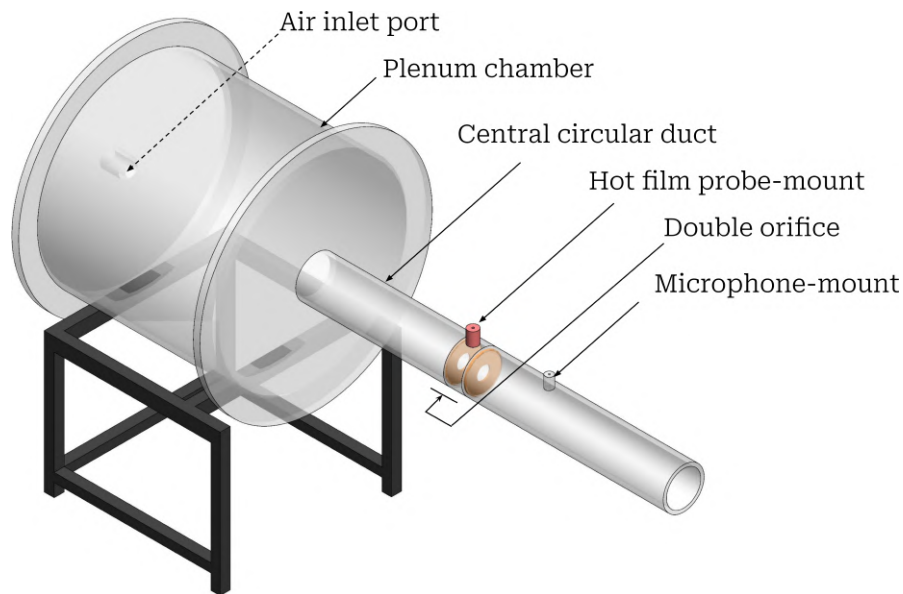


Figure 3.3: Schematic of the aeroacoustic system, which has a confined flow through the double orifices.

corresponds to the variation of Re from 3900 ± 101 to 21000 ± 235 . A pressure field pre-polarized microphone (Piezotronics PCB378C10), which has a preamplifier system and a condenser, is used for measuring acoustic pressure fluctuations. The microphone has a sensitivity of 1 mV/Pa and a resolution of $20 \mu\text{Pa}$. The data from the microphone is acquired for 5 s at a sampling rate of 20 kHz. The inherent noise in the measurements from the microphone is 7 mPa.

The velocity fluctuations, u' , are measured using a hot film probe connected to the constant temperature anemometer (Dantec Dynamics, Multi-channel CTA-54N81). Since the source of the sound for whistling is at the orifice and is a dipole source, only those modes which have velocity antinode near the location of the source are favoured (Hirschberg and Rienstra, 2004). Please refer to Appendix B.1 for more information on the mode shapes of the observed dominant frequencies during whistling. Thus, the hot film probe is located near the velocity anti-node of the excited modes and at a radial distance of 1 cm from the centre of the cross-sectional area of the pipe. The location of the probe is chosen such that we capture the fluctuations caused by turbulence or vortical structures

emerging from the orifice (Mettenleiter *et al.*, 2000). The measured fluctuations from the hot-film probe have contributions from both the acoustics and the hydrodynamic fields. When there is no whistling, the influence of the acoustic field over the hydrodynamic field is negligible, as there is no lock-in between the hydrodynamic and acoustic fields.

3.3 ACOUSTIC DECAY RATE

We monitored the acoustic damping of the aeroacoustic and thermoacoustic systems. The experiments were conducted only when the damping fell within a specified range to ensure repeatability. The decay rate, representing acoustic damping, was maintained at the following values during the experiments:

1. Aeroacoustic system: $-9.3 \pm 2 \text{ s}^{-1}$
2. Backward-facing step combustor: $-7.8 \pm 2 \text{ s}^{-1}$
3. Annular combustor: $-31.5 \pm 2 \text{ s}^{-1}$

All the experimental configurations used in this study utilize compressed air stored in an external tank. Changes in ambient conditions, such as heavy rainfall, can affect the temperature and humidity of the airflow used in the experiments, thereby influencing the acoustic damping properties of the aero-thermoacoustic systems. The specified decay rate ranges were intuitively determined based on the experimental and ambient conditions. To calculate the decay rates, we externally perturb the aero-thermoacoustic system at its natural frequency and measure the rate at which the acoustic pressure oscillations decay after the perturbation ceases (Perry, 1970; Culick and Kuentzmann, 2006).

Under no-flow conditions, the aeroacoustic system, backward-facing step combustor and annular combustor are perturbed at 260 Hz, 240 Hz and 410 Hz, respectively. External acoustic forcing is applied using loudspeakers (Minsound TD-200A) connected in parallel to a power amplifier (Ahuja UBA-500M). The sinusoidal forcing signal required for this process is generated using a Tektronix function generator (Model No. AFG1022). We capture the evolution of acoustic pressure oscillations after generating the sinusoidal

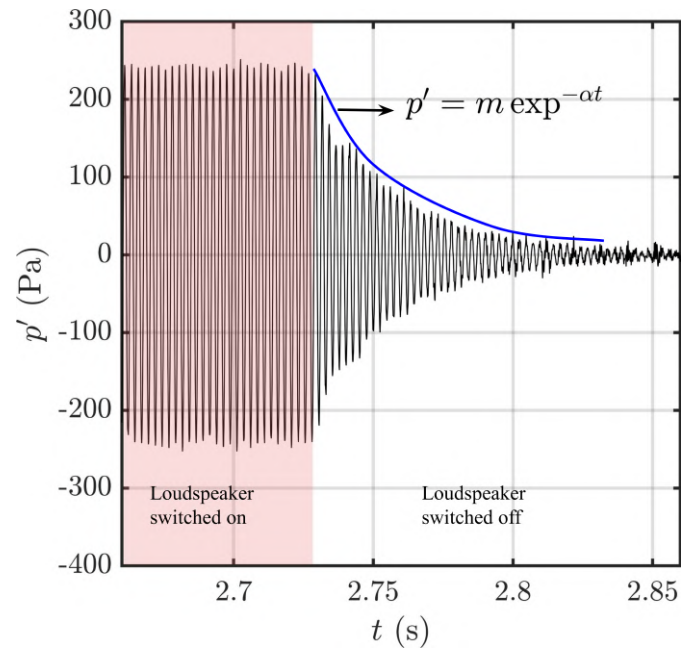


Figure 3.4: The representation of the acoustic pressure oscillations under no-flow conditions, both before and after the abrupt shutdown of the loudspeaker. We extract the envelope of the decaying pressure oscillations and fit an exponential curve, represented in the form of $p' = m \exp^{-\alpha t}$. Here, α represents the decay rate corresponding to the decaying portion of the acoustic signal immediately after turning off the loudspeaker

pressure disturbance and abruptly switching off the acoustic drivers. The envelope of the decaying oscillations is extracted using the Hilbert Transform. A straight line is then fitted to the semi-logarithmic plot of the envelope, with the slope of this plot representing the decay rate of the thermoacoustic system.

CHAPTER 4

ABRUPT TRANSITIONS IN TURBULENT THERMOACOUSTIC SYSTEMS

Thermoacoustic instability (TAI) manifests as large amplitude periodic pressure oscillations. These periodic oscillations are also referred to as limit cycle oscillations. Lieuwen (2002) described the transition from stable combustor operation to unstable combustor operation of TAI as a Hopf bifurcation from a fixed point to a limit cycle solution. Several experimental studies have since then reported supercritical and subcritical bifurcation to the state of limit cycles (Moeck *et al.*, 2008; Li *et al.*, 2017; Juniper, 2012; Etikyala and Sujith, 2017; Subramanian *et al.*, 2010; Guan *et al.*, 2020). However in turbulent combustors, the study by Nair *et al.* (2014) showed that the state of intermittency occurs as a route to thermoacoustic instability from the stable operating condition characterized by the state of chaos. Further, the state of intermittency observed is described as the epochs of periodic oscillations amidst the regime of aperiodic oscillations. The study also discusses the mechanism for such a kind of intermittency, which is due to back-and-forth fluctuations of the parameters or the subsystems caused by turbulence fluctuations. Further, it is a great challenge to model the dynamics of chaos and the state of intermittency incorporating the deterministic turbulent fluctuations. Therefore, several studies have incorporated the effect of turbulent aperiodic fluctuations by perturbing the system with noise.

Moreover, the occurrence of intermittency leads to a smooth variation of the statistical measures of the system, such as the root-mean-squared (rms) or Fourier amplitude, as the state of the system changes from a state of combustion noise to TAI. Past studies

The results presented in this chapter are published in Bhavi, R. S., Pavithran, I., Roy, A., and Sujith, R. I. (2023), Abrupt transitions in turbulent thermoacoustic systems, *Journal of Sound and Vibration*, 547, 117478. <https://doi.org/10.1016/j.jsv.2022.117478>

were focused on gradual transitions in turbulent combustors. However, recently, abrupt transitions have been discovered in turbulent thermoacoustic systems (Roy *et al.*, 2021; Singh *et al.*, 2021; Wang *et al.*, 2021). The observation of abrupt transitions in highly turbulent thermoacoustic systems is not understood clearly. Specifically, the explanation of what makes a transition continuous or abrupt has been found lacking in the literature.

4.1 EXPERIMENTAL OBSERVATION OF ABRUPT SECONDARY BIFURCATIONS

The experimental data for studying abrupt transitions in this chapter was obtained from the following sources:

1. Data set for a turbulent annular combustor having the abrupt transition via secondary bifurcation was acquired by a team consisting of Dr. Samarjeet Singh, Dr. Amitesh Roy, Mr. Midhun P. R. and Prof. R. I. Sujith in the year of 2019. Please refer to Singh *et al.* (2021) for more details on the data.
2. Data set for a bluff body stabilised backward facing step combustor with preheater having the abrupt transition via secondary bifurcation was acquired by a team consisting of Dr. Samadhan A. Pawar, Dr. Manikandan Raghunathan, Mr. Midhun P. R., Ms. Reeja K. and Prof. R. I. Sujith in the year of 2019. Please refer to Pawar *et al.* (2021) for more details on the data.

We begin by considering the characteristics of the bifurcation when the equivalence ratio (ϕ) is changed in these turbulent combustors. Figure 4.1(a) depicts the variation in p'_{rms} when the control parameter ϕ is increased in the annular combustor. For low values of equivalence ratio ($\phi < 0.8$), the state of the system is characterised by combustion noise (cf. Fig. 4.1b) possessing very low amplitude ($p'_{\text{rms}} \approx 20$ Pa) of fluctuations. The fluctuations are characterised by a unimodal distribution and a broadband spectrum. Upon increasing the equivalence ratio (ϕ) beyond a value of 0.8, the state of intermittency is observed, where aperiodic fluctuations are randomly interspersed with bursts of periodic oscillations (cf. Fig. 4.1c). The appearance of periodic bursts, whose amplitude is higher than the amplitude of combustion noise, alters the initially unimodal distribution; we observe secondary peaks at $|p'| \neq 0$ (see PDF in Fig. 4.1c). The increased periodic

content appears as a narrowband peak in the amplitude spectrum. Upon further increasing the value of ϕ , the state of low amplitude limit cycle oscillations (LCO) with $p'_{\text{rms}} \approx 373$ Pa is observed. The limit cycle oscillations show (cf. Fig 4.1d) a bi-modal distribution and a narrowband peak in the amplitude spectrum at 220 Hz. Finally, for $\phi > 0.87$, we observe (cf. Fig 4.1e) an abrupt transition from the low amplitude primary limit cycle oscillations to a large amplitude ($p'_{\text{rms}} \approx 1500$ Pa) secondary limit cycle oscillations.

Figure 4.2 shows the characteristics of abrupt transition to large amplitude limit cycle oscillation in the swirl-stabilized and preheated bluff-body stabilized combustor as ϕ is decreased. The transition is observed when ϕ is decreased from 0.99 to 0.54 in a quasi-static manner in the swirl-stabilized combustor, while it is observed for a decrease in ϕ from 1.09 to 0.62 in the preheated bluff-body stabilized combustor. In each of these two combustors, a decrease in ϕ leads to a transition from combustion noise to high-amplitude TAI through the states of intermittency and low-amplitude limit cycle oscillations. These states in the swirl and bluff-body combustor have similar statistical properties to the representative plots shown in Fig. 4.1(b-e). The abrupt transition, thus, takes place through a secondary bifurcation to large amplitude limit cycle oscillations. Note that the swirl-stabilized backward facing step combustor depicts secondary bifurcation to very large amplitude levels ($p'_{\text{rms}} \approx 4$ kPa). Thus, it is evident from Figs. 4.1 and 4.2 that these turbulent thermoacoustic systems exhibit abrupt transitions in the form of secondary bifurcations. Secondary bifurcation appears in disparate turbulent combustion systems with very different flame and acoustic responses. Thus, the common phenomenology across disparate combustors implies a certain universal mechanism through which secondary bifurcation occurs in turbulent combustors. Motivated by these results, a mathematical model, as discussed in Chapter 2, is considered for describing secondary bifurcations. The equation is given as,

$$\ddot{\eta} + \left(\mu_6 \eta^6 + \mu_4 \eta^4 + \mu_2 \eta^2 - \mu_0 \right) \dot{\eta} + \omega^2 \eta + \xi = 0, \quad (4.1)$$

where μ_0 is the control parameter and μ_2 , μ_4 , and μ_6 are the coefficients of the nonlinear

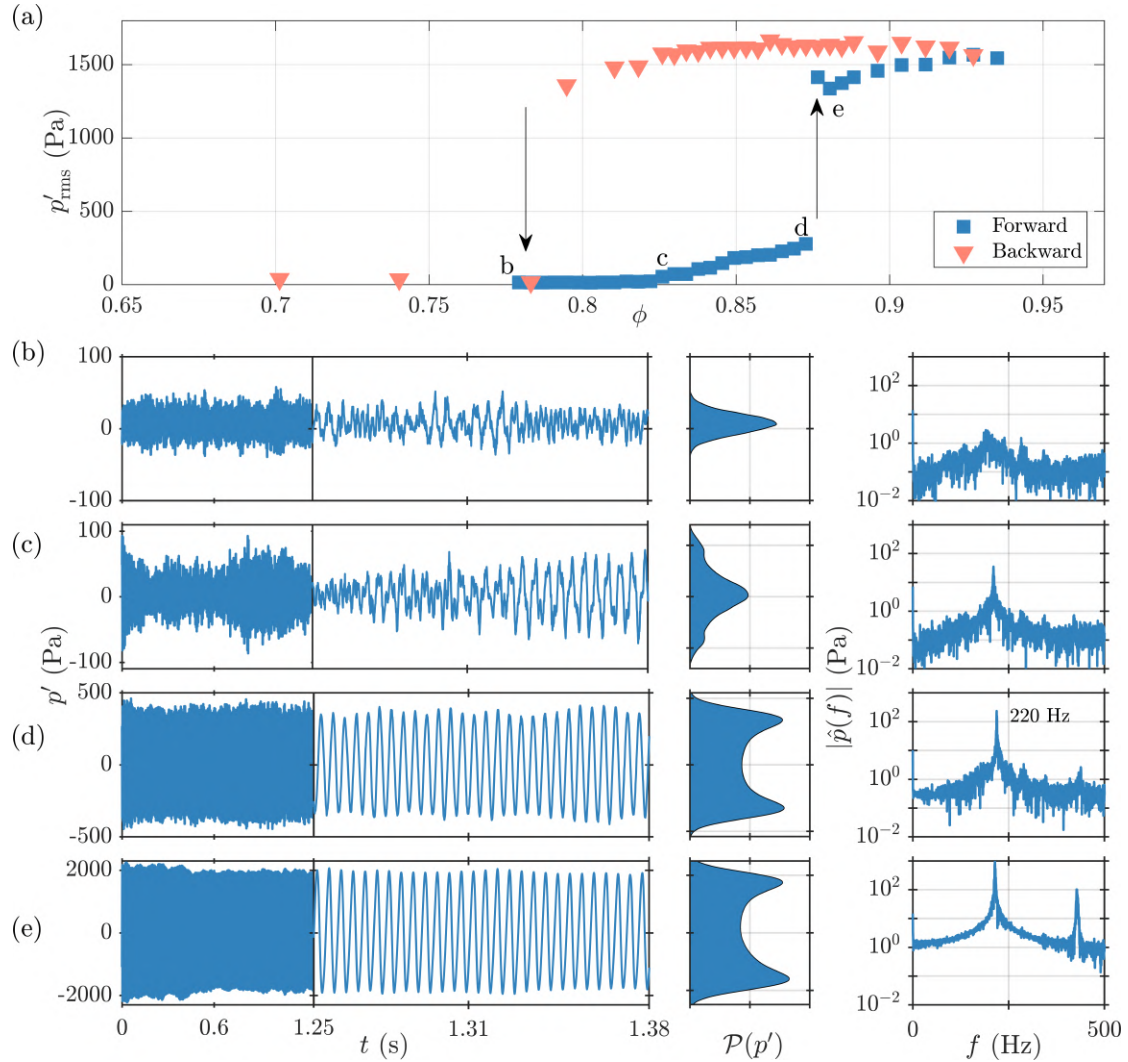


Figure 4.1: Characteristics of secondary bifurcation in the annular combustor. (a) The variation of p'_{rms} as a function of the control parameter ϕ . Panels (b-e) shows the time series, the PDF $\mathcal{P}(p')$ and the amplitude spectrum $|\hat{p}(f)|$ of pressure fluctuations p' observed during the states of (b) combustion noise, (c) intermittency, (d) low amplitude limit cycle oscillations and (e) large amplitude limit cycle oscillations, as indicated in panel (a). Note the increase in the abscissa limits for the time series and distribution in panels (b) to (e).

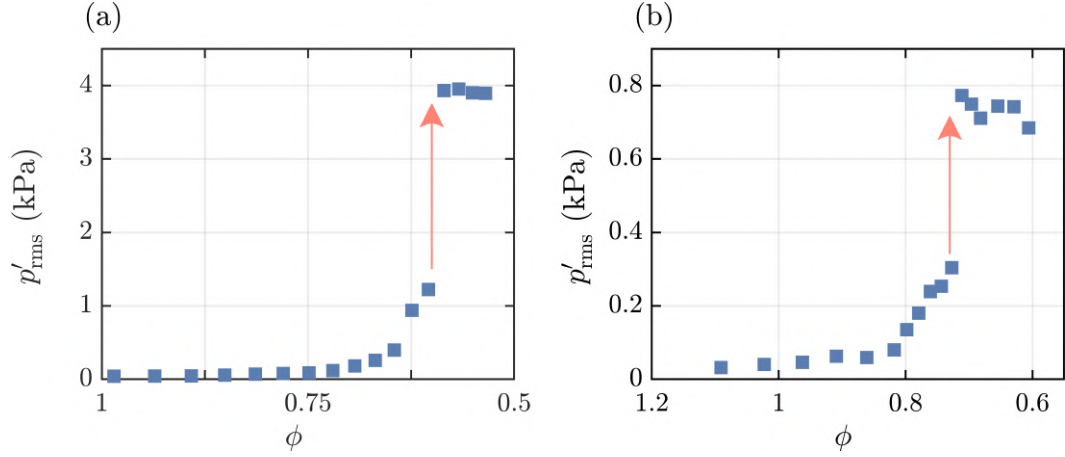


Figure 4.2: The variation of p'_{rms} as a function of ϕ during secondary bifurcation in (a) the swirl-stabilized backward facing step combustor and (b) the bluff-body stabilized backward facing step combustor with preheated air.

terms. The effect of turbulence is included as additive Gaussian white noise ξ , which is delta correlated in time: $\langle \xi(t)\xi(t + \tau) \rangle = \Gamma\delta(\tau)$, where Γ is the noise intensity. The symbol $\langle . \rangle$ represents the ensemble of realizations of the stochastic process. Thus, the overall dynamics is governed by the second-order stochastic differential equation. The model is extended to obtain primary and secondary limit cycle solutions, derive the underlying potential functions, and underscore the role of stochastic fluctuations on the observed phenomenology.

4.2 SLOW FLOW REPRESENTATION OF THE STOCHASTIC SYSTEM

Let us now consider the effect of stochastic fluctuations on the transition to limit cycle oscillations. One can consider the acoustic variable $\eta(t)$ to be quasi-harmonic (Minorsky, 1962), such that we have:

$$\eta(t) = A(t) \cos [\omega t + \Omega(t)]. \quad (4.2)$$

This decomposition allows us to separate the evolution of envelope-amplitude $A(t)$ and phase $\Omega(t)$, which vary at a slower time scale in comparison to the faster time scale $2\pi/\omega$. Using the method of averaging and simplifying the stochastic functions following

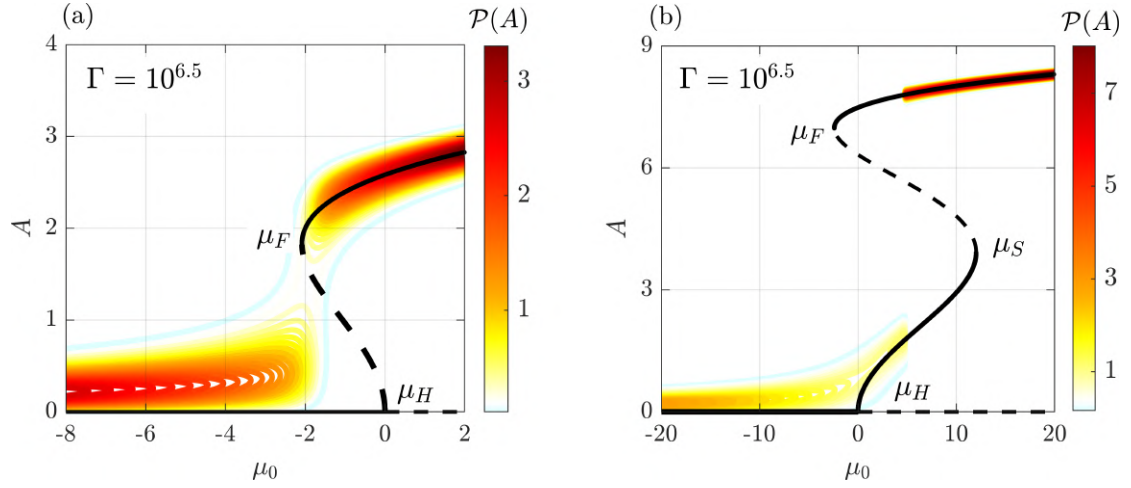


Figure 4.3: Bifurcation characteristics of the stochastic thermoacoustic system. Variation in the amplitude of fluctuations for (a) subcritical and (b) supercritical bifurcation followed by a secondary bifurcation to a large amplitude limit cycle. The bifurcation diagram for the deterministic system ($\Gamma = 0$, cf. Eq. 4.3) is indicated by the black line. The difference in the abscissa in (a) and (b) indicates the significant difference between the amplitude of limit cycles due to subcritical and secondary bifurcation. The solid lines correspond to the stable solution, while the broken lines indicate an unstable solution. The contour shows the variation in probability density function $\mathcal{P}(A)$ with parameter μ_0 , estimated according to Eq. ((4.11)). The noise intensity is fixed at $\Gamma = 10^{6.5}$. The other model parameters are: (a) $\mu_2 = -10$, $\mu_4 = 3$, $\mu_6 = 0$; and (b) $\mu_2 = 7$, $\mu_4 = -0.6$, $\mu_6 = 0.01$. Labels μ_H , μ_F , and μ_S indicate the parameter value μ_0 at which Hopf, fold, and secondary bifurcations occur.

(Krylov and Bogoliubov, 2016; Stratonovich, 1967; Balanov *et al.*, 2009) for further details), one obtains a set of Langevin equation governing the evolution of the slowly varying amplitude and phase of the system, which are expressed as:

$$\dot{A} = \frac{\mu_0}{2}A - \frac{\mu_2}{8}A^3 - \frac{\mu_4}{16}A^5 - \frac{5\mu_6}{128}A^7 + \frac{\Gamma}{4\omega^2 A} + \frac{\sqrt{\Gamma}}{\sqrt{2\omega}}\xi_1, \quad (4.3)$$

$$\dot{\Omega} = \frac{\sqrt{\Gamma}}{\sqrt{2\omega A}}\xi_2. \quad (4.4)$$

Here, ξ_1 and ξ_2 are two uncorrelated Gaussian white noise terms with zero mean and unit variance. Note that for a deterministic system, the evolution of the phase is zero ($\dot{\Omega} = 0$), and now with the addition of noise, the phase drifts. In Eq. (4.3), the sign associated with the factor $\mu_0/2$ determines the linear stability of the system. Further, the term $\Gamma/4\omega^2 A + (\sqrt{\Gamma}/\sqrt{2\omega})\xi_1$ arises due to the covariance of stochastic terms in the Fokker-Planck equation of the joint PDF of A and Ω . The Langevin equation (Eq. 4.3) can be expressed in terms of the potential function V , as shown below:

$$\dot{A} = -\frac{dV}{dA} + \frac{\sqrt{\Gamma}}{\sqrt{2\omega}}\xi_1. \quad (4.5)$$

Here, the negative sign associated with it implies the fact that the evolution of the system tends to minimize the potential function. The potential function $V(A, \mu_0)$ can then be determined by comparing Eqs. (4.3 & 4.5) and evaluating the resulting integral. This leads to

$$V(A) = -\frac{\mu_0}{4}A^2 + \frac{\mu_2}{32}A^4 + \frac{\mu_4}{96}A^6 + \frac{5\mu_6}{1024}A^8 - \frac{\Gamma}{4\omega^2} \ln A, \quad (4.6)$$

which defines the potential function of the overall system.

4.3 STATIONARY SOLUTION OF THE FOKKER-PLANCK EQUATION

The stochastic differential equation can be re-cast in the $\hat{\text{Ito}}$ sense (A. Pavliotis, 2014), which would allow us to invoke the Fokker-Planck equation for the evolution of $\mathcal{P}(A)$ corresponding to the Langevin equation of A . Thus, in the $\hat{\text{Ito}}$ sense, Eq. (4.5) can be

written as,

$$dA = \Psi(A)dt + dW, \quad (4.7)$$

where, $\Psi(A)$ is a function defined as,

$$\Psi(A) = -\frac{dV}{dA} = \frac{\mu_0}{2}A - \frac{\mu_2}{8}A^3 - \frac{\mu_4}{16}A^5 - \frac{5\mu_6}{128}A^7 + \frac{\Gamma}{4\omega^2A}, \quad (4.8)$$

and $dW = \xi dt$ is the increment of the Wiener process. Recall that it was assumed that the noise ξ is delta-correlated, a condition that is seldom fulfilled in real systems. The noise usually possesses finite correlation time (t_{cor}). For the present purposes, if ξ is sufficiently fast such that t_{cor} is much lesser than the relaxation time of the system, the evolution of the PDF $\mathcal{P}(A)$ satisfies the Fokker-Planck equation

$$\frac{\partial}{\partial t}\mathcal{P}(A, t) = -\frac{\partial}{\partial A}[\Psi(A)\mathcal{P}(A, t)] + \frac{\Gamma}{4\omega^2}\frac{\partial^2}{\partial A^2}\mathcal{P}(A, t). \quad (4.9)$$

Here, $\Psi(A)$ and $\Gamma/4\omega^2$ are the drift and diffusion coefficients, respectively. At large times, one can assume that the distribution reaches a stationary state, such that: $\lim_{t \rightarrow \infty} \mathcal{P}(A, t) = \mathcal{P}(A)$. Thus, Eq. (4.9) reduces to

$$\frac{d}{dA}\mathcal{P}(A) - \frac{4\omega^2}{\Gamma}\Psi(A)\mathcal{P}(A) = 0. \quad (4.10)$$

This equation can be readily solved to yield

$$\mathcal{P}(A) = \mathcal{N} \exp\left(-\frac{4\omega^2}{\Gamma}V(A)\right). \quad (4.11)$$

where \mathcal{N} is a constant such that $\int_0^\infty \mathcal{P}(A) = 1$.

4.4 EFFECT OF NOISE LEVELS ON THE TRANSITION

The analytically derived probability distribution function $\mathcal{P}(\eta)$ is plotted as a function of μ_0 in Eq. (4.11) in Fig. 4.3. For obtaining the subcritical bifurcation, we set $\mu_6 = 0$, $\mu_4 = 3$ and $\mu_2 = 10$, while for the secondary bifurcation, we $\mu_6 = 0.01$, $\mu_4 = -0.6$ and $\mu_2 = 7$. The bifurcation for the purely deterministic case is obtained by setting the noise intensity $\Gamma = 0$ in Eq. (4.3) and plotting the resulting solution. Figure 4.3 compares the effect

of the same level of noise intensity $\Gamma = 10^{6.5}$ on the characteristic of bifurcation. One can notice that for the same noise intensity, an initially sub-critical Hopf bifurcation transforms into a continuous sigmoid-type transition, as depicted by the contour of $\mathcal{P}(A)$ in Fig. 4.3. On the other hand, secondary bifurcation remains abrupt with an important difference: the fixed point solution is coloured by noisy fluctuations, which hide the sharp demarcation in the dynamics at the location of supercritical transition $\mu_0 = \mu_H$. This is precisely what is observed in the bifurcation plots from experiments (cf. Figs. 4.1a and 4.2) where the amplitude rises through the state of intermittency before the state of the low-amplitude limit cycle is reached.

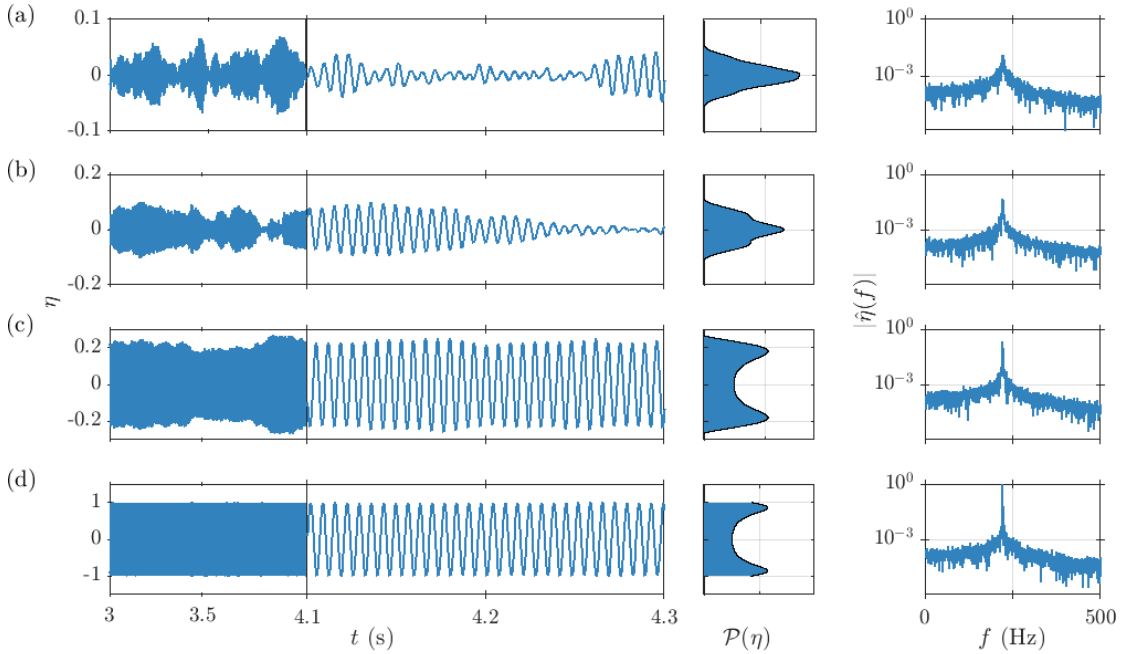


Figure 4.4: Simulated time series of $\eta(t)$, probability density function $\mathcal{P}(\eta)$ and the spectrum $\hat{\eta}(f)$ from the stochastic model during the state of (a) combustion noise ($\mu_0 = -20$), (b) intermittency ($\mu_0 = -5$), (c) low-amplitude thermoacoustic instability ($\mu_0 = 5$) and (d) high-amplitude thermoacoustic instability ($\mu_0 = 20$). The simulation parameters are: $\mu_6 = 0.01$, $\mu_4 = -0.6$, $\mu_2 = 7$ and $\Gamma = 10^{6.5}$.

To see this effect clearly, one can numerically simulate the model (Eq. 4.1) and plot the time series, $\mathcal{P}(\eta)$ and $\hat{\eta}(f)$ for four representative states across the transition in Fig. 4.4. At $\mu = -20$, the time series depicts aperiodic fluctuations with some periodic content (cf.

Fig. 4.4a). However, the spectral amplitude remains very low. The distribution $\mathcal{P}(\eta)$ shows unimodal characteristics, a fact also observed in the experimental data (cf. Fig. 4.1a). We also note here that deterministic features such as chaos and multifractality of the state of combustion noise are not captured by the additive white noise considered here. Next, at $\mu_0 = 2$ (cf. Fig. 4.4b), one can observe intermittent bursts amidst aperiodic fluctuations. The distribution $\mathcal{P}(\eta)$ shows a change from a unimodal distribution to peaks at $|\eta| \neq 0$, a feature that is noted in Fig. 4.1(c). Finally, we observe low-amplitude and high-amplitude limit cycle oscillations at $\mu_0 = 5$ and $\mu_0 = 20$ as seen in Fig. 4.4c,d.

To further quantify the effect of noise on the characteristics of an abrupt transition, we define the noise factor R as

$$R = \frac{p'_{\text{rms(CN)}}}{\Delta p'(\mu_c)} \times 100\%. \quad (4.12)$$

The noise factor R is the ratio of the amplitude of p'_{rms} during the state of combustion noise and amplitude difference in the fluctuations at the critical transition point (μ_c). The critical parameter for the subcritical point is $\mu_c = \mu_H$ while for secondary bifurcation, it is $\mu_c = \mu_S$ (cf. Fig. 4.3). For instance, the amplitude difference at the secondary bifurcation is $\Delta p'(\mu_S) = p'_{\text{rms}}(\text{HA-LCO}) - p'_{\text{rms}}(\text{LA-LCO})$, where HA-LCO and LA-LCO indicate the high-amplitude and low-amplitude limit cycle oscillations at $\mu_c = \mu_S$. Thus, the noise factor R compares the effect of combustion noise on the observed transition.

The noise factor R during the abrupt transition in the annular, longitudinal and preheated combustor are 1.86%, 4.37% and 10%. Similarly, for the transitions shown in Fig. 4.3, the noise factor R is 20% for the initially subcritical bifurcation and 8% for the secondary bifurcation. Thus, R values of the experimental results indicate that the noise levels of the combustor are not comparable to the amplitude of secondary limit cycle oscillation to transform the abrupt secondary transition into a continuous sigmoid-type transition. We also plot the stochastic bifurcation diagram by setting the noise intensity in the model to $\Gamma = 10^{7.5}$ in Fig. 4.5b. For this case, it is noted that the secondary bifurcation

displays a continuous, sigmoid-type transition. The noise factor for the case of $\Gamma = 10^{7.5}$ corresponds to $R = 35\%$. Thus, we find that the abrupt secondary bifurcations can be made continuous at very high noise levels, something which may not be feasible in real-world turbulent combustors.

4.4.1 Potential landscape of the secondary bifurcation

Let us now consider the stability of the dynamical states observed during the secondary bifurcation. The stability of various dynamical states is best visualized through the potential function V (Eq. 4.6). From the definition of the potential function, we have $\Psi(A) = -dV/dA$. Note that the minima and the maxima of the potential function $V(A, \mu_0)$ correspond to the stable and unstable fixed points of $\Psi(A, \mu_0)$. The value of $\Psi'(A)$ is a measure of the stability of the fixed points as $\Psi'(A)$ corresponds to the second derivative of the potential function (d^2V/dA^2) (Strogatz, 2018). The second derivative is a measure of the curvature of the potential function, describing its sharpness. Thus, the higher the magnitude of $-\Psi'(A)$ is, the higher would be the stability of the fixed point (Strogatz, 2018). We discuss how the variation in the parameter μ_0 leads to a change in the stability of the potential $\Psi(A)$ next.

The variation in the potential function $V(A)$ is shown in Fig. 4.5(c,d) at $\mu_0 = -5$, 4 and 12 to compare their behaviour at different states, indicated by the dotted lines in the transition diagram. The potential functions are shown at two different noise intensities ($\Gamma = 10^{6.5}$ and $\Gamma = 10^{7.5}$). The associated distribution $\mathcal{P}(A)$ is also shown below the potential $V(A)$. When $\mu_0 = -5$, the system is at stable equilibrium (Fig. 4.5c), and any amount of perturbation to the stable state will be restored to its equilibrium position. Thus, the system exhibits globally stable fixed points for $\mu_0 < 0$. The additive noise continuously perturbs the system around the stable fixed points. For low noise levels ($\Gamma = 10^{6.5}$), the mean of the distribution $\mathcal{P}(A)$ is at the minimum of the potential function $V(A)$ (cf. Fig. 4.5c, at $\mu_0 = -5$). In contrast, at a higher noise level ($\Gamma = 10^{7.5}$), $\mathcal{P}(A)$ shows a wider distribution, as the variance of the noise is much larger (see Fig. 4.5d, at

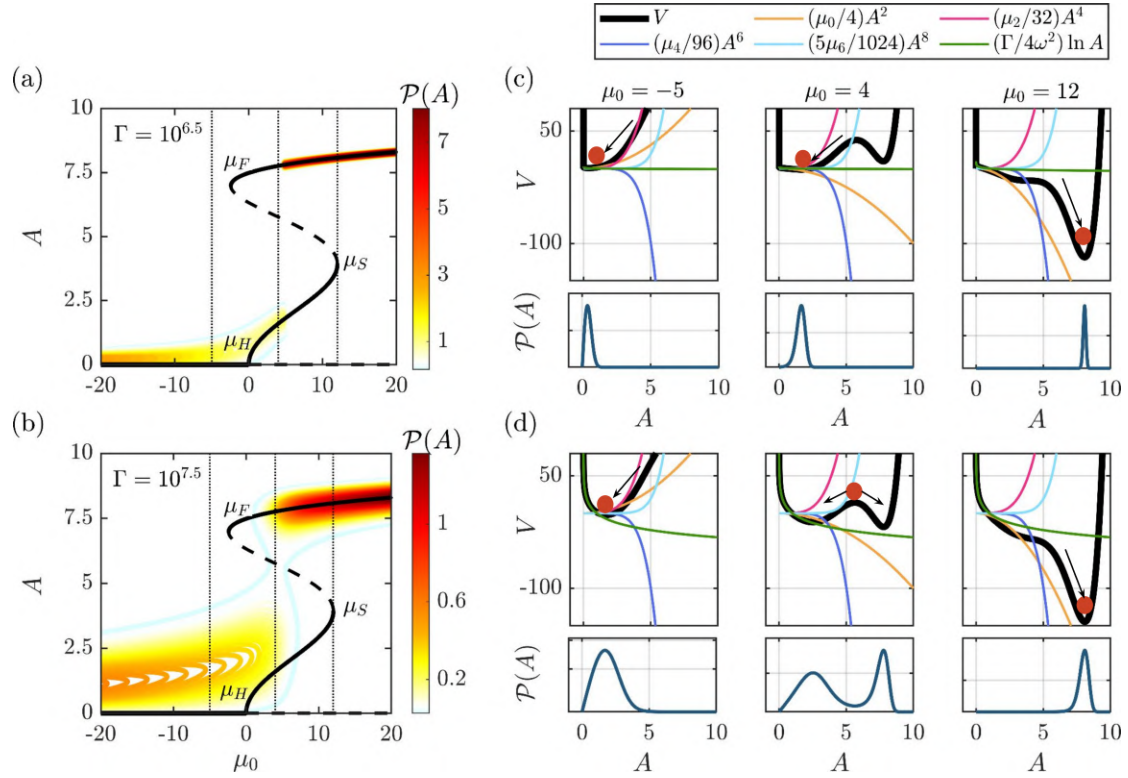


Figure 4.5: Effect of stochastic fluctuations on the properties of secondary bifurcation for (a) $\Gamma = 10^{6.5}$ and (b) $\Gamma = 10^{7.5}$. The contours show the variation in the distribution $\mathcal{P}(A)$ as a function of μ_0 . Panels (c) and (d) depict the potential functions $V(A)$ (top panel) and distribution $\mathcal{P}(A)$ (bottom panel). The bold line indicates the potential V . The contributions of individual terms of Eq. (4.6) are also indicated. $V(A)$ and $\mathcal{P}(A)$ are shown at $\mu_0 = -5, 4$ and 12 , marked by the dotted lines in panels (a) and (b). Other simulation parameters are the same as that in Fig. 4.3(b).

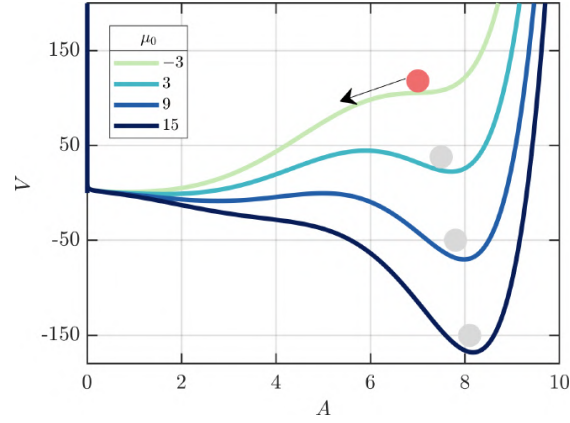


Figure 4.6: Illustration of hysteresis observed during the secondary bifurcation. Plot shows the variation of the potential function $V(A)$ when the value of the parameter is decreased from $\mu_0 = 15$ to $\mu_0 = -3$.

$\mu_0 = -5$).

For $\mu_0 > 0$, we notice that the potential $V(A)$ develops a secondary trough. We observe a unimodal Gaussian distribution $\mathcal{P}(A)$ for $\Gamma = 10^{6.5}$ at $\mu_0 = 4$ and $\mu_0 = 12$ (Fig. 4.5c). We notice that there is a shift in $\mathcal{P}(A)$ from a distribution centred at a lower amplitude to one centred at a much higher amplitude. This shift at $\mu_0 = 12$ is associated with the secondary trough in the potential $V(A)$ becoming the global minima, implying its global stability. On the other hand, for $\Gamma = 10^{7.5}$, we notice that at $\mu_0 = 4$, the potential $V(A)$ has a double-well characteristic with a comparable value of minima. As the noise level is higher, the perturbations can take the system from one potential well to the next. Consequently, the distribution $\mathcal{P}(A)$ has a bimodal distribution. The bimodal distribution implies the presence of intermittency, where the amplitude switches between low-amplitude oscillations (wider distribution) and higher-amplitude bursts of periodic oscillations (narrow distribution). Finally, at $\mu_0 = 12$, we have a unimodal distribution. The second trough has a lower minima, implying that the system reaches the globally stable limit cycle oscillation at very large amplitude levels.

To illustrate the phenomenon of hysteresis, we plot the potential functions for different values of μ_0 (15, 9, 3, and -3), which is shown in Fig. 4.6. The system depicts the state of

the secondary limit cycle at $\mu_0 = 15$. Reversing μ_0 below μ_S will not restore the state of the system back to the primary limit cycle. Upon reducing the parameter value ($\mu_0 = 9$ and 3), another trough forms at a lower amplitude value. However, the potential barrier (local maxima in V) of the unstable fixed point separating the two troughs is very high, thereby hindering the transitions back to either the primary limit cycle or the fixed point. The system transitions to the fixed point solution only when the parameter is reversed below the fold point (i.e., $\mu_0 < \mu_F$).

4.5 CONCLUDING REMARKS

To summarize, we reported the observation of secondary bifurcation in three disparate turbulent combustors – annular combustor, swirl-stabilized combustor, and bluff-body stabilized combustor with preheated air – despite them having completely different flame responses and acoustic characteristics. These systems exhibit a sequence of transitions from combustion noise to intermittency to low-amplitude limit cycle oscillations, followed by an abrupt jump to large-amplitude secondary limit cycle oscillations.

We also note that the intermittency obtained here in the model is due to the effect of noise-induced fluctuations. According to the studies, we come across broadly three kinds of mechanisms for the state of intermittency or the dynamics of epochs of periodic oscillations amidst the epochs of aperiodic oscillations. They are: intermittency as a dynamical state (Kabiraj and Sujith, 2012; Nair *et al.*, 2014), intermittency due to repeated switching between co-existing states possibly due to noise (triggering mechanism, Kabiraj *et al.* (2020)), and intermittent oscillations induced by noise (noise-induced coherence, Saurabh *et al.* (2017)). The intermittency obtained in the model of the current study corresponds to dynamics obtained by triggering and noise-induced oscillations. Further in the model, we have considered eigenmodes $j=1$, ignoring the mean flow and temperature gradients. Therefore, the current model is insufficient to capture the precise dynamics of chaos and intermittency; the influence of the higher modes is additionally required

to describe the complex dynamics. One can consider the approach of fractional order differential equation to capture the intricate dynamics such as chaos Varghese *et al.* (2021). Alternatively, one can also utilize the concept of the kicked oscillator model to model the dynamics of intermittency Nair and Sujith (2015).

However, the current approach is sufficient to show that a deterministic subcritical bifurcation is transformed into a continuous sigmoid-type transition, typical of the intermittency route, in the presence of noise. By means of comparison, we observe that for a given intensity of noise, which is high enough to transform a subcritical Hopf bifurcation into a continuous one, the secondary bifurcation to a large amplitude limit cycle remains abrupt.

CHAPTER 5

CONTINUOUS RAPID TRANSITIONS IN TURBULENT THERMOACOUSTIC SYSTEMS

In the previous chapter, we showed that turbulent combustors exhibit abrupt transitions. These abrupt transitions are also referred to as explosive transitions and are characterized by the phenomenon of hysteresis (Kumar *et al.*, 2015). The occurrence of hysteresis is due to the simultaneous presence of multiple stable regimes for a range of control parameters (Zou *et al.*, 2014). However, in practical engineering systems, there are exceptions where a genuine abrupt rise in the statistical measure of the oscillations is observed, but the transition is not discontinuous (Brøns and Bar-Eli, 1991). Such transitions, where a rapid rise in the magnitude of the fluctuation occurs for a minute increment in the control parameter, were primarily investigated in the Van der Pol oscillator model and are referred to as canard explosions (Krupa and Szmolyan, 2001). Canard explosions have been reported in many real-world systems such as chemical oscillations (Brøns and Bar-Eli, 1991), ground dynamics of an aircraft (Rankin *et al.*, 2011), neuronal activity (Moehlis, 2006), predator-prey food chains (Deng, 2004), and light emitting diodes (Marino *et al.*, 2011).

In a transition involving a canard explosion, the magnitude of the limit cycle grows significantly soon after the Hopf bifurcation (Börger, 2017). The dynamics of the system during this transition become highly sensitive to variation in the control parameter. There is a significant growth in the magnitude of the oscillation for an exponentially small range of values of the control parameter at the canard explosion regime (Brøns and Bar-Eli, 1991). Hence, a canard explosion appears abrupt if there is a lack of resolution in the

The results presented in this chapter are published in Bhavi, R. S., S. Sudarsanan, M. Raghunathan, A. Bhaskaran, and Sujith, R. I. (2024), Canard explosions in turbulent thermo-fluid systems, *Chaos: An Interdisciplinary Journal of Nonlinear Science*, 34, 103133. <https://doi.org/10.1063/5.0223320>

variation in system parameters (Diener, 1984). A continuous transition comprising a canard explosion, albeit appears abrupt, traces the same forward and reverse path in the control parameter variation (Börger, 2017). Further, large magnitude bursts and mixed-mode oscillations are observed when the system exhibits slow-fast dynamics at the canard explosion regime (Han and Bi, 2012; Desroches *et al.*, 2013). In this chapter, the current study reports the observation of canard explosions in thermo-fluid systems. We present the experimental results for the rapid rise in the magnitude of the acoustic pressure oscillations within a minute range of the control parameter, a principal feature of the canard explosion.

5.1 CANARD EXPLOSIONS IN TURBULENT COMBUSTORS

Figure 5.1 represents the bifurcation diagram and the nature of the sudden transition in the bluff body stabilized dump combustor. In order to study the sudden transitions via canard explosions, the control parameter (ϕ) of the system is varied. Initially, when the airflow rate is varied in steps of 30 SLPM, we observed an abrupt transition (refer to points d and e in Fig. 5.1a). The abrupt transition is from low magnitude ($p'_{\text{rms}} = 420$ Pa) to high magnitude ($p'_{\text{rms}} = 3525$ Pa) acoustic pressure fluctuations. Here, p'_{rms} represents the root mean square value of the acoustic pressure fluctuations (p'). The corresponding time series are presented in Fig. 5.1(d, e). To further investigate this seemingly abrupt transition, the airflow rate is varied at finer steps (10 SLPM) between the points of the control parameter corresponding to the abrupt jump. A continuous, albeit steep, variation in the rms value of p' is observed when the control parameter is varied in finer steps (refer to Fig. 5.1b). We have also performed experiments, varying at finer steps of ϕ 0.006 (airflow of 5 SLPM), to confirm continuous rapid rise (please refer to Appendix A.2). Further, it is noted that the continuous transition occurs via a state of bursting (refer to Fig. 5.1f-i). During the bursting state, one can observe large amplitude fluctuations ($p' \approx 3500$ Pa) amidst low amplitude fluctuations ($p' \approx 500$ Pa) (refer to Fig. 5.1g).

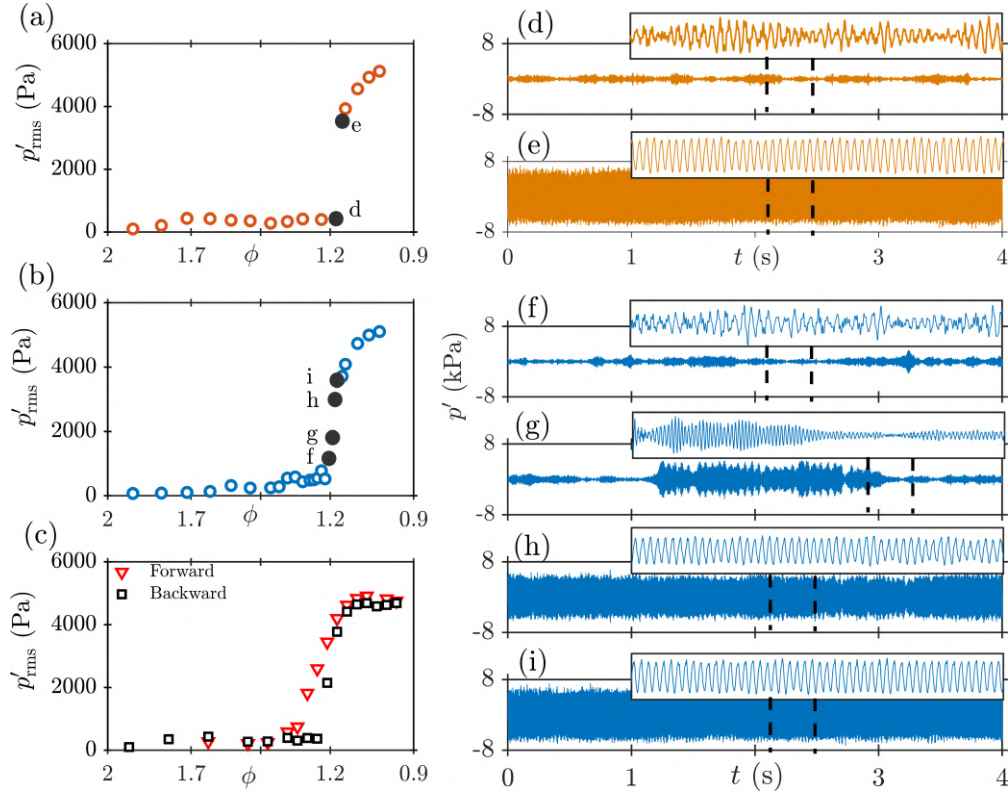


Figure 5.1: Representation of a sudden transition to high amplitude periodic oscillations via canard explosion in the bluff body stabilized dump combustor. **(a, b & c)** The bifurcation diagrams for the variation of the rms value of the acoustic pressure fluctuations (p'_{rms}) as a function of the equivalence ratio ϕ . **(d-i)** The corresponding time series of the acoustic pressure signal during canard explosion. **(a)** Sudden transition from a low amplitude **(d)** ($p'_{\text{rms}} = 420$ Pa) to very high amplitude **(e)** ($p'_{\text{rms}} = 3525$ Pa) acoustic pressure fluctuations as ϕ is varied. When ϕ is varied in finer steps between these apparently abrupt transition points, we observe a **(b)** continuous transition **(f-i)** to high amplitude fluctuations via **(g)** bursting dynamics. **(c)** The transition retraces the forward path when ϕ is varied in the reverse direction, implying the absence of the hysteresis. Thus, a transition with a rapid increase in the magnitude of acoustic pressure fluctuations is observed within a very narrow range of the control parameter.

Further, when the control parameter is varied in the reverse direction, the transition retraces the forward path (refer to Fig. 5.1c). Similar observations of the canard explosions were observed when experiments were performed in a swirl-stabilized dump combustor (Fig 5.2). In the swirl-stabilized dump combustor, as the equivalence ratio is decreased from 0.783 to 0.532, a rapid decrease in the value of p'_{rms} is observed (refer to the points a1, a2, & a3 of Fig. 5.2a). The transition is from a state of high magnitude fluctuations ($p'_{\text{rms}} = 4730$ Pa) to a state of low magnitude fluctuations ($p'_{\text{rms}} = 770$ Pa) (refer to Fig. 5.2a1, a3). Additionally, it is noted that when the parameter is varied in the reverse direction, the system retraces the forward path (Fig. 5.2a). The difference in the values of p'_{rms} at the state of thermoacoustic instability in forward and reverse paths is due to increased damping as a result of prolonged heating of the combustor walls (Pavithran *et al.*, 2023). Thus, we note that a continuous but steep transition involving a canard explosion exhibits no hysteresis.

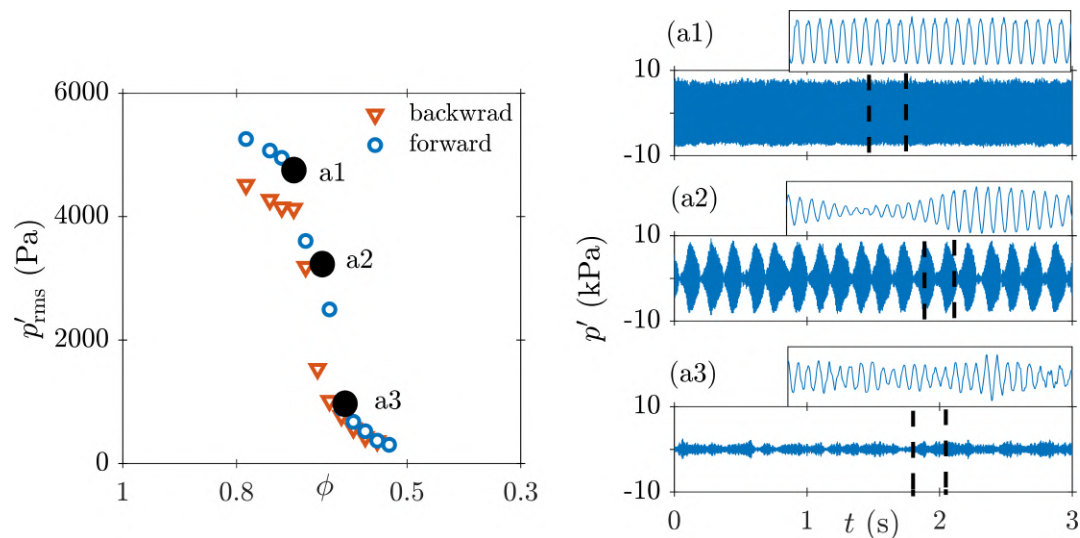


Figure 5.2: Representation of the sudden transition via canard explosion in a swirl stabilized dump combustor. **(a)** The forward and reverse path of the transition via the canard explosion. The equivalence ratio (ϕ) in the forward path is varied from 0.783 to 0.532. It is noticed that the transition occurs via the state of large amplitude bursting **(a1-a3)**.

Further, in the swirl stabilized dump combustor, the steep rise in the rms value of p' to a high amplitude oscillatory instability occurs via the state of large amplitude bursting

(refer to point a2 in Fig. 5.2a and the corresponding time series in Fig. 5.2a2). The state of bursting has imprints corresponding to the states of low-amplitude fluctuations and high-amplitude fluctuations (Fig. 5.2a3 & a1). Similarly, when ϕ is varied from 1.4 to 0.9 in an annular combustor, a sudden transition for $\phi > 1.075$ is observed (refer to Fig. 5.3a). Upon varying ϕ in the reverse direction, the transition retraces its path. Moreover, it is noted that the transition occurs via a state of large amplitude bursting (refer to Fig. 5.3b2). The bursting state has the imprints of low-amplitude fluctuations and high-amplitude fluctuations (cf. Fig. 5.3b1, b2 & b3), similar to the bursting characteristics observed in the swirl stabilized dump combustor. However, the time interval of bursting oscillations in the annular combustor is larger than the time interval of bursting in the swirl-stabilized combustor. In summary, in all three combustors, it is noted that the amplitude of the bursts corresponding to an underlying canard explosion is very high due to the rapid nature of the transition at the bifurcation regime.

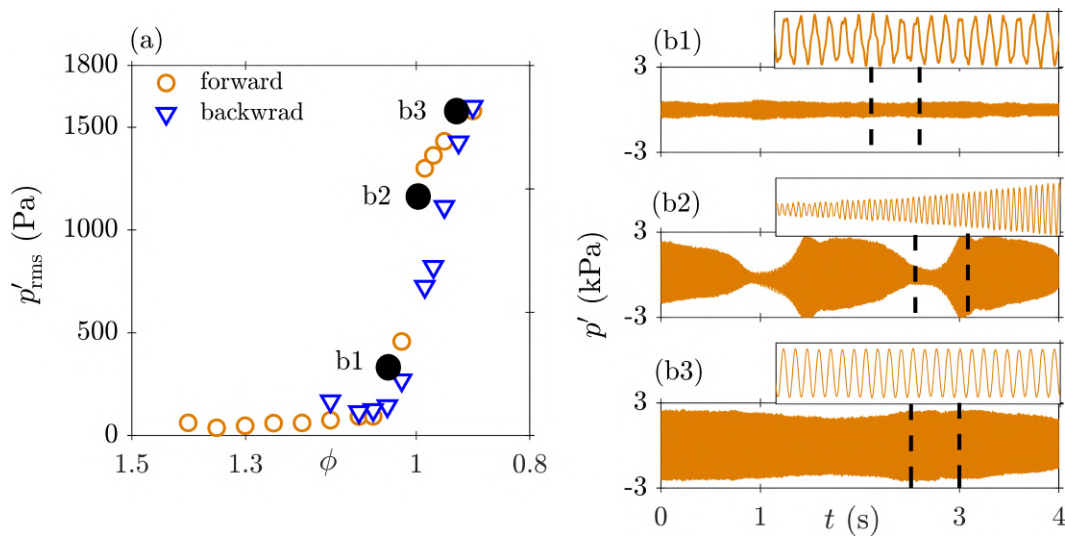


Figure 5.3: Representation of the sudden transition via canard explosion in an annular combustor. **(a)** The forward and reverse path of the transition via the canard explosion. The equivalence ratio (ϕ) in the forward path is varied from 1.4 to 0.9. We notice that the transition occurs via the state of large amplitude bursting **(b1-b3)**.

In order to investigate the bursting phenomenon, an experimental measurement of temperature fluctuations of the hot exhaust gases for the swirl-stabilized dump combustor

during the state of bursting ($\phi = 0.657$). The temperature fluctuations are measured using a K-type thermocouple. The exhaust gas temperature is governed by the internal variables of the combustor, such as flame temperature, equivalence ratio and the heat transfer rate to the combustor walls. These variables, in turn, govern the dynamics of the oscillatory instabilities exhibited by a combustor.

Figure 5.4 represents the variation in temperature alongside the acoustic pressure fluctuation p' during bursting in a swirl stabilized dump combustor. We note that there is a strong correlation between the temperature fluctuation (T') and the envelope of the bursting oscillations (p'_{env}). The strength of the correlation is tested by computing Pearson's correlation coefficient (r), and the value of r is 0.84 for T' and p'_{env} . The time series of T' is band passed to remove the fluctuations lesser than 1 Hz for computing the value of r . Moreover, the local maxima of T' are in the high amplitude bursting regime of p' , and the local minima of T' are in the low amplitude regime of p' (Fig. 5.4a). This rhythmic variation of T' and p'_{env} is also evident in the amplitude spectrum of the envelope of acoustic pressure fluctuations (\hat{p}'_{env}) and the temperature fluctuations (\hat{T}'_{env}) having the same dominant frequency at 6 Hz (refer to Fig. 5.4b, c). A similar observation of variation in T' and the envelope of p' , but out of phase pattern, is made for the state of large amplitude bursting in the annular combustor at $\phi = 1$ (refer to Fig. 5.4d).

Further, the past literature on bursting dynamics suggests that bursting occurs when a system parameter fluctuates at a slower time scale (compared to the system oscillation) at the bifurcation regime (Izhikevich, 2000; Kasthuri *et al.*, 2019; Tandon *et al.*, 2020). Therefore, observing variation in temperature fluctuations in correlation with the bursting amplitude (Fig. 5.4), we note that a system parameter is fluctuating at a slower time scale at the bifurcation regime.

Thus, it is evident from Figs. 5.1, 5.2 and 5.3 that sudden transitions via canard explosions occur in three different turbulent thermoacoustic systems. Despite differences in the

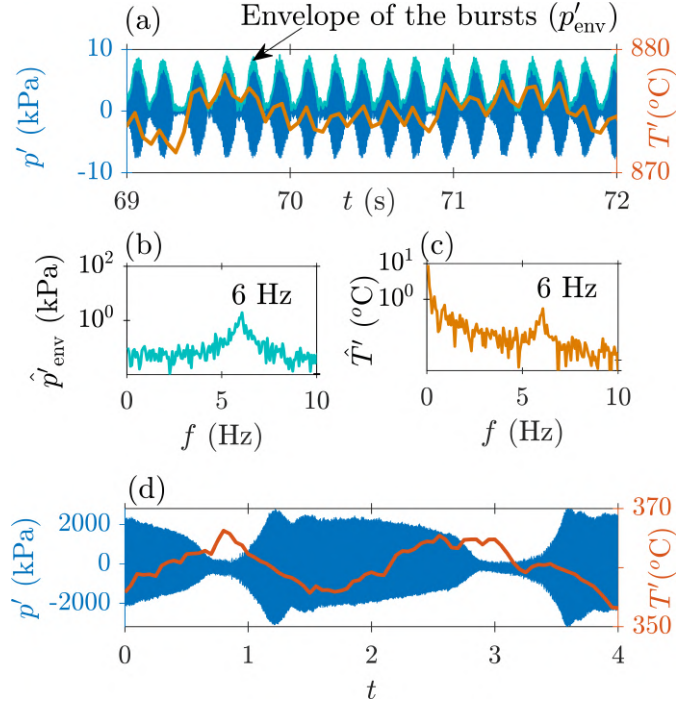


Figure 5.4: **(a)** Representation of the variation of the exhaust gas temperature (T') along with the acoustic pressure fluctuations (p') for a swirl stabilized dump combustor, measured during the state of bursting via canard explosions ($\phi = 0.657$). **(b-c)** The amplitude spectrum of the envelope of acoustic pressure fluctuations (\hat{p}'_{env}) and the temperature fluctuations (\hat{T}'_{env}) have the same dominant frequency at 6 Hz. **(d)** The variation of T' along with p' for an annular combustor, measured during the state of bursting via canard explosions ($\phi = 1$). Notice the pattern of variations in T' and the envelope of p' ; the maxima of T' is in the region of minimum p' , and the minima of T' is in the region of maximum p' .

nature of the flow fields and the flame acoustic interactions in these different turbulent combustor configurations, we observe a common transition via canard explosion. The observation of large amplitude bursts in the regime of bifurcation hints towards an underlying universal mechanism, which we illustrate in the following subsections using a low-order model for thermo-fluid systems. Inspired by the experimental observations, we consider a Van der Pol oscillator as illustrated by Ananthkrishnan *et al.* (1998) to describe the sudden transition. We reduce the influence of the lower-order nonlinearities such that the variation of the system amplitude becomes highly sensitive to the control parameter at the bifurcation regime. We further incorporate a slowly varying coupling

term to the acoustic driving to obtain the phenomenon of large amplitude bursting.

5.2 MODELLING CANARD EXPLOSION IN THERMOACOUSTIC SYSTEM

The dynamics of the canard explosion presented in the above experiments is mainly associated with the change in the amplitude of the acoustic pressure fluctuations as the parameter is varied. Therefore, one can consider the mathematical model discussed in Chapter 2, which is given as,

$$\ddot{\eta} + \left(\mu_6 \eta^6 + \mu_4 \eta^4 + \mu_2 \eta^2 - \mu_0 \right) \dot{\eta} + \omega^2 \eta + \xi = 0, \quad (5.1)$$

We note that the coefficients μ_2 , μ_4 and μ_6 govern the stability and the amplitude of the LCO branches in the bifurcation curve. Now, the dynamics of the canard explosion is such that the amplitude of the system becomes highly sensitive to a narrow range of parameters near the bifurcation regime. To achieve this, one can reduce the value of the coefficients coupled with the terms $(\mu_6 \eta^6 + \mu_4 \eta^4 + \mu_2 \eta^2)$. Therefore, we multiply all the nonlinear coefficients with a constant $\epsilon \ll 1$, reducing the strength of nonlinearity associated with the nonlinear terms. Such systems with reduced strength of nonlinearity are referred to as weakly nonlinear oscillators (Strogatz, 2018). The modified equation with the coupling term ϵ is written as,

$$\ddot{\eta} + \epsilon \left(\mu_6 \eta^6 + \mu_4 \eta^4 + \mu_2 \eta^2 \right) \dot{\eta} - \mu_0 \dot{\eta} + \omega^2 \eta = 0. \quad (5.2)$$

To visualise the effect of the magnitude of ϵ , the dynamics of the envelope of the fluctuations is obtained from the harmonic oscillator Eq. (5.2), using the method of averaging (Balanov *et al.*, 2009; Strogatz, 2018). We substitute the acoustic variable to be of the form $\eta(t) = A(t) \cos[\omega t + \Omega(t)]$. Here, $A(t)$ and $\Omega(t)$ represent the amplitude-envelope and its phase, respectively. The evolution time scale of $A(t)$ and $\Omega(t)$ is much slower than the faster times scale of system $2\pi/\omega$. Thus, after substituting

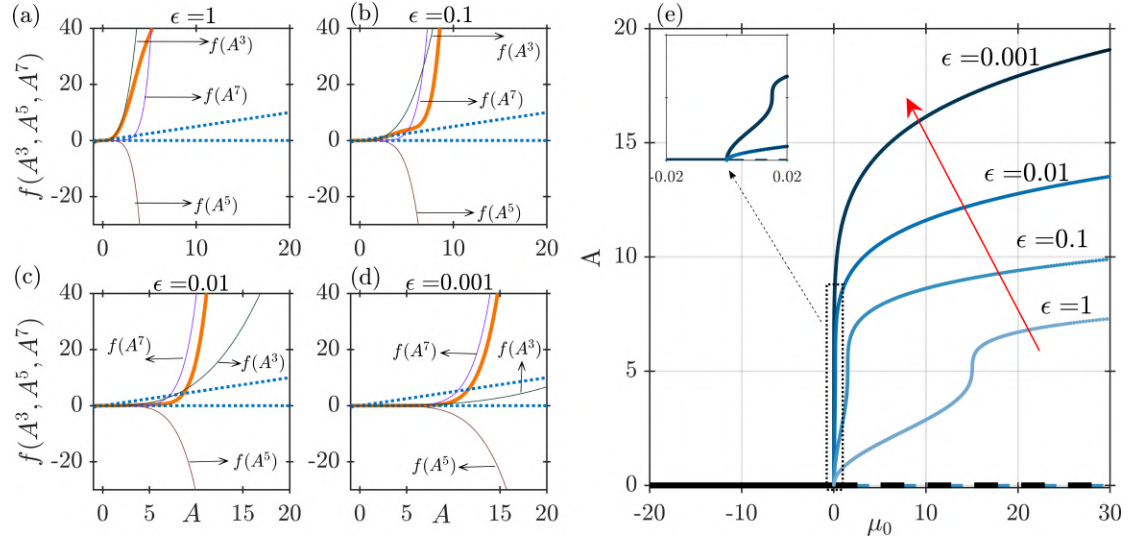


Figure 5.5: **(a-d)** Representation of the effects of ϵ on the evolution of the solutions for Eq. (5.3), which is of the form $\dot{A} = f(\mu_0, A) - f(A^3, A^5, A^7)$. The ordinate denotes the values of $f(A^3, A^5, A^7)$ (thick orange curve), and the abscissa represents the values of A . The contributions from A^3 , A^5 , and A^7 are presented in the coloured thin solid curves. The dashed blue lines represent the control parameter curve $f(\mu_0, A)$ for $\mu_0 = 0$ and 1. Geometrically, the solutions are the points of intersections of $f(A^3, A^5, A^7)$ and $f(\mu_0, A)$. **(e)** Bifurcation diagram to represent the effect of ϵ on the continuous bifurcation curve obtained by fixing $\mu_2 = 6.7$, $\mu_4 = -0.5$, and $\mu_6 = 0.01$. The variation of μ_0 is shown on the abscissa and the solutions of Eq. (5.3) are shown on the ordinate. In the bifurcation diagram, thick lines are for stable solutions and the broken line is for unstable solutions. Notice that as ϵ is decreased from 1 to 0.001, the range of parameters to reach the high amplitude oscillations after the bifurcation decreases to a very narrow span.

$\eta(A, \Omega)$ and averaging Eq. (5.2) over the faster time scale $2\pi/\omega$ (Balanov *et al.*, 2009), the dynamics of the amplitude-envelope of the oscillations is obtained as,

$$\dot{A} = \frac{\mu_0}{2}A - \epsilon \left(\frac{\mu_2}{8}A^3 + \frac{\mu_4}{165}A^5 + \frac{5\mu_6}{128}A^7 \right). \quad (5.3)$$

We note that the evolution of the amplitude-envelope is a function $\dot{A} = f(\mu_0, A) - f(A^3, A^5, A^7)$, which is dependent on the control parameter μ_0 and the damping term $f(A^3, A^5, A^7)$. The nonlinear damping term $f(A^3, A^5, A^7)$ is in turn a function of the higher order terms $f(A^3)$, $f(A^5)$ and $f(A^7)$. The solutions for Eq. (5.3) are computed as $\dot{A} = 0$, which are obtained by balancing $f(\mu_0, A) = f(A^3, A^5, A^7)$ (Strogatz, 2018).

We proceed with considering a case of continuous bifurcation obtained by setting $\mu_2 = 6.7$, $\mu_4 = -0.5$, and $\mu_6 = 0.01$. In Fig. 5.5(a-d), the effect of ϵ on the evolution of solutions for Eq. (5.3) is represented. These solutions are, geometrically, the points of intersections of the curves $f(\mu_0, A)$ and $f(A^3, A^5, A^7)$. The thick orange line represents the curves for $f(A^3, A^5, A^7)$, which is a summation of contributions from $f(A^3)$, $f(A^5)$ and $f(A^7)$ represented with thin lines. The curves for $f(\mu_0, A)$, at $\mu_0 = 0$ and $\mu_0 = 1$, are shown in dotted blue lines. $f(\mu_0, A)$ is a line passing through the origin where μ_0 is its slope. Thus, several curves for $f(\mu_0, A)$ with varying slopes are obtained as μ_0 is varied as a control parameter, not shown here in the interest of space. From Fig. 5.5(a,b), for the lower values of A , it is noted that the dynamics of the curve $f(A^3, A^5, A^7)$ (orange line) is mainly contributed from $f(A^3)$ and $f(A^5)$. One can also note that as the value of ϵ decreases from 1 to 0.001, the absolute value of the functions ($|f(A^3)|$, $|f(A^5)|$, and $|f(A^7)|$) decreases, and their curves tend towards the abscissa (cf. Fig. 5.5a-d). The effect of the decrease in ϵ , for smaller amplitudes of A , is more pronounced on the lower order nonlinear terms $f(A^3)$ and $f(A^5)$ than on the highest order term $f(A^7)$ (cf. Fig. 5.5a-d). This influence of ϵ on the nonlinear terms collectively transforms the curve $f(A^3, A^5, A^7)$ to have lower slopes for an extended value of A (compare the orange lines of Fig. 5.5a-d). Thus, the transformation results in a scenario where one observes a rapid change in the value of solutions, the intersection of $f(A^3, A^5, A^7)$ and $f(\mu_0, A)$ (cf. Fig. 5.5c,d), for a minute change in the value of the parameter μ_0 in the range $|\mu_0| < 1$.

In Fig. 5.5(e), we plot the bifurcation curves for the cases of $\epsilon = 1, 0.1, 0.01$, and 0.001 obtained by varying the control parameters in the range of $-20 \leq \mu_0 \leq 30$. As ϵ is reduced, it is noticed that the bifurcation curve significantly steepens at the Hopf point $\mu_0 = 0$ (refer to Fig. 5.5e). In other words, the range of values of μ_0 to reach the saturation in the rise in amplitude decreases to a very narrow span (refer to the inset of Fig. 5.5e). The steepening of the transition curve occurs due to the higher reduction in the nonlinearity of lower-order nonlinear terms for lower amplitudes A , which otherwise

form a continuous bifurcation (refer to the curve $\epsilon = 1$, in Fig. 5.5). From Fig. 5.5(a-d), we convey that the effect of ϵ is less on the highest-order nonlinear term η^6 when compared to the lower-order nonlinear terms in Eq. (5.2). Thus, the coupling term ϵ aids in obtaining a weakly nonlinear oscillator exhibiting a transition with a canard explosion at the Hopf point.

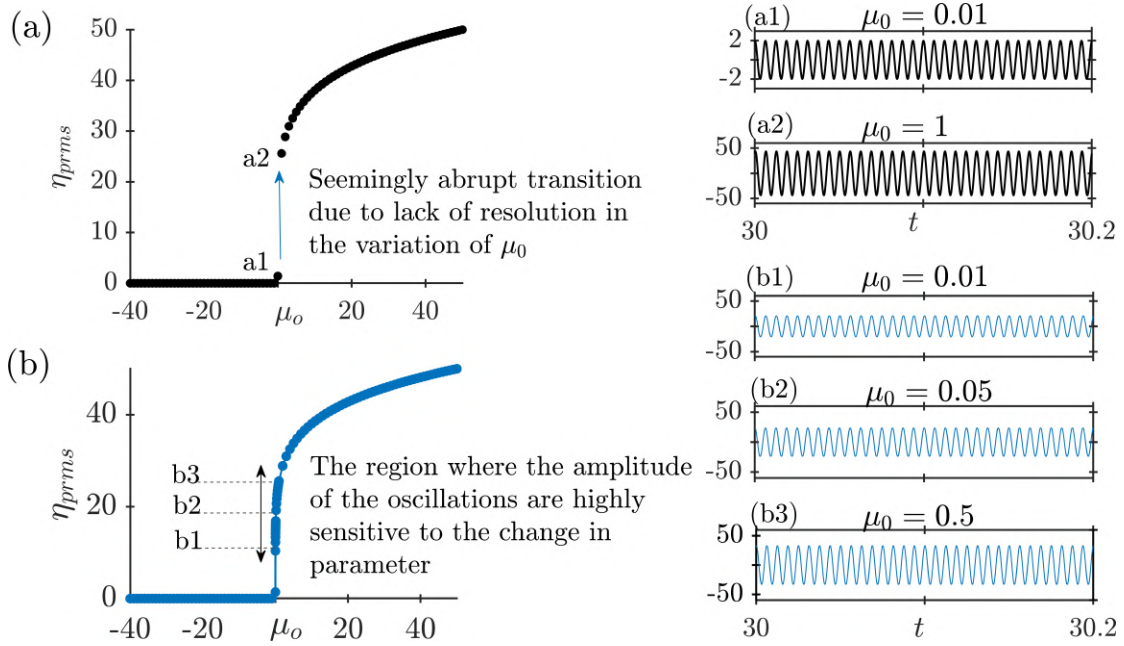


Figure 5.6: Representation of the canard explosion by numerically integrating Eq. (5.2). The curves represent the variation of η_{rms} as a function of μ_o . When the control parameter μ_o is varied in steps of 1, we notice an abrupt jump in (a) the bifurcation diagram. The abrupt nature of the transition is due to a lack of resolution in the variation of the control parameter. The abrupt jump is also evident from the amplitude of the time series (a1) before and (a2) after the transition. However, when we vary the control parameter in finer steps, we have (b) stable dynamics at each of these finer steps. Thus, the model captures a rapid continuous transition (b1-b3), where the amplitude rises significantly with a negligible change in μ_o .

Further, utilising 4th order Runge-Kutta method, we numerically integrate Eq. (5.2) by fixing $\epsilon = 0.0001$ for a range of control parameter $-40 \leq \mu_o \leq 50$ to obtain the bifurcation diagram. Figure 5.6a denotes the bifurcation curve when the control parameter μ_o is varied in steps of 1. Since there is a significantly steeper rise, the transition appears to be abrupt at the Hopf point $\mu_o = 0$ due to a weaker resolution in the variation of

the control parameter. This seemingly abrupt transition is what we notice during the experiments as the system transitions to high-amplitude thermoacoustic instability (refer to Fig. 5.1a). We further illustrate that, by increasing the resolution at the canard explosion regime, the system exhibits the stable LCO at every small variation in μ_0 , implying a continuous rapid transition (refer to Fig. 5.6b).

Further, the experimental data denotes that the temperature fluctuations of the hot gas vary in correlation with the bursting amplitude at a slower time scale (compared to system oscillations) (refer to Fig. 5.4). This variation of the temperature fluctuations suggests that there is an additional parameter that fluctuates at a timescale slower than the thermoacoustic oscillations during the state of bursting. When such an oscillating term is coupled with the driving term η , the system exhibits bursting oscillations at the bifurcation regime (Kasthuri *et al.*, 2019). We illustrate the bursting phenomenon for an underlying canard explosion in the following subsection.

5.2.1 Bursting behaviour due to underlying canard explosion

The amplitude of the bursts corresponding to an underlying canard explosion is very high due to the sudden nature of the transition at the bifurcation regime. Experimentally, we observed that a system parameter (T') fluctuates at a slower time scale (compared to system oscillations) at the bifurcation regime of the canard explosion (refer to Fig. 5.4). Such parametric oscillations are also reported in past studies of thermoacoustic systems (Kasthuri *et al.*, 2019; Tandon *et al.*, 2020). Kasthuri *et al.* (2019) has shown that the temperature near the flame holder oscillates at a much slower time scale than the thermoacoustic oscillations during the state of bursting. In a turbulent combustor with a swirler configuration, Hong *et al.* (2008) showed that there is a fluctuation in the equivalence ratio during the state of large amplitude bursting. Tandon *et al.* (2020) replicated the bursting dynamics of the low-turbulence systems using a phenomenological model containing slow-fast time scales. In line with the conjectures of these studies, one would intuitively expect large amplitude bursting oscillations in a system containing

slow-fast time scales across the canard explosions. Inspired by these studies, we further illustrate the effect of the fluctuation of the system parameter at the bifurcation regime of a canard explosion; for that, we couple the driving term $\dot{\eta}$ with a periodic oscillation of a very low frequency ω_q with a coupling strength of q . Thus, Eq. (5.2) is further modified as,

$$\begin{aligned} \ddot{\eta} + \epsilon \left(\mu_6 \eta^6 + \mu_4 \eta^4 + \mu_2 \eta^2 \right) \dot{\eta} - \mu_0 \dot{\eta} \\ - [q \sin(\omega_q t) + \xi_m] \dot{\eta} + \omega^2 \eta + \xi_a = 0. \end{aligned} \quad (5.4)$$

The coupling is added with the multiplicative noise ξ_m to model the fluctuations associated with the driving as a result of the internal noise in the system (Clavin *et al.*, 1994). We also add additive white noise ξ_a to the Eq. (5.4) to incorporate the effect of turbulence (Noiray, 2017). Here, ξ is the white noise defined as $\langle \xi \xi_\tau \rangle = \Gamma \delta \tau$, where Γ is the noise intensity. The subscripts ‘ m ’ and ‘ a ’ denote the correspondence to multiplicative and additive noise, respectively. We further note an alternate description for the coupling added here can also be viewed as an oscillating parameter with the noise, which can be written as $(q \sin(\omega t) + \xi_m) \dot{\eta}$.

The qualitative nature of the bursting behaviour obtained from the model for different types of combustors is represented in Fig. 5.7. At $\mu_0 = 0$, fixing $q = 0$, $\Gamma_a = 10^5$ and $\Gamma_m = 10^4$, we obtain the bursting behaviour that matches with the time series obtained from the bluff body stabilized dump combustor (refer to Fig. 5.7a). The irregularity in the bursting pattern is due to the multiplicative noise ξ_m associated with the driving term $\dot{\eta}$. When we fix $\omega = 370$ rad/s, $\omega_q = 3$ rad/s, $q = 20$ rad/s, $\Gamma_a = 10^5$ and $\Gamma_m = 10^4$, we obtain a bursting pattern observed in the swirl stabilized dump combustor (refer to Fig. 5.7b).

Further, upon fixing $\omega = 370$ rad/s, $\omega_q = 0.5$ rad/s, $q = 20$ rad/s, $\Gamma_a = 10^7$ and $\Gamma_m = 10^5$, we obtain a bursting pattern observed in the annular combustor (refer to Fig. 5.7b). The coupling oscillation frequency ω_q for the case of an annular combustor is lesser than that of the swirler stabilized dump combustor. Hence, the bursts in the annular combustor

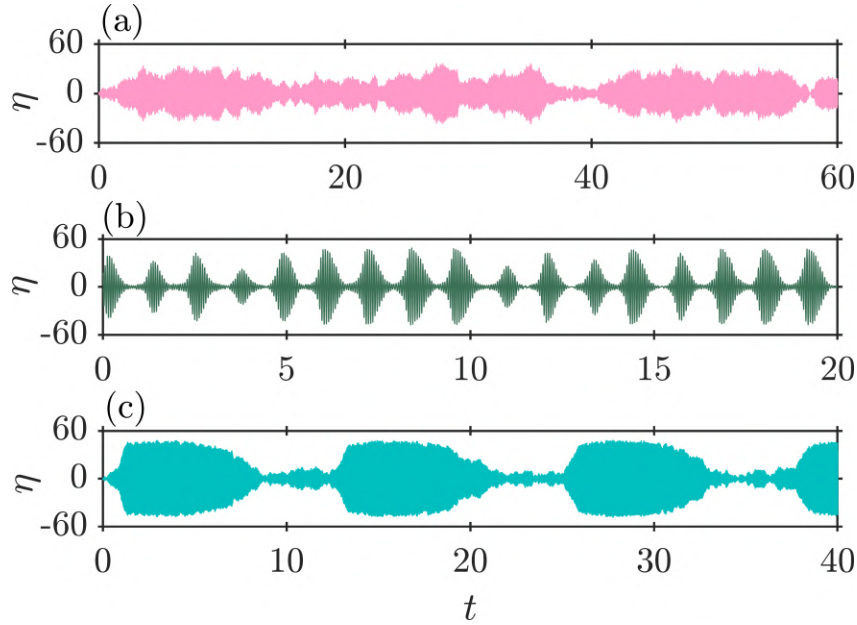


Figure 5.7: Representation of the time series for bursting behaviour at the bifurcation regime of the canard explosion, obtained by numerical integration of Eq. (5.4). **(a)** Time series analogous to the bursting behaviour of a bluff body stabilized dump combustor. **(b)** Time series analogous to the bursting behaviour of a swirl stabilized dump combustor. **(c)** Time series analogous to the bursting behaviour of an annular combustor. We notice large amplitude bursts at the bifurcation regime due to the underlying canard explosion

are of longer duration. Thus, using these results from the model we illustrate that large amplitude bursts are observed in turbulent combustors when a system parameter fluctuates at the bifurcation regime of an underlying canard explosion.

5.3 CONCLUDING REMARKS

In summary, we reported the experimental evidence for the occurrence of canard explosion in three different turbulent thermoacoustic systems—a bluff body and a swirl-stabilized dump combustor, and a swirl-stabilized annular combustor. The transition appears discontinuous when there is a lack of resolution in the variation of the control parameter. Though the rise in the magnitude of the fluctuations is steep in nature, unlike abrupt transitions, the canard explosion in this study exhibits no hysteresis. When such a transition involves a parameter fluctuation at the bifurcation regime, the system is bound

to exhibit bursting behaviour with large amplitude bursts. We experimentally showed that the state of the bursting, in the regime of canard explosions, consists of very high amplitude fluctuations amidst low amplitude fluctuations.

It is important to note that according to past studies, in this rapid transition, small oscillations emerge from a Hopf bifurcation to large relaxation-type oscillations characterized by alternating slow and fast phases. A family of periodic orbits can be observed following a segment of the unstable inner branch of the critical manifold for a significant duration. These trajectories are known as canard orbits, giving rise to the term canard explosion (Eckhaus, 1983). The transitions described in our experimental results don't involve the relaxation oscillations as the traditional literature on the canard explosions describes. However, we note that the transition is steep and continuous in nature. We also observe that a low-amplitude oscillatory state emerges from a very low-amplitude aperiodic state, which can be related to the Hopf bifurcation analogy (please refer to A.1). Moreover, a peculiar type of bursting that has an amplitude of bursts ranging from low amplitude limit cycle to high amplitude limit cycle oscillation is observed, and they occur at the rapid transition regime. The appearance of the bursts having high and low amplitude periodic oscillations hints towards an underlying rapid continuous transition.

CHAPTER 6

TRANSITIONS IN AEROACOUSTIC SYSTEMS

Oscillatory instabilities are a common phenomenon in fluid flows, often accompanied by a high degree of coherence in turbulent reactive flows. For instance, during thermoacoustic instability, large coherent structures emerge within the turbulent flow (Sujith and Unni, 2020). This behaviour is an indication of the characteristics of complex systems. The self-organization in turbulent flow leads to the development of an ordered acoustic field and large coherent structures, all occurring without any need for external forcing. Emergence is a key feature of complex systems. The approaches and techniques from complex system theory used to study thermoacoustic instabilities can similarly be applied to examine flow-induced oscillatory instabilities in other fluid dynamic systems. Thus, in the spirit of complex systems, the current thesis explores the commonality of the transitions in fluid flows of thermoacoustic and aeroacoustic systems.

Now, we shift our focus to an aeroacoustic system where the acoustic field is influencing the acoustic source. However, unlike thermoacoustic systems, the energy component for acoustic power does not include heat release rate fluctuations in aeroacoustic systems. The source of acoustic power in these aeroacoustic systems originates from the hydrodynamic flow instabilities involving turbulent shear layers and vortex shedding. Self-sustained aeroacoustic oscillations arising from the interactions between the hydrodynamic and acoustic fields are perceived as a whistle. Such whistling can lead to large amplitude acoustic oscillations that have disastrous consequences for engineering systems such as large segmented solid rocket motors and large gas pipelines. The whistling corresponds to the state of limit cycle oscillations (LCO) in dynamical systems theory. An aeroacoustic

The results presented in this chapter are published in Bhavi, R. S., Pavithran, I., and Sujith, R. I. (2024), Dynamical states associated with the shift in whistling frequency in aeroacoustic system, *Journal of Sound and Vibration*, 592, 118606. <https://doi.org/10.1016/j.jsv.2024.118606>

system exhibits different dynamical states when the bulk flow velocity is varied as a control parameter. Understanding the dynamical states and the transitions between them, as the control parameter is varied, is crucial in designing control strategies for such aeroacoustic oscillations. The past studies have shown that as the control parameter varies, in an aeroacoustic system that has a flow through orifices, the whistling frequency shifts.

In this chapter, it is shown that such a change in frequency occurs via three different scenarios: (1) direct transition between the two LCOs as an abrupt transition, (2) via a state of intermittency, and (3) via a state of aperiodicity. In the current aeroacoustic system, the abrupt transition between the LCOs is manifested as a bursting behaviour where the amplitude of the acoustic pressure fluctuations abruptly switches between high and low-amplitude LCOs. Further, the current study shows that the dynamical state and the transition between them during the frequency shift have a correlation with the magnitude of the frequency shift. Using recurrence theory we show that there is a change in the dynamical state of the system during the frequency shift. Further, synchronisation analysis is used to investigate the coupled behaviour of the velocity (u') and the acoustic pressure (p') fluctuations during the different dynamical states. Our findings imply that u' and p' exhibit phase synchronisation (PS) during the state of LCO, corresponding to whistling. In contrast, u' and p' are desynchronised during the state of aperiodicity, corresponding to stable operation. Furthermore, the bursts of periodic oscillations during intermittency correspond to the phase-synchronised epochs of periodic u' and p' , and the aperiodic epochs correspond to the desynchronised aperiodic u' and p' .

6.1 DYNAMICAL STATES ASSOCIATED WITH SHIFTS IN WHISTLING FREQUENCY

To investigate the dynamical states in the aeroacoustic system, Re is increased by changing the inlet airflow rate. Figure 6.1a shows the changes in the root mean square value (rms)

of the acoustic pressure fluctuations p'_{rms} as Re is increased. As Re is increased from 4,000 to 12,700, a rise and fall in the value of p'_{rms} attaining successive maxima followed by minima is observed.

Figure 6.1b shows the corresponding changes in the dominant frequency (whistling frequency) of p' with Re . The dominant frequency from the amplitude spectrum of the acoustic pressure fluctuations is computed using the fast Fourier transform (FFT). The resolution of the amplitude spectrum considered here is 0.2 Hz. A switch in dominant frequencies from 461 to 411, 443 to 535, 535 to 411, and 445 to 470 Hz is observed when the value of Re crosses the values 5, 100, 7, 500, 8, 300, and 12, 000, respectively; please refer to the intersection regime of R1-2, R2-3, R3-4, and R4-5 in figure 6.1(a, b). A detailed view of the amplitude spectrum during the frequency shifts is represented in the waterfall plots of figure 6.1e-h. In the following subsections, the different routes of frequency shifts and the associated dynamical states observed in the aeroacoustic system as Re increases beyond 4,000 are described.

Transition via the state of intermittency

The change in the value of p'_{rms} begins from a local minimum at $Re = 4,000 \pm 101$ (Fig. 6.1a), where the value of p'_{rms} is approximately equal to 1 Pa. Upon increasing Re , p'_{rms} gradually increases to a local maximum at $Re = 5,100 \pm 110$ (marked as i in Fig. 6.1a). We observe the state of LCO (Fig. 6.1c-i) at this local maximum ($p'_{\text{rms}} = 9.5$ Pa). With further increase in Re , the value of p'_{rms} decreases to a second local minimum ($p'_{\text{rms}} = 1.7$ Pa, marked as ii in Fig. 6.1a). This transition from a local maximum to a local minimum is accompanied by a shift in the dominant frequency of p' (Fig. 6.1e) from 461 to 411 Hz. We observe that this frequency shift occurs via the state of intermittency (Fig. 6.1c-ii), which is characterized by bursts of periodic oscillation amidst epochs of aperiodicity. We also observe the states of intermittency during the subsequent frequency shifts, which are shown in Appendix B.2. The value of p'_{rms} further increases, with increasing Re , to a subsequent higher local maximum ($p'_{\text{rms}} = 46.6$ Pa, marked as iii in

Fig. 6.1a) when the value of Re equals $7,500 \pm 129$. The dynamical state corresponding to this local maximum is an LCO, as shown in figure 6.1c-iii.

Upon further increasing Re beyond 7,500, we note a sudden dip in the value of p'_{rms} from 46 to 8.5 Pa. This decrease is accompanied by a shift in dominant frequency from 443 to 535 Hz (Fig. 6.1f and the interface of the region R2 & R3 in Fig. 6.1b). We again note that the switch in the dominant frequency occurs via a state of intermittency (refer to Fig. B.2a of Appendix B.2). With a further increment of Re , a similar trend of rise in p'_{rms} is observed, reaching a local maximum and subsequently decreasing to a minimum with a change in the dominant frequency of p' fluctuations from 535 to 411 Hz (Fig. 6.1g). During this frequency shift, we found that the transition occurs via the state of intermittency (refer to Fig. B.2c of Appendix B.2). Thus, when Re is increased from 4,000 to 9,200, we have shifts in whistling frequency between the regions R1-R2, R2-R3, and R3-R4 (Fig. 6.1b). During these frequency shifts, we observe that the dynamical state is intermittency. When the value of Re is varied beyond 9,200, the transition associated with the shift in whistling frequency changes and we describe this observation in the following subsection.

Abrupt transition between states of limit cycle oscillations

When we varied Re beyond 9,200, the value of p'_{rms} increases to a higher p'_{rms} of 170 Pa at $Re \approx 12,000 \pm 165$; here we observe that the dynamical state is LCO. With the continued increase in the value of Re , we observe an abrupt jump to another state of LCO having a lower amplitude with the value of $p'_{\text{rms}} = 60$ Pa (marked as iv & v in Fig. 6.1a). The time series corresponding to the abrupt transition are shown in figure 6.1d. This abrupt jump is accompanied by a slight frequency shift from 445 to 470 Hz (Fig. 6.1h). However, when we further investigated this abrupt transition by varying the control parameter in finer steps of $Re = 70$ at the bifurcation regime, a bursting phenomenon is observed (Fig. 6.2). We observe that the state of the system switches between the LCOs of rms values 170 Pa and 60 Pa (Fig. 6.2b, c, d).

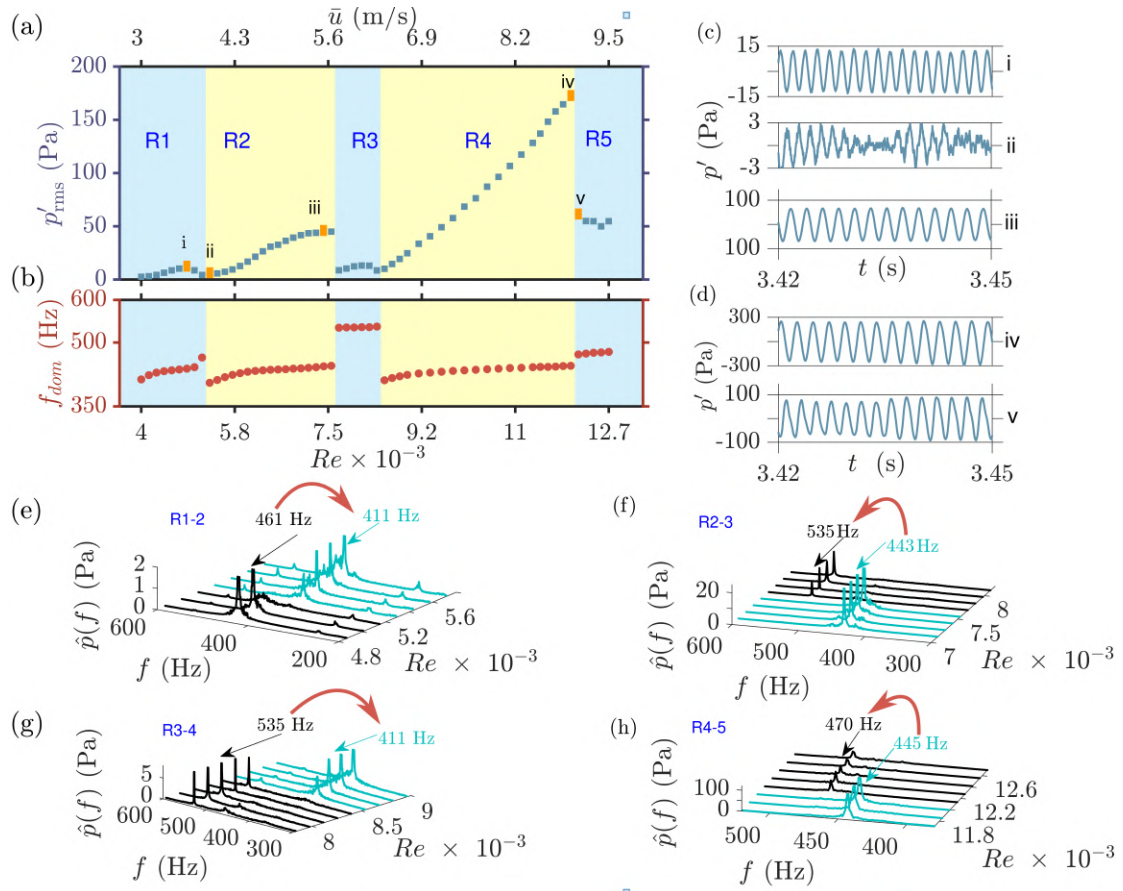


Figure 6.1: (a) rms of the acoustic pressure oscillations p'_{rms} (Pa) as a function of Re . The corresponding average flow velocity \bar{u} (m/s) of the airflow across the orifice is marked on the top abscissa. (b) The dominant whistling frequency of p' as Re is varied. The regions corresponding to the particular dominant frequency of p' signal are categorized as R1, R2, R3, R4, and R5. The shifts in dominant frequency are observed as Re is varied. (c) The time series corresponding to the transition via the state of intermittency during the shift in whistling frequency from 461 to 411 Hz; (ci) LCO, (cii) intermittency, and (ciii) LCO. (d) Time series of LCOs corresponding to the abrupt transition from one LCO to another (transition from point iv to v, marked in p'_{rms} variation) with a slight shift in dominant frequency. (e-h) Waterfall diagram of the amplitude spectrum for a particular range of Re during the shift in dominant frequency spectrum from regions R1-2, R2-3, R3-4, and R4-5.

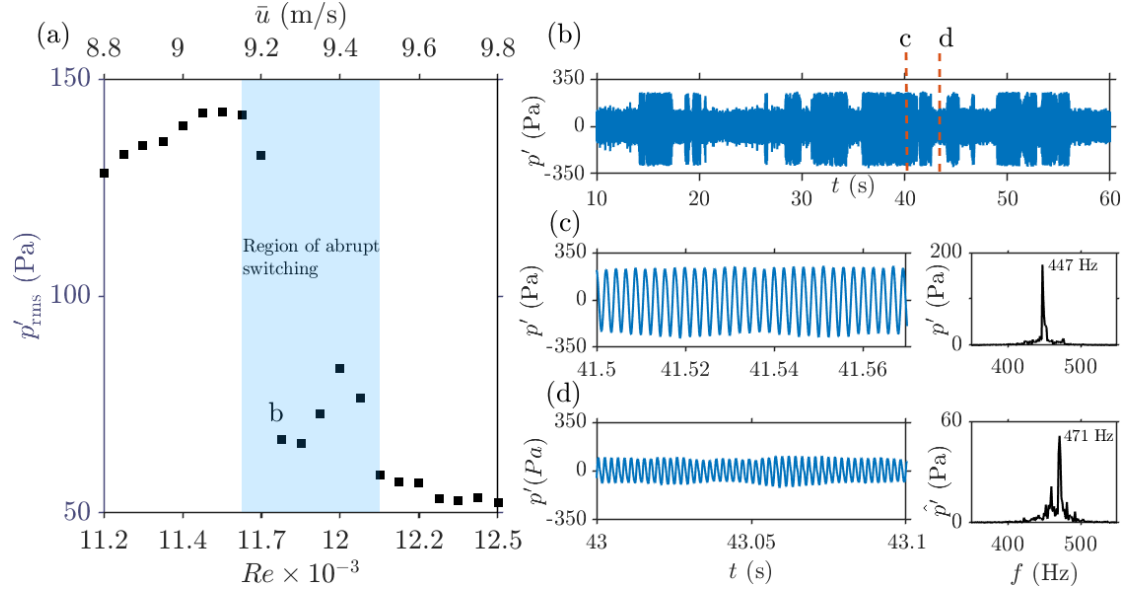


Figure 6.2: Representation of the state of bursting, having sudden shifts between high and low-amplitude LCOs during the frequency shift. (a) Variation of p'_{rms} with Re . (b) The times series of p' corresponds to the state of abrupt switching between the high and low-amplitude LCOs. (c) The zoomed-in view of the high-amplitude LCO and its corresponding amplitude spectrum. (d) The zoomed-in view of the low-amplitude LCO and its corresponding amplitude spectrum.

In contrast to the state of intermittency, where switching occurs between periodic and aperiodic states, here, we observe switching between two periodic states of different amplitudes, which manifests as a bursting phenomenon. We conjecture that the abrupt switching dynamics is due to the fluctuations in the strength of the lock-in phenomenon between the acoustic and hydrodynamic modes caused by the turbulence. Moreover, the sudden occurrence of high-amplitude LCOs amidst the low-amplitude LCOs indicates an underlying abrupt transition.

We note that p'_{rms} continues to decrease with a further increase in Re beyond 12,000. Hence, we further varied Re until 21,000 to investigate the subsequent dynamical state that the system exhibits. In the following subsection, we list the observed dynamical states with further increase in Re .

Transition via the state of aperiodic oscillations

Figure 6.3 represents the occurrences of the dynamical states for the variation of Re beyond 12,600. As Re increases, the system exhibits a state of intermittency for the range of Re varying from 14,700 to 15,500 (refer to Fig. 6.3a, b, c). With further increase in Re beyond 16,300, a state of aperiodicity is observed (refer to Fig. 6.3a, b, d). One can also note that, for $Re \geq 13,000$, the amplitude spectrum changes from having a sharp peak at 540 Hz to a broadband nature (refer to the waterfall diagram of Fig. 6.3b). Upon continuation with the increase in Re , the state of intermittency is encountered again, which extends to the range Re varying from 18,200 to 18,600 (Fig. 6.3b, e). With a further increase in Re beyond 18,600, the system enters the state of LCO corresponding to the frequency 920 Hz (Fig. 6.3 a, b, f).

Thus, from figure 6.1, it is observed that the aeroacoustic system exhibits a state of intermittency during the frequency shifts for the control parameter Re in the range of 4,000 to 8,600. However, for Re values greater than 8,600, an abrupt transition from one LCO to another LCO is observed during the frequency shift. For the values of Re beyond 16,000, the state of aperiodicity is observed during the frequency shift (Fig. 6.3). These are indeed different routes associated with the shift in whistling frequency. The observed dynamics arises due to the coupled interactions between the velocity fluctuations (u') and the acoustic fluctuations (p'). Hence, a further investigation of the coupled behaviour of u' and p' is performed in the following subsection.

6.1.1 The phenomenon of lock-in between the acoustic and hydrodynamic modes

The vortex shedding process from the orifice has different hydrodynamic modes based on Re (Nomoto and Culick, 1982; Huang and Weaver, 1991). The lock-in between the vortex shedding and the acoustic modes leads to the whistling phenomenon. There is a gradual desynchronisation of the hydrodynamic mode from the acoustic mode, which results in a decrease in the whistling sound as the control parameter Re increases. In order to illustrate this gradual decrease in the strength of lock-in, the joint recurrence

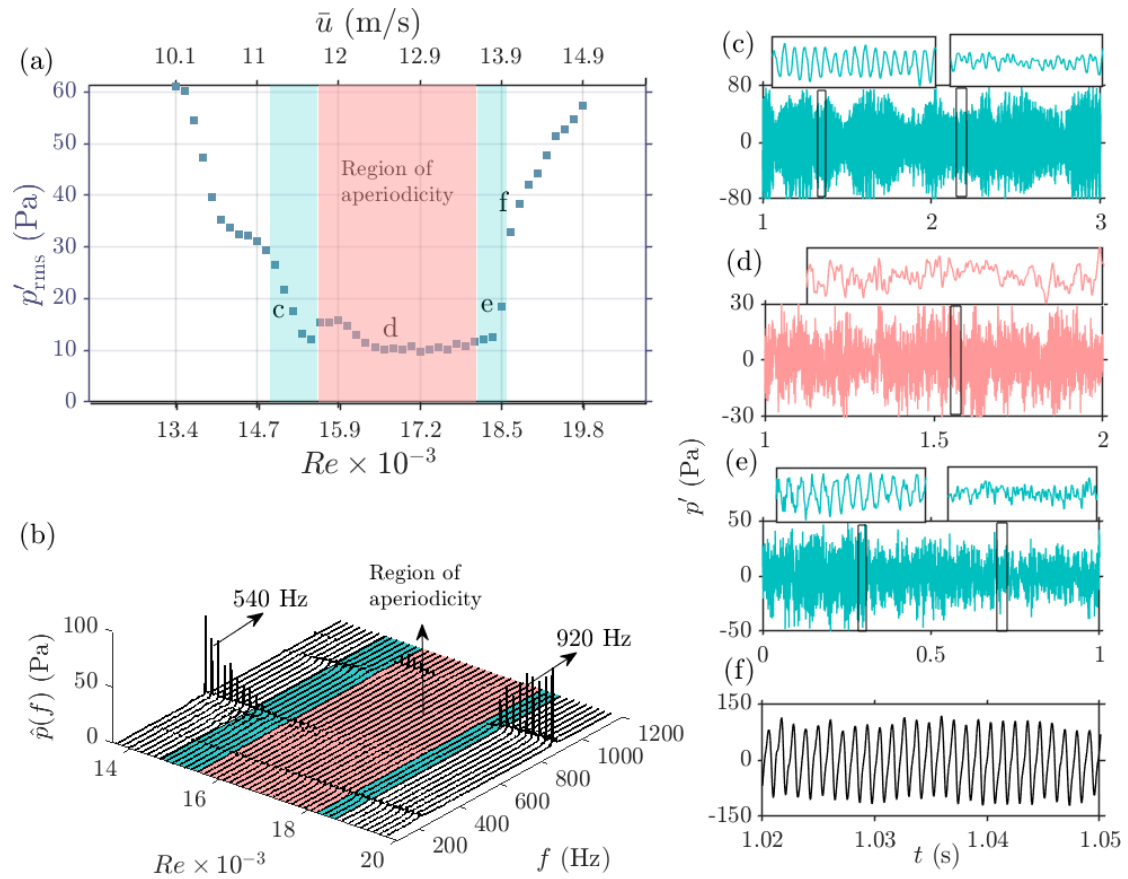


Figure 6.3: Representation of the state of aperiodicity when there is no lock-in between the acoustic and hydrodynamic modes. (a) Variation of p'_{rms} for the range of Re varying from 13,000 to 20,000 and the corresponding (b) waterfall plot to show the variation of the amplitude spectrum with Re . The mint blue coloured patches represent ($Re = 14,700-15,500$ and $18,200-18,600$) the states of intermittency. The pastel red patch denotes ($Re = 15,500$ to $18,200$) the aperiodic state, where the amplitude spectrum is a broad band in nature. A large shift in frequency from 540 Hz to 920 Hz is observed for a transition via the state of aperiodicity. The time series for the states of (c) intermittency, (d) aperiodicity, (e) intermittency, and (f) LCO.

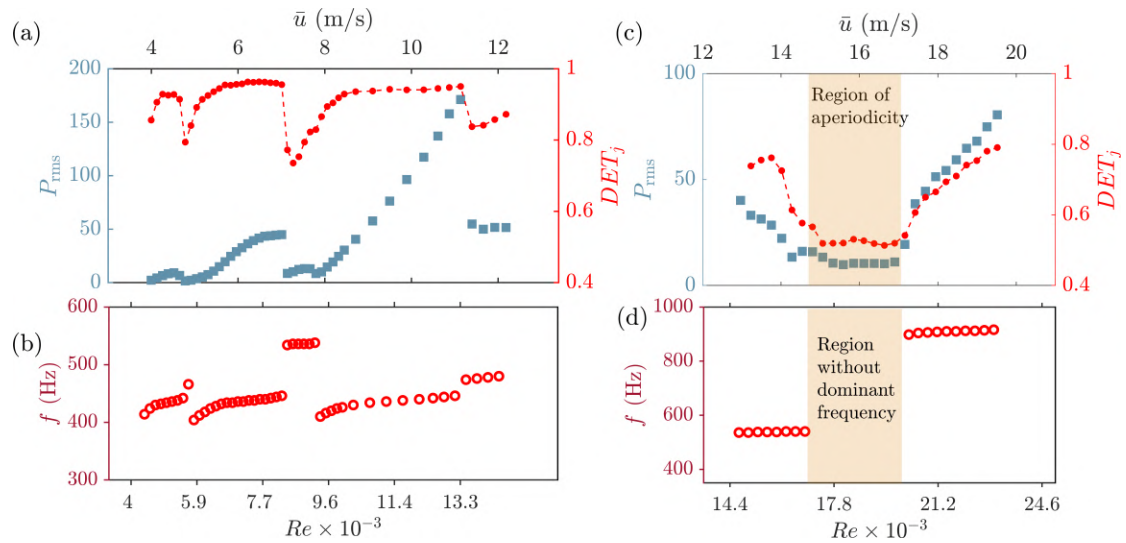


Figure 6.4: Representation of the variation of DET_j and p'_{rms} as a function Re (a) for the range of Re varying from 4,000 to 13,000 where the states of intermittency and abrupt transition is observed; (b) The corresponding variation in the dominant frequency. The variation of DET_j and p'_{rms} with Re (c) for the range of Re varying from 14,000 to 21,200 where we observe the states of aperiodicity, and (d) the corresponding variation in the dominant frequency. We observe a decrease in the values of DET_j during the frequency shifts for the state of intermittency and the state of aperiodicity (in the brown background). A very negligible change in DET_j is observed during the abrupt transition between the LCOs at $Re \approx 13,000$

quantification measure, Determinism DET_j (refer to Section Section 2.3), between the signals from the microphone and the hot film probe is computed at each of the control parameter values Re . DET_j is 1 when the signals are phase-locked in the time domain and is zero when there is no phase synchrony between the signals.

Figure 6.4 indicates the variation in DET_j as a function of Re . The variation of p'_{rms} along with DET_j is also plotted. For the transitions via the states of intermittency during the frequency shifts ($4,000 \leq Re \leq 12,000$), we observe that the variation in DET_j decreases to a local minimum and then subsequently increases (shown in light blue patches of Fig. 6.4a). A very negligible change in DET_j is noticed during the abrupt transition between the two LCOs ($Re \approx 12,000$). This observation is expected as there is a lock-in between the acoustic and the hydrodynamic modes during the states of LCO. However, for the transitions via the states of intermittency, the decrease in DET_j implies that the acoustic and the hydrodynamic modes begin to lose the strength of lock-in between them. The decrease in the strength of lock-in results in the system approaching the state having a very low sound pressure level (Nomoto and Culick, 1982). We also compute DET_j for the transition involving the state of aperiodicity (refer to Fig. 6.4 (c)). We observe that DET_j decreases as Re increases and has the lowest values for the aperiodic region when compared to the regions of intermittency. For further increase in $Re > 18,300$, DET_j again increases.

Further, an increase in DET_j is observed if the subsequent lock-in region is near the existing value of the control parameter Re . The increase in DET_j , as Re increases, indicates the beginning of the lock-in of the subsequent hydrodynamic and acoustic modes. However, the flow through the orifice also has fluctuations in velocities due to turbulence (Kamin *et al.*, 2019), which can create variations in the strength of the lock-in between the hydrodynamic and acoustic modes. We observe low-amplitude aperiodic fluctuations of acoustic pressure when the modes are not locked. However, if the frequency of the hydrodynamic mode is close to the frequency of the duct acoustic

mode, there is a sporadic response from the shear layer separation process to form a larger vortex to give rise to a periodic epoch (Kamin *et al.*, 2019). This occasional response of the shear layer manifests as fluctuations in the strength of the lock-in process. Thus, the fluctuations in the strength of the lock-in give rise to the state which has the imprints of periodicity amidst aperiodicity in the acoustic pressure fluctuations. Such a state having periodic epochs amidst aperiodic regimes corresponds to the state of intermittency (Kamin *et al.*, 2019).

Further, we observe a trend in the magnitude of the shift in the whistling frequency associated with these three routes, which are intermittency, abrupt switching between LCOs, and aperiodicity. In these three cases, the manner in which lock-in between acoustic and hydrodynamic modes occur is different. We observe that the magnitudes of the shift in frequency during the transition via intermittency are 50, 90 and 125 Hz, which are relatively high compared to the frequency shift (25 Hz) during the state of abrupt switching between the LCOs. For a relatively small frequency shift, the control parameter Re values for the lock-in region of current and the subsequent modes are nearby, thus allowing the subsequent modes to lock-in before even the system loses the strength of lock-in from the current modes. Hence, we observe the abrupt switching between the two LCOs, which manifests as bursting. In the case of transition via intermittency, the shift in frequency is larger, implying that Re values between the two lock-in regions are far apart. Thus, when the shift in frequency is large, the system continues to lose the strength of lock-in between the current modes to reach the aperiodic state and then followed by the beginning of lock-in of the subsequent modes. In the case of frequency shift occurring via the state of aperiodicity, the shift is 380 Hz (refer to Fig. 6.3a,b). This frequency shift is significantly larger than the frequency shifts for the state of intermittency (125 Hz) and abrupt transition (25 Hz). Thus, the control parameter (Re) values for lock-in regions are significantly far apart when we observe the state of aperiodicity.

Motivated by these findings, we utilize a visualization technique based on the theory of

recurrence (Marwan *et al.*, 2007) to characterize the dynamical states of intermittency, LCO and aperiodicity in the following subsections. Further, the high values of DET_j during the state of LCO and the lowest value of DET_j during the state of aperiodicity indicate that there is a variation in the synchrony between the dynamics of u' and p' . Thus, we study the behaviour of u' and p' variables in the purview of synchronisation analysis in the subsequent sections.

6.1.2 Characterizing the dynamical states using recurrence

Figure 6.5 represents the plots for the recurrence matrix obtained for p' oscillations for the state of intermittency at $Re \approx 5, 100$, the state of abrupt switching between the LCO at $Re \approx 12, 000$, and the state of aperiodicity at $Re \approx 16, 800$. For the state of intermittency, the phase space is reconstructed with an embedding dimension of $D = 7$ and an optimum delay of $\tau_{opt} = 0.7$ ms; For LCO, D is 5 and τ_{opt} is 0.5 ms. The recurrence matrix is obtained based on choosing a fixed value for the threshold $\epsilon = \lambda/5$, where λ is the highest span between the pairs of locations of the trajectory in phase portrait (Marwan *et al.*, 2007). For the state of intermittency, the recurrence plot is seen to have perforated black patches among white regions (Fig. 6.5a). The occurrence of black patches in RP is due to the regime of low-amplitude aperiodic oscillations of the state of intermittency (Kabiraj and Sujith, 2012; Nair *et al.*, 2014). The white patches correspond to the bursts of periodic oscillations of the state of intermittency (Kabiraj and Sujith, 2012). Similar observations are made for the intermittency states at $Re \approx 7, 500$ and $Re \approx 8, 400$ (refer to Fig. C.1 of Appendix C.1).

The periodic signal has equidistant diagonal lines in the RP. The time period of the LCO can be computed using the distance between the diagonal lines (Marwan *et al.*, 2007). Figure 6.5c-d represents the time series and RP for the state of abrupt switching between the LCOs corresponding to 445 and 470 Hz. We observe that the diagonal lines corresponding to low-amplitude LCO of 470 Hz are more closely spaced than the diagonal lines corresponding to the high-amplitude LCO of 445 Hz (refer to the

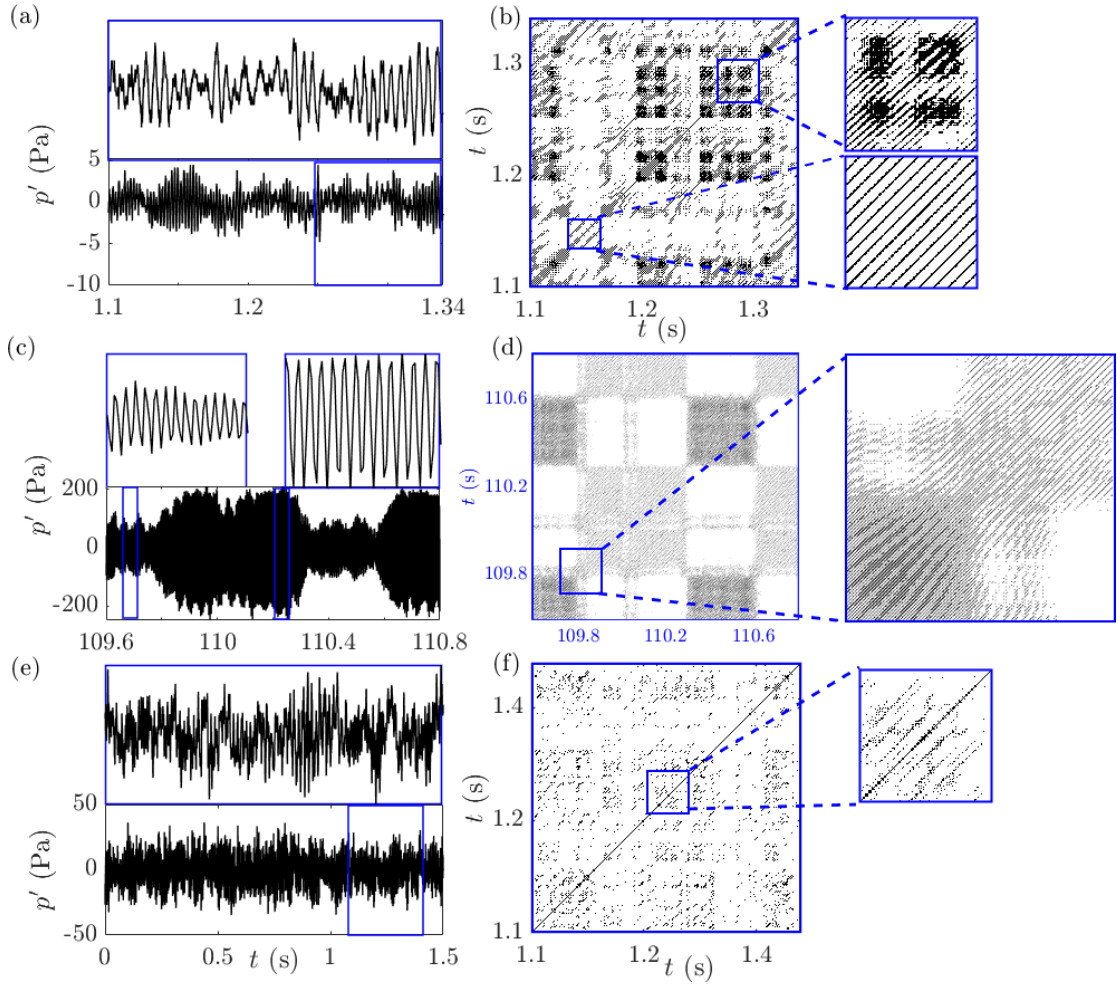


Figure 6.5: The plots for p' fluctuations and the corresponding recurrence matrix obtained during (a,b) the state of intermittency ($Re \approx 5, 100$), (c,d) the state of abrupt switching between the limit cycle oscillations ($Re \approx 12,000$) and (e,f) the state of aperiodic oscillations ($Re \approx 16,800$). The recurrence plots are plotted based on choosing a fixed value for the threshold $\epsilon = \lambda/5$, where λ is the maximum diameter of the reconstructed attractor in the phase space. The recurrence plot for the state of intermittency (b) has black patches, which correspond to the low amplitude aperiodic oscillations relative to λ . The recurrence plot for the abrupt switching between the LCOs (d) has the variation in the spacing between the diagonal lines (zoomed-in view, d), indicating the temporal switching of frequencies corresponding to LCOs. The presence of short, broken diagonal lines in the recurrence plots for aperiodicity (e) indicates the deterministic behaviour of the aperiodic oscillations.

zoomed-in version of the Fig. 6.5d). The change in spacing between the diagonal lines indicates that there is a temporal switching between the two states of LCO of different frequencies. Such an observation in RP, however, a bursting phenomenon between the silent and period states is also observed in the time series dynamics of thermoacoustic systems (Kabiraj and Sujith, 2012). The equidistant diagonal lines are also observed in the recurrence plots for the states of LCO at $Re \approx 4,800, 7,300, 8,100,$ and $12,200$ (Fig. C.1 of Appendix C.1). Further, we also show the RP for the aperiodic state at $Re = 16,800$ (Fig. 6.5(e,f)). The presence of short, broken diagonal lines indicates the deterministic behaviour of the aperiodic oscillations. Moreover, the p' during the aperiodic dynamics contains the small epochs of periodic dynamics due to the certain flow-induced acoustics at chamber resonance and results in the short diagonals lines in RP (Kabiraj *et al.*, 2015b). The observation indicates the possibility of chaotic dynamics. However, dedicated tests are required to confirm the dynamics of chaos.

Investigating the change of dynamical states using RQA

The aeroacoustic system exhibits the rich dynamical states and transitions between them upon varying the control parameter. In order to quantify the changes in the dynamical states, we extract the information from the topology of the recurrence plot using the recurrence quantification measure. To obtain and compare the quantifiable measure across various values of Re , we fix the threshold ϵ to a specific value.

Here, we choose the threshold ϵ to be of the size of the attractor corresponding to the aperiodic state of the intermittency during frequency shift. The size of the attractor corresponds to the maximum diameter of the reconstructed attractor in the phase space.

We present the variation of RR during the shift in whistling frequency in figure 6.6. The first column represents the variation of p'_{rms} with Re (Fig. 6.6(a-e)-i). The second column denotes a shift in whistling frequency with Re (Fig. 6.6(a-e)-ii). The corresponding variations in RR during the frequency shift are shown in the third column (Fig. 6.6(a-e)iii).

The plots corresponding to transitions via the state of intermittency are grouped in the peach-coloured background. We note that as Re varies, the curves of RR increase and then decrease (Fig. 6.6(a-c)iii). This observation is due to an increase in the number of black points in the RP as the system approaches the state of intermittency. The rise in black dots is attributed to the fact that the pairwise separation length rarely crosses the threshold ϵ during the aperiodic epoch of the state of intermittency. Thus, the curve of the recurrence measure RR rises during the frequency shift. This variation in RR confirms the loss of periodicity while the system transits from one whistling frequency to another.

The plots corresponding to the abrupt switching from one LCO to another LCO are shown in the green background (Fig. 6.6d). In contrast to the transition via intermittency, we observe that the values of RR are low, and the variation in RR is negligible for the abrupt transition between the two LCOs. This observation is expected since both the states are of LCO, and the pairwise distance regularly crosses the threshold ϵ (Fig. 6.6diii). Further, the plots corresponding to the transition via the state of aperiodicity are presented in the light blue shade (Fig. 6.6e). Similar to the transition via the state of intermittency, during the frequency shift, we observe an increase and subsequent decrease in the value of RR with the control parameter Re (Fig. 6.6e-iii). However, the value of RR stays at 1 for a range of Re (16,300 to 18,300), implying that the state of aperiodicity extends for a larger range of Re in comparison to the range of Re for the state of intermittency (Fig. 6.6(a,b,c,e)-iii).

Further, the co-existence of the coupled acoustic and hydrodynamic subsystems in a confined flow gives rise to the synchronisation between the two. Thus, the synchronisation strength between the system variables, u' and p' fluctuations, is an important criterion for understanding the mechanism through which the observed dynamical states occur during the frequency shift. Hence, we investigate the coupled dynamics between the two different variables, u' and p' , of the current system using the theory of synchronisation.

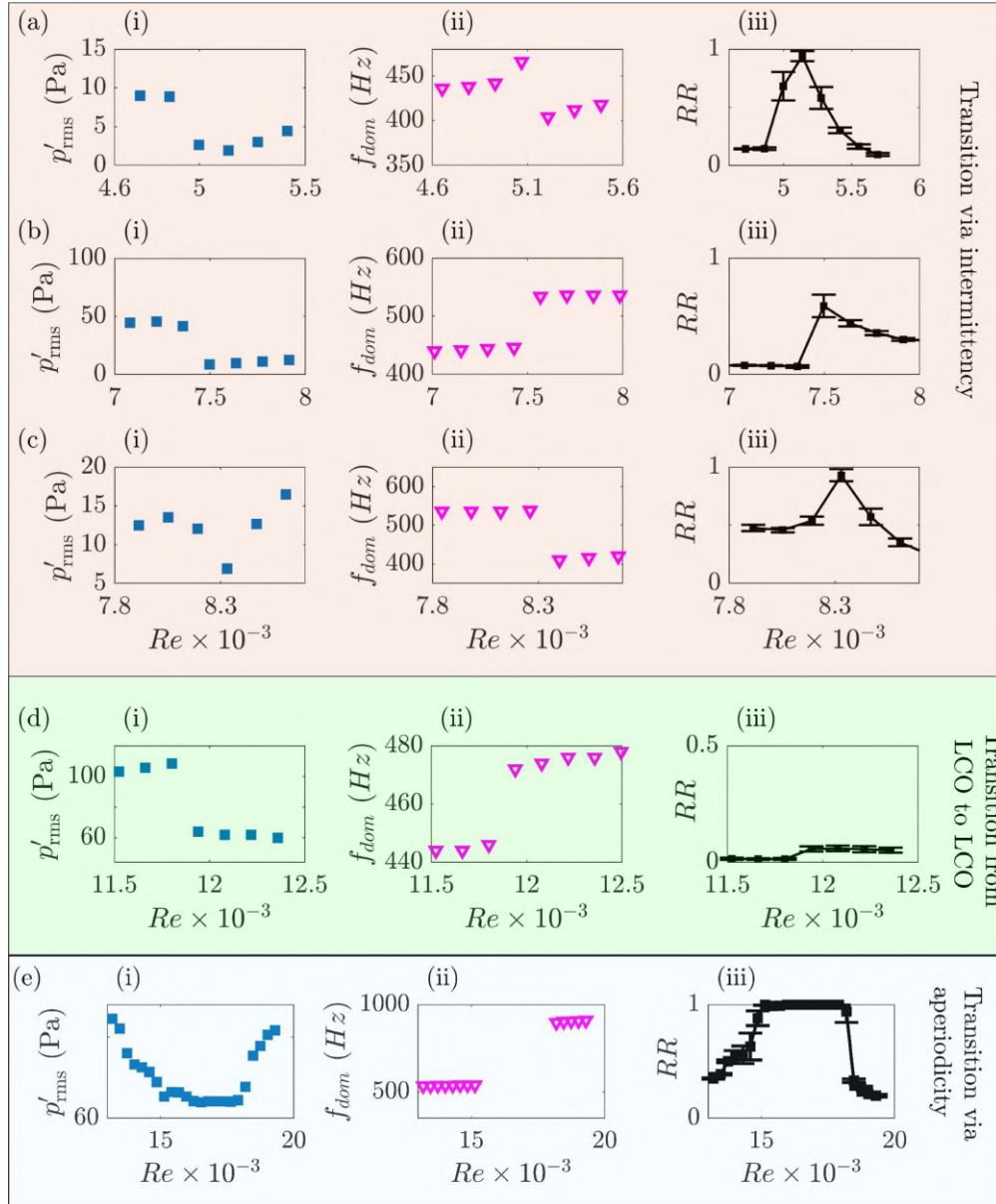


Figure 6.6: Representation of the variation of the recurrence quantification measure RR during the transitions corresponding to the shifts in whistling frequency via the state of intermittency (peach-coloured box), via an abrupt switching from one LCO to another LCO (green box), and via the state of aperiodicity (light blue box). (a-e)i The variation of p'_{rms} is shown in the first column ($Re \approx 4,600-5,500, 7,000-8,000, 7,800-8,600, 11,500-12,500$ and $14,000$ to $19,800$). (a-e)ii The corresponding variation in the dominant frequency f is shown in the second column. The shaded region represents the absence of dominant frequency (eii). The variation in the RQA measure (a-e)iii recurrence rate RR is shown in the third column. The RQA measure is computed for an embedding dimension of 7 and the optimal τ of 0.7 ms. At each control parameter, the signal of length 1,00,000 points is parted into sections of 5,000 points, and the mean values of RQA are plotted. The error bar represents the standard deviation. We observe a rise and dip in the value of the RQA measure RR for the transitions via the states of intermittency and aperiodicity.

In the following subsection, we plot joint recurrence matrices to understand the level of synchronisation between u' and p' during the states of intermittency, LCO and aperiodicity.

6.1.3 Investigating the synchronised dynamics of the acoustic and hydrodynamic field

Figure 6.7 represents the joint recurrence plots (JRP) of the phase trajectories of u' and p' corresponding to the state of intermittency at $Re \approx 5,100$, LCO at $Re \approx 12,000$ and the state of aperiodicity $Re \approx 16,800$ (Fig. 6.7a and c). The corresponding time signal of the acoustic pressure p' and velocity u' fluctuations are shown in the subfigures b, d, and f of figure 6.7. The value of ϵ is selected such that the recurrence rate (RR) for the individual recurrence matrix remains fixed, which is 0.1. A simultaneous recurrence of u' and p' would manifest as a black dot in the JRP. The black dots are sparsely distributed in an irregular pattern during the desynchronised state due to the aperiodic nature of the two subsystems. The sparse distribution during the desynchronised state is a result of the fewer occurrences of the simultaneous recurrences in the trajectories of u' and p' .

During the states of intermittency, we observe the sparsely spaced irregular black patches due to the aperiodic epochs and the diagonal lines due to the simultaneous recurrence of the trajectories of periodic epochs of u' and p' (Fig. 6.7a). During the state of LCO, we observe that most of the area in JRP is filled with diagonal lines. Note that the diagonal lines are more pronounced during LCO than during the periodic epochs of the intermittency (Fig. 6.7c), implying a higher correlation between u' and p' . During the state of aperiodicity, we observe the sparsely spaced black dots in JRP (Fig. 6.7e), implying that there is no correlation between u' and p' .

The states of intermittency observed at higher Re also exhibit similar JRP structures (Fig. C.2c, e). The occurrence of diagonal lines in the JRP corresponding to the states of LCO at $Re \approx 4,800, 7,300, 8,100,$ and $12,200$ also depict the high correlation

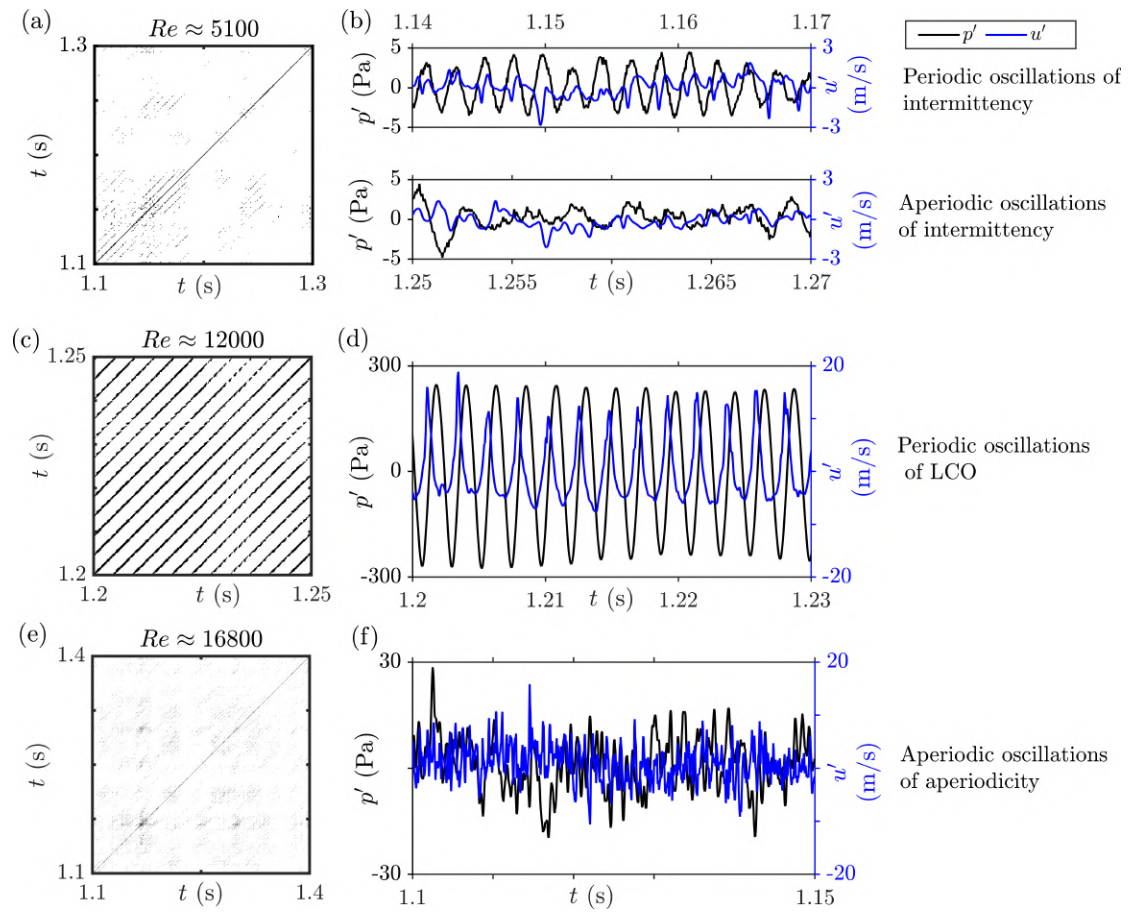


Figure 6.7: The representation of the JRP for (a) the state of intermittency at $Re \approx 5, 100$, (c) the state of LCO at $Re \approx 12, 000$ and (e) the state of aperiodicity $Re \approx 16, 800$. The corresponding signal of p' superimposed on u' oscillations during the (b) state of intermittency, (d) LCO and (f) aperiodicity are shown in the right subfigures. The presence of black dots in the joint recurrence plots represents the simultaneous recurrence of u' and p' . Diagonal lines are observed for the simultaneous recurrence of periodic u' and p' ; discontinuous diagonal lines are observed for the weakly coupled phase synchronised periodic limit cycle oscillations. During the periodic epochs of the state of intermittency as well, we observe discontinuous diagonals in the JRP. The density of the black dots is minimum during the desynchronised state of aperiodicity and the desynchronised epoch of the intermittency as a result of the very low simultaneous recurrence of u' and p' . A fixed RR of 0.1 is chosen to compute the recurrence matrix of the individual subsystems.

between u' and p' (Fig. C.2a, b, d, f). Thus, from the JRP, we observe that the strength of synchronisation is high during the states of LCO and is low during the states of intermittency.

We now quantify the topology of the joint recurrence plots using the RQA measures recurrence rate RR_J and determinism DET_J . Figure 6.8 represents the changes of DET_J and RR_J with Re . The first column represents the variation of p'_{rms} with Re (Fig. 6.8(a-e)-i). The second column denotes a shift in whistling frequency with Re (Fig. 6.8(a-e)-ii). The corresponding variations in DET_J and RR_J during the frequency shift are shown in the third and fourth columns, respectively (Fig. 6.8(a-e)iii & iv). The plots corresponding to transitions via the state of intermittency are grouped in the peach-coloured background, the abrupt switching between the states of LCO are in the green background, and the state of aperiodicity are in the light blue background. Note that as Re varies during the shift in whistling frequency that occurs via the state of intermittency, the curves of DET_J and RR_J decrease and then subsequently increase, indicating the decrease and increase of the synchronisation strength (Fig. 6.8(a-c)iii & iv). There is an overall decrease in the values of DET_J and RR_J during the transition from high-amplitude LCO to low-amplitude LCO, which indicates that the synchronisation strength reduces and is manifested as the reduction in the amplitude of the LCO. For the transition via the state of aperiodicity, we observe that DET_J and RR_J decrease, stay constant for the range of Re (16,300 to 18,300), and then rise. This observation implies that the strength of synchronisation is low for a longer range of Re for the transition via the state of aperiodicity.

Note that the values and variations of these recurrence measures depends on how we define the recurrence threshold ϵ while computing the recurrence matrix. In Section 2.2, we choose a fixed value of ϵ . The motivation behind choosing a fixed value of ϵ is to clearly capture and visualize the state of intermittency (Nair *et al.*, 2014), which has different amplitudes in the signal during the periodic and the aperiodic epochs. In that

case, for a fixed ϵ , there are more number of recurrence points within the radius of ϵ for the low-amplitude aperiodic trajectory. Hence, we observe that the measure RR rises as the system exhibits the states of intermittency and aperiodicity during the frequency shift. In contrast, when the value of ϵ is selected such that the recurrence rate RR remains constant. We compute the JRM by taking the dot product of the two recurrence matrices that are computed using fixed RR . We choose fixed RR so as to compare the simultaneous recurrence patterns observed between the different dynamical states of the system with fluctuations having different amplitudes. Though RR is fixed, the value of RR_J will be lesser when the trajectories of two signals do not recur at the same time. Thus, we observe a dip in the value of the measure RR_J when the system exhibits the state of intermittency and aperiodicity during the frequency shift.

The state of phase synchronisation

We further make use of the probability of recurrence to identify the type of synchrony that persists between u' and p' . The probability of recurrence quantifies the probability with which a state vector of the trajectory recurs after a time lag τ (Romano *et al.*, 2005).

In figure 6.9, we represent the plots for the variation in the probability of recurrence with the time lag τ , corresponding to the states of LCO, aperiodicity and intermittency. In order to study the coupled behaviour of the two subsystems u' and p' , we have overlapped the plots of $P(\tau)$ for u' and p' . We observe several peaks of $P(\tau)$ at regular intervals as the time lag τ increases, denoting the existence of a very high probability of recurrence at regular intervals for u' and p' during LCO (Fig. 6.9a). Further, the peaks of $P(\tau)$ of the two subsystems occur simultaneously, implying that the trajectories of u' and p' are phase-locked. Hence, we observe the state of phase synchronisation (PS) during LCO; note that the magnitude of the peaks of $P(\tau)$ for u' and p' are not matching, implying the absence of generalised synchronisation. During the state of aperiodicity, we observe very low values of $P(\tau)$ for u' and p' , and there is no correlation among $P(\tau)$, implying the existence of the desynchronised state (Fig. 6.9b). During the periodic

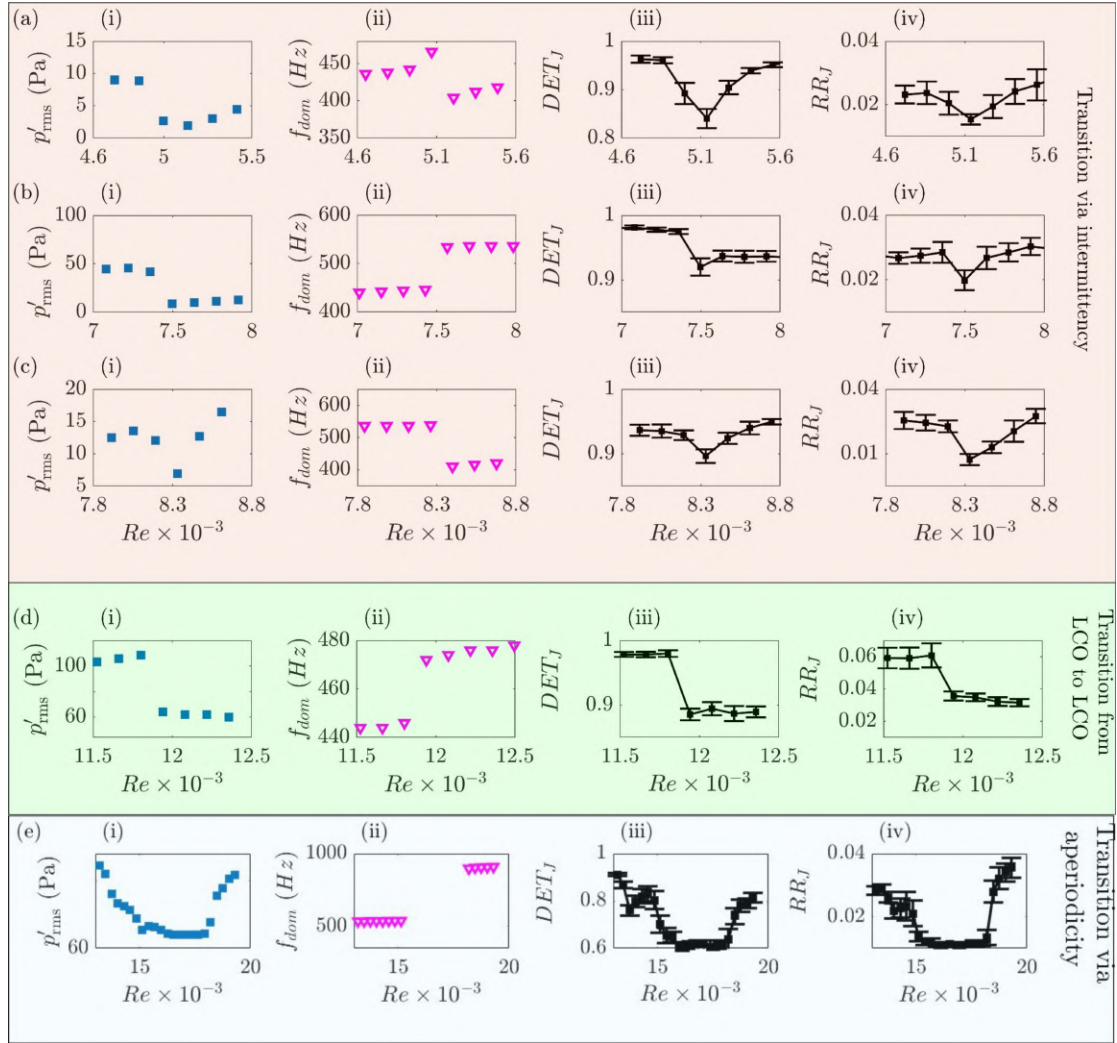


Figure 6.8: Representation of the variation of the RQA measures for JRP during the shifts in whistling frequency via the state of intermittency (peach-coloured box), through abrupt switching between the LCOs (green box) and through the state of aperiodicity (light blue box). (a-e)i The variation of p'_{rms} is shown in the first column for the ranges of $Re \approx 4,600-5,500$, $7,000-8,000$, $7,800-8,600$, $11,500-12,500$, and $14,000-19,800$, respectively. (a-e)ii The corresponding variation in the dominant frequency f_{dom} is shown in the second column. The shaded region represents the absence of dominant frequency (eii). The variation in the RQA measures (a-e)iii determinism DET_J and (a-e)iv recurrence rate RR_J for JRP are shown in the third and fourth columns correspondingly. The RQA measure is calculated from the JRM. The JRM is computed as the dot product of the two recurrence matrices obtained with an embedding dimension of 7, an optimal τ of 0.7 ms and a fixed RR of 0.1. At each Re , the signal of 1,00,000 points is parted into sections of 5,000 points, and the mean values of RQA measures are plotted. The error bar represents the standard deviation. A dip in the variation of RQA measure signifies a decrease in synchronisation strength during the shift in whistling frequency.

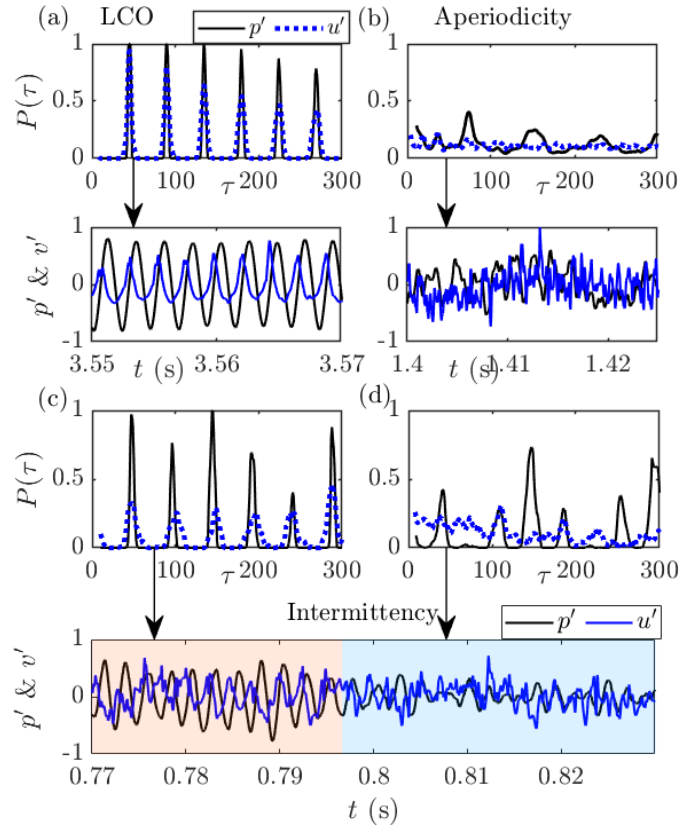


Figure 6.9: Characterization of the type of synchronisation observed during the states of LCO, aperiodicity and the states of intermittency using the RPs where we observe the variation of $P(\tau)$ with the time lag τ . The plots of $P(\tau)$ for u' and p' show (a) the state of phase synchronisation between u' and p' during the state of LCO, (b) the state of desynchronisation between u' and p' during the state of aperiodicity. (c) The state of phase synchronisation during the periodic epochs of the intermittency, and (d) the state of desynchronisation during the aperiodic regime of the intermittency. The corresponding normalized signals of u' and p' are shown in the bottom row of each subfigure.

epochs of intermittency, the peaks of $P(\tau)$ of the two subsystems occur simultaneously, implying that the trajectories of u' and p' are phase-locked (Fig. 6.9b) and it is a phase synchronised state. During the aperiodic epochs, the values of $P(\tau)$ of u' and p' are low, and there is no correlation among them, implying the desynchronised state (Fig. 6.9d).

Thus, we conclude that the state of LCO corresponds to the phase-synchronised state of u' and p' , implying a high strength of lock-in between the acoustic and hydrodynamic modes. We observe that the state of aperiodicity corresponds to the desynchronised state of aperiodic u' and p' . The state of desynchronisation implies the absence of lock-in between the acoustic and hydrodynamic modes. During the state of intermittency, we observe that periodic epochs of u' and p' are phase synchronised and the aperiodic epochs of u' and p' are desynchronised. Hence, the state of intermittency corresponds to the state of intermittent synchronisation. The state of intermittent phase synchronisation indicates that there are fluctuations in the strength of lock-in between the acoustic and hydrodynamic modes when Re is near the region of LCO.

6.2 CONCLUDING REMARKS

To summarize, we observed shifts in whistling frequency when the Reynolds number Re of the flow in an aeroacoustic system, having a flow through two orifices, is increased. We discovered that the shift in whistling frequency occurs via three different scenarios— (1) a direct transition between the two limit cycle oscillations (LCOs) as an abrupt transition, (2) via the state of intermittency, and (3) via the state of aperiodicity. The abrupt transition between the LCOs manifests as a state of bursting between the high-amplitude and low-amplitude LCOs. We characterize the observed dynamical states using the recurrence plots. During the frequency shift, we showed that there is a variation in the strength of lock-in between the acoustic and hydrodynamic modes using the Determinism DET_j . We used the synchronisation analysis to study the coupling behaviour between the velocity (u') and acoustic pressure (p') fluctuations for the transitions associated with

the frequency shifts. Using the probability of recurrence, we showed that the state of LCO corresponds to the state of phase synchronisation between u' and p' fluctuations. We also showed that u' and p' are desynchronised during the state of aperiodicity.

CHAPTER 7

CONCLUSIONS AND FUTURE PROSPECTS

The current thesis reports the transitions to high amplitude oscillatory instabilities in aero-thermoacoustic systems. An individual study of these systems as thermoacoustic and aeroacoustic systems is performed.

The current study begins with the observation of secondary bifurcation in three disparate turbulent combustors – annular combustor, swirl-stabilized combustor, and bluff-body stabilized combustor with preheated air – despite them having completely different flame responses and acoustic characteristics. These systems exhibit a sequence of transitions from combustion noise to intermittency to low-amplitude limit cycle oscillations, followed by an abrupt jump to large-amplitude secondary limit cycle oscillations. We then modelled the secondary abrupt bifurcations using a second-order oscillator equation containing higher-order nonlinearities. The effect of turbulence is incorporated in terms of Gaussian delta-correlated white noise. We show that the model captures the secondary bifurcation very well and depicts good qualitative agreement with the dynamical states observed in experiments. The Langevin equation of the slowly varying amplitude and phase is then derived through deterministic and stochastic averaging techniques. The potential function for the secondary bifurcation is obtained, and the stability of the observed dynamical states is discussed. In addition, the stationary distribution of the envelope of the amplitude of the fluctuations is also obtained by solving the Fokker-Plank equation.

The study shows that a deterministic subcritical bifurcation is transformed into a continuous sigmoid-type transition, typical of the intermittency route, in the presence of noise. By means of comparison, one can observe that for a given intensity of noise, which is high enough to transform a subcritical Hopf bifurcation into a continuous

one, the secondary bifurcation to a large amplitude limit cycle remains abrupt. The current study finds that a very high value of noise intensity is required for transforming a secondary bifurcation into a continuous transition. We, therefore, conclude that secondary bifurcations can have very high stability due to the presence of higher-order nonlinearities and can appear in turbulent combustion systems despite having relatively high levels of turbulent fluctuations. It is to be noted that the higher stability of secondary limit cycles reflects the system's high resilience to instability-control strategies, while their abrupt nature makes them exceedingly difficult to predict.

Upon further conducting experiments under different conditions, a transition which is rapid and continuous in nature was observed, which was referred to as canard explosions. The transition appears discontinuous when there is a lack of resolution in the variation of the control parameter. Though the rise in the magnitude of the fluctuations is steep in nature, unlike abrupt transitions, the canard explosion in this study exhibits no hysteresis. When such a transition involves a parameter fluctuation at the bifurcation regime, the system is bound to exhibit bursting behaviour with large amplitude bursts. The current study experimentally showed that the state of the bursting, in the regime of canard explosions, consists of very high amplitude fluctuations amidst low amplitude fluctuations.

We describe the transition via the canard explosion using the low-order model representing thermoacoustic systems. A continuous secondary bifurcation steepens at the bifurcation regime when the nonlinearity of the nonlinear damping in the model is reduced by coupling a small variable ϵ . In other words, the dynamics of the transition from stable operation to high amplitude oscillatory instability gets restricted to a very narrow range of control parameters for the values of $\epsilon \ll 1$. For such a steepened transition, we conjecture that the system amplitude becomes highly sensitive to the change in control parameter at the bifurcation regime, thus giving rise to a scenario of large amplitude bursts. We have noticed, from past studies, that the Van der Pol oscillator model is a well-accepted model

for describing the dynamics of thermoacoustic systems (Lee *et al.*, 2021; Bonciolini *et al.*, 2021). Past studies have even calibrated the model using techniques such as flame transfer function (Noiray, 2017). Our motive behind using the phenomenological Van der Pol oscillator model, corresponding to thermoacoustic systems, is to qualitatively illustrate the potentiality of these systems to exhibit a rapid continuous transition.

Further, during the state of bursting, we observe a slow variation in the fluctuation of the exhaust gas temperature in correlation with the envelope of the acoustic pressure fluctuation. The temperature of the exhaust gas represents the flame temperature as well as the fluctuation in the heat release rate, which in turn governs the dynamics of the thermoacoustic oscillations. We convey that parameter fluctuation has a role in bursting behaviour in the regime of canard explosion, as explained using the low-order thermoacoustic model.

We further investigate the transitions in an aeroacoustic system, where we observe that there is feedback from the acoustic field to the acoustic source. We observed shifts in whistling frequency when the Reynolds number Re of the flow in an aeroacoustic system, having a flow through two orifices, is increased. We discovered that the shift in whistling frequency occurs via three different scenarios— (1) a direct transition between the two limit cycle oscillations (LCOs) as an abrupt transition, (2) via the state of intermittency, and (3) via the state of aperiodicity. The abrupt transition between the LCOs manifests as a state of bursting between the high-amplitude and low-amplitude LCOs. We characterize the observed dynamical states using the recurrence plots. During the frequency shift, we showed that there is a variation in the strength of lock-in between the acoustic and hydrodynamic modes using the phase locking value (PLV). We used the theory of synchronisation to study the coupling behaviour between the velocity (u') and acoustic pressure (p') fluctuations for the transitions associated with the frequency shifts. Using the probability of recurrence, we showed that the state of LCO corresponds to the state of phase synchronisation between u' and p' fluctuations. We also showed that u'

and p' are desynchronised during the state of aperiodicity.

In conclusion, we observed that the difference in the frequency shifts during the state of intermittency is relatively high compared to what is observed during the state of abrupt switching between the LCOs. However, during the state of aperiodicity, the frequency shift is significantly higher compared to the shifts observed during the intermittency and the abrupt switching between the LCOs. The frequency shift indicates the loss in the strength of the lock-in between the current acoustic and hydrodynamic modes and the beginning of the lock-in for the subsequent modes. This observation is evident from the variation of PLV with Re , which decreases to a local minimum and then rises during the frequency shift. From the perspective of synchronisation theory, the frequency shift corresponds to a decrease and a subsequent increase in the strength of synchronisation, as depicted by the recurrence quantification analysis (RQA) measures of the joint recurrence matrix.

The existence of PS implies that during the state of LCO, the variables u' and p' significantly influence each other. The observation of the intermittent phase synchronisation indicates fluctuations in the strength of lock-in between the acoustic and hydrodynamic modes during the state of intermittency. We conjecture that the fluctuations in the strength of lock-in between the modes, in combination with the turbulent fluctuations, also result in the abrupt switching between the LCOs.

SCOPE FOR THE FUTURE WORK

In this thesis, we investigated the potentiality of turbulent aero-thermoacoustic systems exhibiting different transitions to oscillatory instabilities, specifically sudden transitions. The proposed model to describe abrupt transition and canard explosion can be utilized for system identification to predict the transitions in real time for turbulent combustors. Further, it is also important to understand the change in the nature of bifurcation as an additional parameter is changed in these turbulent fluid mechanical systems. For instance,

studies in the past have shown that the nature of bifurcations changes as the turbulence intensity, as an additional parameter, is changed (George *et al.*, 2018; Nagarajan *et al.*, 2019). However, a systematic variation of this additional parameter, which reveals the change in the nature of bifurcation, is missing in past studies. The turbulent aero-thermoacoustic systems exhibit gradual, abrupt and canard explosions due to changes in the response between the subsystems. The subsystems include hydrodynamics, acoustic field, and heat release rate fluctuations. Any system parameter that significantly influences the response between the subsystems can be varied as an additional parameter to observe the change in the nature of the bifurcation. For instance, Etikyala and Sujith (2017) observed that the nature of the bifurcation changes from supercritical to subcritical as an additional parameter is varied in a laminar thermoacoustic system, a Rijke tube. Here, the heater power of the Rijke tube is varied as the primary control parameter and the mass flow rate of the air is changed as an additional parameter. Similarly, in turbulent combustors, one can vary the power of the combustor or the bluff body position to investigate the change in the nature of the bifurcations. However, an understanding of flow physics is relevant to obtain further insights into the abrupt transition in turbulent aero-thermoacoustic systems. Thus, a future study involving the visualization of the flow field using particle image velocimetry and high-speed chemiluminescence imaging of flame dynamics is required to observe the dynamics of the turbulent field as the nature of transition changes.

APPENDIX A

CANARD EXPLOSIONS AND GRADUAL TRANSITIONS

A.1 HOPF BIFURCATION: EMERGENCE OF LCO FROM THE SILENT STATE

A canard explosion is characterized by a sudden transition from a low-amplitude oscillatory state to a high-amplitude oscillatory state within an exponentially small range of the control parameter. Moreover, a low-amplitude oscillatory state emerges from a Hopf bifurcation (Brøns and Bar-Eli, 1991). However, practical combustors involve turbulent reactive flow. In turbulent systems, we notice that the stable operation is not really silent due to inherent turbulent fluctuations (Nair *et al.*, 2014). If one considers a mean-field description where the effect of turbulence is discounted, the bifurcation of the turbulent thermoacoustic system could be viewed as a transition from a fixed-point solution to a periodic solution— which is a Hopf bifurcation

Figure A.1 represents the states of low amplitude chaos during stable operation, intermittency, large amplitude bursting and limit cycle oscillations for the transition consisting of a canard explosion in a bluff body stabilized dump combustor. We present the time series and phase trajectory of the low amplitude chaos during stable operation in Fig. A.1(b). The operating conditions of the combustors correspond to an approximate Reynolds number of 3×10^4 where the flow is fully turbulent. The low amplitude chaos is due to this inherent turbulence of the combustors; thus, we observe that stable operations are not silent. With a further variation in the control parameter (ϕ), we observe the state of intermittency (refer to Fig. A.1c).

Upon further variation of ϕ , referring to Fig. A.1(d), we notice a state of large amplitude

bursting. During the state of bursting, we show the states corresponding to high amplitude limit cycles (LCO, $p' \approx 3000$ Pa), low amplitude LCO ($p' \approx 500$ Pa) and low amplitude chaos ($p' \approx 200$ Pa, Fig. A.1(d)). The observation from the states of intermittency and large amplitude bursting implies that a low-amplitude LCO is born out of low-amplitude chaos, and the transition is continuous but rapid in nature. During the bursting state, the existence of all the ranges of the amplitudes of LCOs, including low amplitude chaos, is possibly due to the fluctuation of the system parameter across the steep rise of the canard explosion. This argument regarding the fluctuation of the system parameter also corroborates the bursting behaviour in the results from the model, as illustrated in Section 5.2.1. Upon further slight variation in the control parameter (ϕ), the system exhibits a very high amplitude LCO ($p' \approx 6000$ Pa), indicating an underlying canard explosion (Fig. A.1e).

A.2 COMPARISON BETWEEN THE CANARD EXPLOSION AND THE GRADUAL TRANSITION

Figure A.2 represents the comparison between the canard explosion and a gradual transition in a turbulent thermoacoustic system. We present the bifurcation diagram for the experimental trial where the control parameter is varied in steps of 5 SLPM (Fig. A.2a). We observe that the amplitude of the system rapidly rises in a continuous manner for smaller changes in equivalence ratio at $\phi \approx 1.2$ (refer to the light blue patch in the Fig. A.2a). This observation implies a higher sensitivity of the amplitude of the system with the control parameter at the regime of canard explosion. The experimental observation of this canard explosion also matches with the results from the model, as shown in Fig. A.2(b).

To further examine the sensitivity of the system amplitude on the control parameter, we perform experiments to obtain a gradual transition to thermoacoustic instability in a bluff body stabilized combustor. The combustor is operated with the same operating conditions

(refer to Chapter 3) corresponding to the results of the canard explosion, except for the bluff body position from the dump plane and the fuel flow rate. The new distance of the bluff body from the dump plane is 30 mm, and the fuel flow rate is 46 SLPM. At this new operating condition, we obtain a gradual transition unlike canard explosion, as shown in Fig. A.2(c). Here, we notice that there is a gradual increase in the amplitude of the p'_{rms} as a function of ϕ (refer to the grey coloured patch in the Fig. A.2c). We also represent the model results obtained for a noisy gradual transition, shown in Fig. A.2(d), obtained by modifying the nonlinear coefficients ($\mu_2 = 1$, $\mu_4 = 0$, & $\mu_6 = 0$). Thus, we observe that for a canard explosion, the amplitude rise is much steeper than the gradual transition.

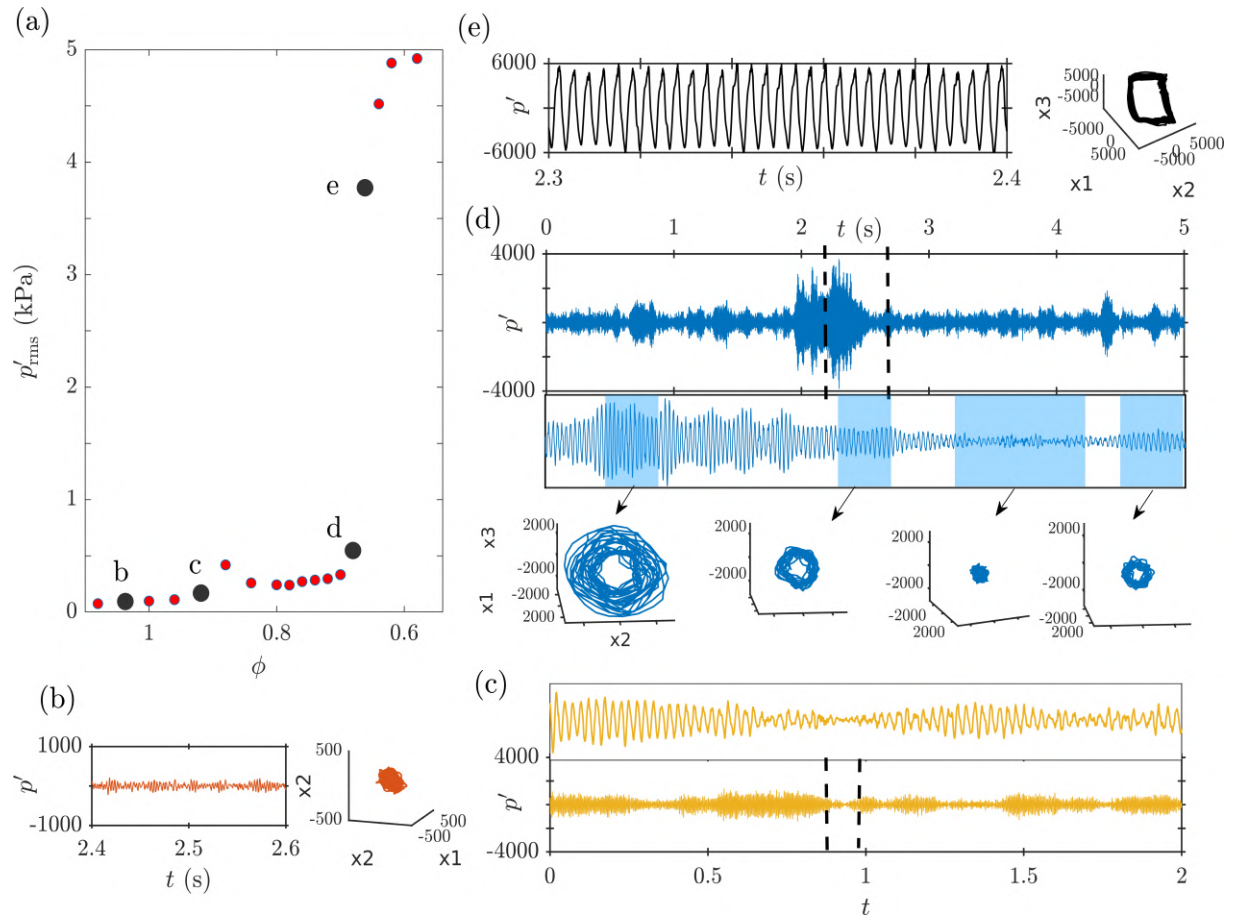


Figure A.1: Representation of the states of stable operation, intermittency, large amplitude bursting and limit cycle oscillations for the transition corresponding to canard explosion in a bluff body stabilized dump combustor. **(a)** Bifurcation diagram for the variation of p'_{rms} as a function of the equivalence ratio (ϕ). **(b)** Time series and phase space trajectory of low amplitude chaos during the stable operation. **(c)** Representation of the time series corresponding to the state of intermittency. **(d)** Time series corresponding to the state of bursting. We have also shown a zoomed-in region of the time series and phase space trajectories of certain epochs. Here, we present the epochs corresponding to high amplitude limit cycles (LCO, $p' \approx 3000Pa$), low amplitude LCO ($p' \approx 500 Pa$) and low amplitude chaos $p' \approx 200$. The observation implies that a low-amplitude LCO is born out of low-amplitude chaos, and the transition is continuous but rapid in nature. The existence of all the ranges of the amplitude of LCOs, including low amplitude chaos, is possibly due to the fluctuation of the system parameter across the steep rise of the canard explosion. **(e)** Time series corresponding to the state of LCO and the phase space trajectory.

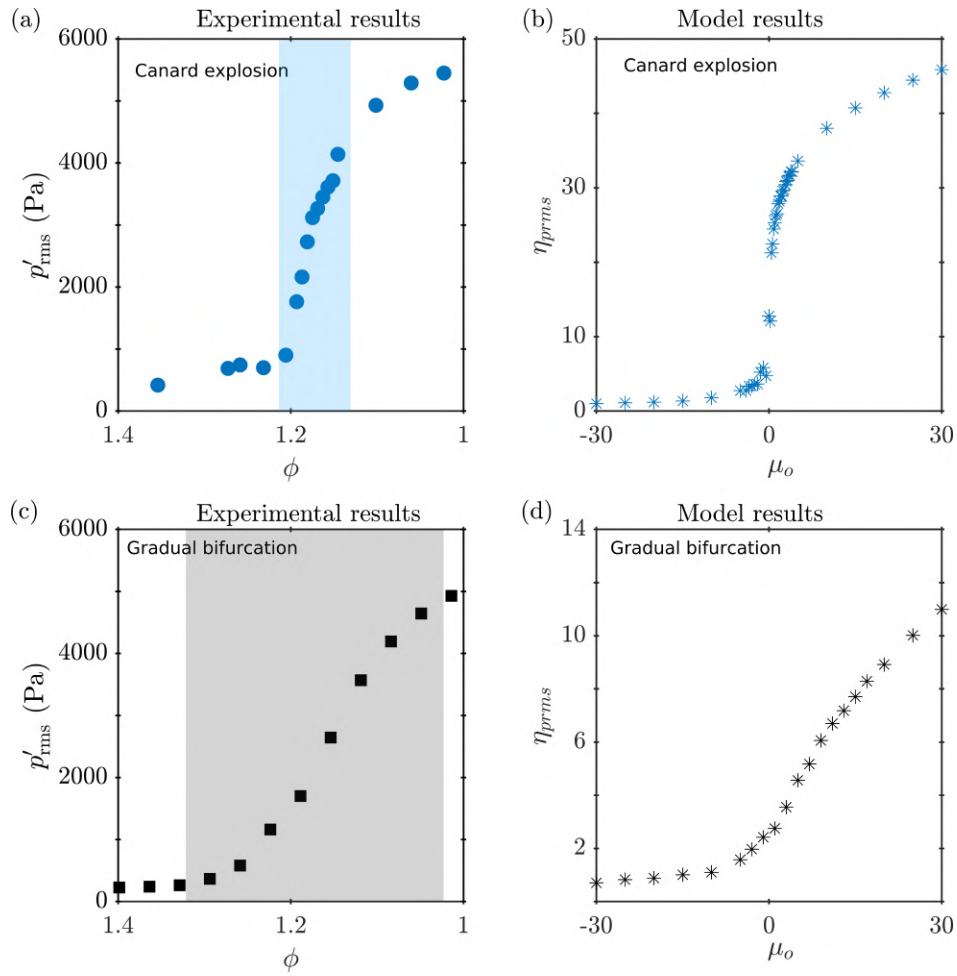


Figure A.2: **(a)** Representation of a sudden transition to high amplitude periodic oscillations via canard explosion in a bluff body stabilized dump combustor. We present the bifurcation diagram for the variation of the rms value of the acoustic pressure fluctuations (p'_{rms}) as a function of the equivalence ratio ϕ . The airflow rate, which governs the control parameter, varies in steps of 5 SLPM during the canard explosion regime. **(b)** The corresponding results of canard explosions obtained from the model. **(c)** Representation of the gradual bifurcation obtained in the bluff body stabilized combustor by modifying the fuel flow rate (46 SLPM) and the distance of the bluff body from the dump plane (30 mm). **(d)** The corresponding results of gradual bifurcation obtained from the model. We notice that for a canard explosion, the amplitude rise is much steeper than the gradual transition.

APPENDIX B

NATURAL MODES AND TIME SERIES OF AEROACOUSTIC SYSTEMS

B.1 EIGENMODES OF THE AEROACOUSTIC SYSTEM AND THE MODE SHAPES EXCITED DURING WHISTLING

We observe a switch in dominant frequencies from 461 to 411, 443 to 535, 535 to 411, and 445 to 470 Hz when Re crosses the values 5100, 7500, 8300, and 12000, respectively (refer to Fig. 6.1b). The duct modes play an important role in the frequency that is exhibited during whistling. In order to find the duct modes corresponding to the observed frequencies, we conducted experiments by exciting the system with a loudspeaker. We performed the experiment by fixing the amplitude while varying the frequency of the excitation from 50 Hz to 1000 Hz (refer to Fig. B.1a). We observed a large peak in the rms value of the acoustic pressure at 536 Hz and another peak with a relatively small amplitude around 436 Hz. The frequencies that we observe in the experiments during aeroacoustic instability are in the approximate range of 400 to 536 Hz.

Further, we also performed experiments to find the mode shapes corresponding to the whistling frequencies exhibited by the system (refer to Fig. B.1b) at different Re . We conducted experiments, mounting seven pressure transducers along the length of the pipe. We observe that these modes correspond to the second mode of the duct having an open-open boundary condition. Since the source of the sound, that is, the orifice, is a dipole source, only those modes which have velocity antinode near the location of the source are favoured (Hirschberg and Rienstra, 2004). Thus, we note that the shifts in whistling frequency observed in the experiments correspond to the lock-in between the same duct acoustic mode, but the hydrodynamic modes may be different (Nomoto and Culick, 1982; Huang and Weaver, 1991).

B.2 TIME SERIES OF ACOUSTIC PRESSURE DURING THE STATES OF LCO AND INTERMITTENCY

Figure B.2 represents the time series of the acoustic pressure fluctuation signal corresponding to the state of intermittency and LCO. The states of intermittency (B.2a & c) correspond to the minima of p'_{rms} curve (during the shift whistling frequency) shown in the bifurcation diagram of figure 6.1 in the main text, $Re \approx 7500$ & 8400 . During this state, we observe the bursts of periodic oscillations amidst the epochs of aperiodic oscillations. At $Re \approx 8100$, which corresponds to the maxima of p'_{rms} curve in figure 6.1 of the main text, we observe the state of LCO.

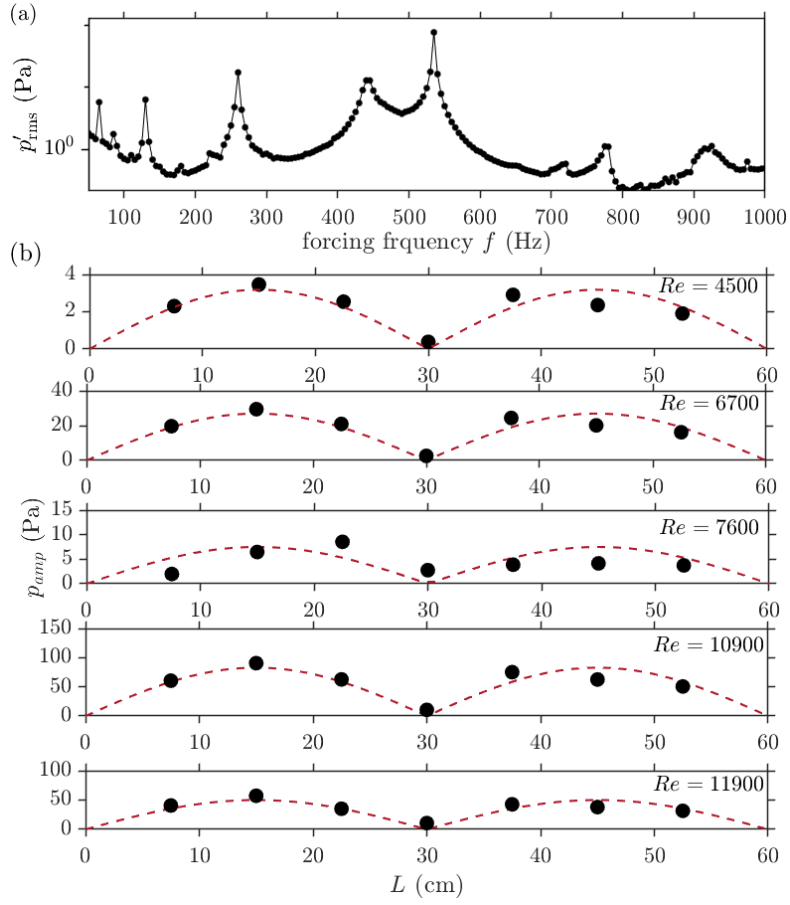


Figure B.1: (a) The variation of the p'_{rms} of acoustic pressure when the system is excited using a loudspeaker from 50 Hz to 1000 Hz. We observe a large peak at 536 Hz. (b) Acoustic mode shapes were obtained by locating the microphones along the duct length during the experiments. Mode shapes were obtained for the Re of 4500, 6700, 7600, 10900, and 11900. The ordinate represents the maximum amplitude of the signal from the amplitude spectrum (represented as the black dots), and the abscissa represents the position of the microphones along the length of the duct. The red curve in the plots indicates the theoretical mode shape for an open-open boundary condition of the duct, obtained using the equation $\hat{p}(x) \approx p_{max} |\sin(kx)|$. Where k is the wave number, and x is the distance from the duct inlet face. The expression for k is given as $k = n\pi/L$, where n is the mode number and L is the length of the duct. The frequencies corresponding to these mode shapes range from 400 to 535 Hz. We observe that these mode shapes correspond to the second mode of the duct having an open-open boundary condition.

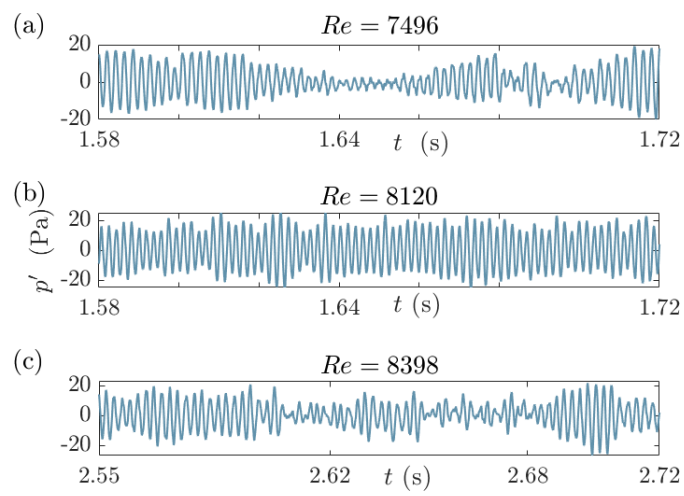


Figure B.2: Acoustic pressure fluctuations during (a) the state of intermittency at $Re \approx 7500$, (b) the state of LCO at $Re \approx 8100$, and (c) the state of intermittency at $Re \approx 8400$. According to the bifurcation diagram of figure 6.1 in the main text, the states of intermittency are found at the minima of p'_{rms} curve during the frequency shift. The maxima of p'_{rms} corresponds to the state of LCO.

APPENDIX C

RECURRENCE ANALYSIS FOR THE AEROACOUSTIC SYSTEM

C.1 RECURRENCE PLOTS FOR THE STATES OF LCO AND INTERMITTENCY

Figure C.1 represents the recurrence plots corresponding to the state of LCO ($Re \approx 4800, 7300, 8100 \& 12200$) and the state of intermittency ($Re \approx 7496 \& 8400$). For the state of LCO, we observe continuous diagonal lines which are equally spaced apart. The distance between the diagonal lines signifies the fundamental time period of the LCO. During the state of intermittency, we observe the black patches amidst the white region.

C.2 JOINT RECURRENCE PLOTS FOR THE STATES OF LCO AND INTERMITTENCY

Figure C.2 represents the joint recurrence plots corresponding to the state of LCO ($Re \approx 4800, 7300, 8100 \& 12200$) and the state of intermittency ($Re \approx 7500 \& 8400$). If the trajectories of the two subsystems u' and p' recur simultaneously, we observe a black dot in JRP. During the state of intermittency (Fig. C.2c & e), we observe that the black dots are sparsely spaced due to the absence of recurrence trajectories during the aperiodic epochs of u' and p' . This observation depicts the weak synchronisation strength between the signals of u' and p' . During the state of LCO, we observe an increase in the density of black dots and the appearance of short diagonal lines (Fig. C.2 a, b, d, and f). This observation of the diagonal lines in the JRP represents an increase in the synchronisation strength between u' and p' .

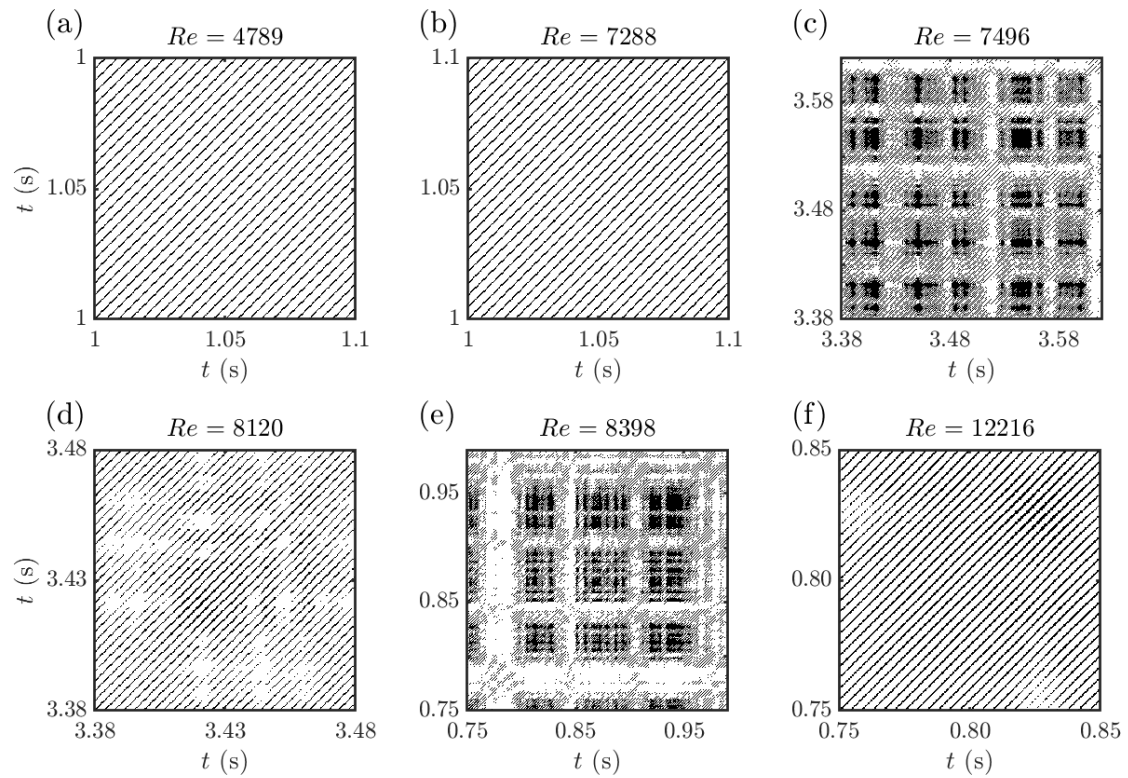


Figure C.1: Recurrence plots for the dynamical states observed with variation in Re . (a) LCO at $Re \approx 4800$. (b) LCO at $Re \approx 7300$. (c) Intermittency at $Re \approx 7500$. (d) LCO at $Re \approx 8100$. (e) Intermittency at $Re \approx 8400$. (f) LCO at $Re \approx 12200$. During the states of intermittency, we observe the black patches amidst the white region of RP. In contrast, during the state of LCO, we observe equally spaced continuous diagonal lines in the RP.

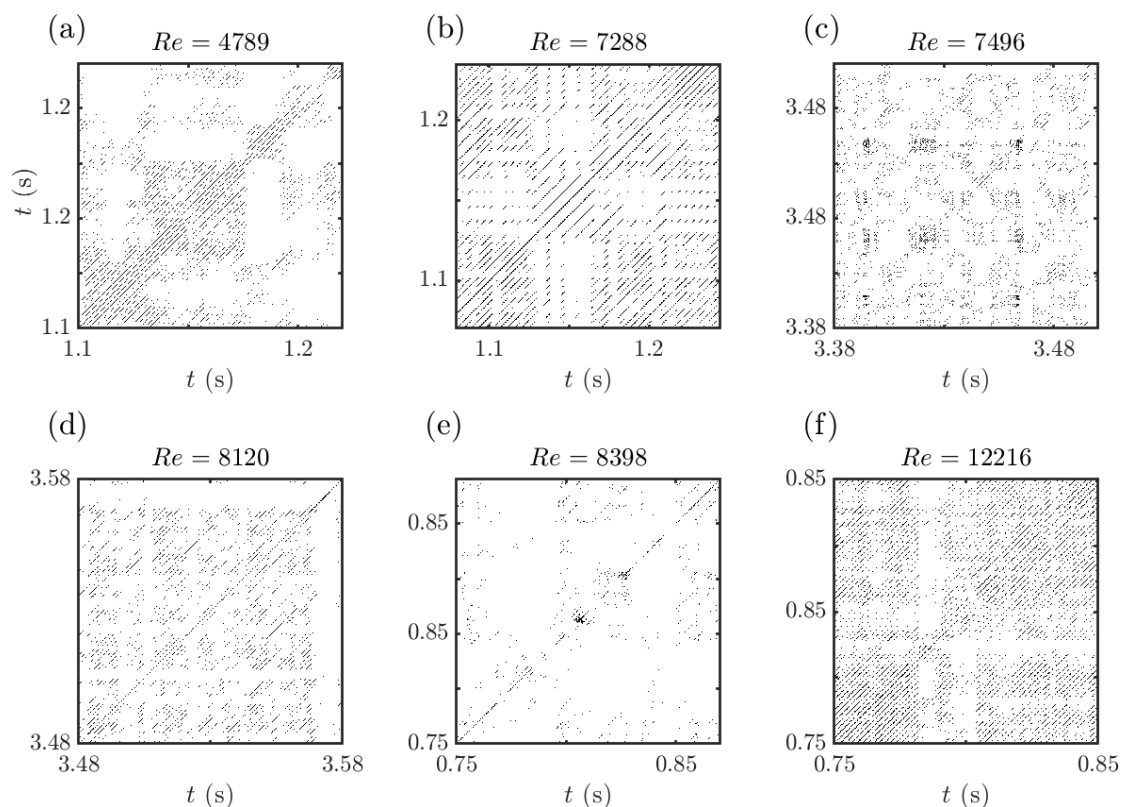


Figure C.2: Joint recurrence plots of the dynamical states that are observed with variation in Re . (a) LCO at $Re \approx 4800$. (b) LCO at $Re \approx 7300$. (c) Intermittency at $Re \approx 7500$. (d) LCO at $Re \approx 8100$. (e) Intermittency at $Re \approx 8400$. (f) LCO at $Re \approx 12200$. We observe diagonal lines in the JRP when there is higher synchronisation strength between the two periodic signals. We observe sparsely spaced black dots, interspersed with broken diagonal lines, in JRPs when the synchronisation strength is low during the states of intermittency.

APPENDIX D

SYNCHRONISATION ANALYSIS FOR THE AEROACOUSTIC SYSTEM

In the current aeroacoustic system, the acoustic field and the hydrodynamic field (Vortex shedding) are two different subsystems. Considering the following observations, we study the synchronisation between acoustic pressure and velocity fluctuations. Figure D.1 shows the time series obtained from the microphone and the hotwire during the aperiodic state at the higher bulk flow velocity. Here, we observe a broad band in the amplitude spectrum; however, there is a slight periodicity in the acoustic pressure fluctuations p' , which is observed as a peak in the amplitude spectrum. The spectrum of the velocity fluctuations is broad without having any dominant peaks (cf. Fig D.1b, c). Thus, we observe two different aperiodic signals.

The dominant peak in p' is attributed to the sound corresponding to the fundamental mode of the duct, generated due to the resonance of a range of flow disturbances in the entire duct. The magnitude of this sound is very low, and its generation is not due to the feedback mechanism between the acoustic and vortex shedding dynamics at the orifices Agarwal (1994a). Hence, the measured signal from the hot film probe is aperiodic with a broad amplitude spectrum due to the absence of periodic shedding of vortical structures. Thus, the difference in the nature of the measured signal from the microphone and the hot film probe implies that there is a negligible influence of the acoustic field over the hydrodynamic field Agarwal (1994b). Although these two system variables are strongly coupled during whistling, they are desynchronised during the aperiodic states. Thus, unlike velocity and displacement variables in a spring mass system, the velocity and acoustic fluctuations in an aeroacoustic system, in actuality, are not complementary. However, the velocity and acoustic pressure have synchronised periodic oscillations

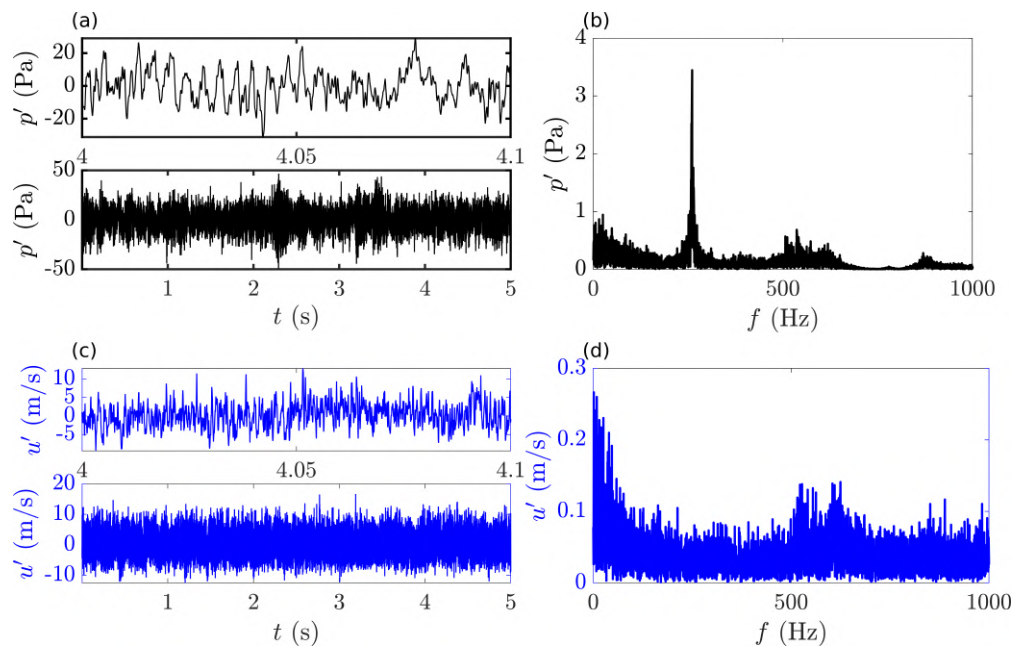


Figure D.1: The fluctuations in the signal from the microphone and hotwire measured during the experiments when the bulk flow velocity is 13.4 m/s based on the diameter of the orifice ($Re = 17800$). Here, (a) we observe that there is slight periodicity in the acoustic pressure fluctuation, which is observed (b) as a peak in the amplitude spectrum. In contrast, the spectrum of the velocity fluctuations is broad without having any sharp peaks.

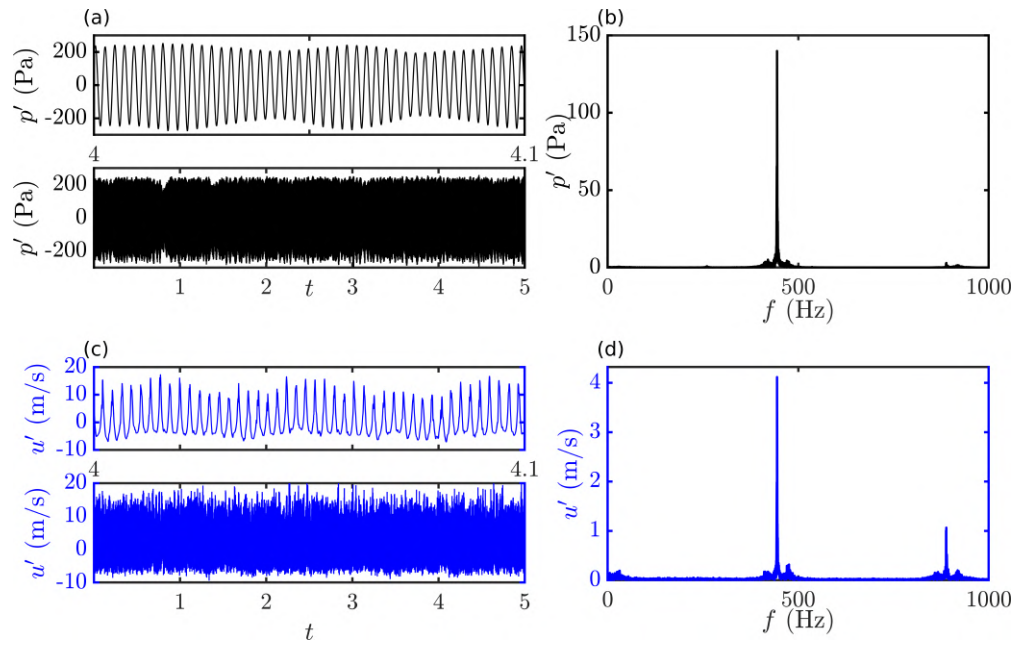


Figure D.2: The fluctuations in the signals from the microphone and hotwire measured during the experiments. We present the time series and their zoomed-in versions in the first column and the respective amplitude spectrum in the second column. The measurements are taken when the bulk flow velocity is 9.07 m/s based on the diameter of the orifice ($Re = 12077$).

during the state of the limit cycle oscillations (Fig. D.2).

BIBLIOGRAPHY

1. **A. Pavliotis, G.**, *Stochastic Processes and Applications: Diffusion Processes, the Fokker-Planck and Langevin Equations*. Springer, New York, 2014.
2. **Agarwal, N. K.** (1994a). The sound field in fully developed turbulent pipe flow due to internal flow separation, part I: Wall-pressure fluctuations. *Journal of Sound and Vibration*, **169**(1), 89–109.
3. **Agarwal, N. K.** (1994b). The sound field in fully developed turbulent pipe flow due to internal flow separation, part II: modal amplitude and cut-off frequencies. *Journal of Sound and Vibration*, **175**(1), 65–76.
4. **Ananthkrishnan, N., S. Deo, and F. E. Culick** (2005). Reduced-order modeling and dynamics of nonlinear acoustic waves in a combustion chamber. *Combust. Sci. and Tech.*, **177**(2), 221–248.
5. **Ananthkrishnan, N., K. Sudhakar, S. Sudershan, and A. Agarwal** (1998). Application of secondary bifurcations to large-amplitude limit cycles in mechanical systems. *J. Sound Vib.*, **215**(1), 183–188.
6. **Anderson, A. B. C.** (1952). Dependence of pfeifenton (pipe tone) frequency on pipe length, orifice diameter, and gas discharge pressure. *The Journal of the Acoustical Society of America*, **24**(6), 675–681.
7. **Anderson, W. E. and V. Yang**, *Liquid rocket engine combustion instability*. American Institute of Aeronautics and Astronautics, 1995.
8. **Anderson, W. E. and V. Yang**, *Liquid Rocket Engine Combustion Instability*. AIAA, Reston, 2012.
9. **Baillet, F., D. Durox, and R. Prud’Homme** (1992). Experimental and theoretical study of a premixed vibrating flame. *Combustion and flame*, **88**(2), 149–168.
10. **Balanov, A., N. Janson, D. Postnov, and O. Sosnovtseva**, *Synchronization: From Simple to Complex*. Springer Series in Synergetics. Springer, Heidelberg, Germany, 2009.
11. **Balasubramanian, K. and R. I. Sujith** (2008a). Non-normality and nonlinearity in combustion–acoustic interaction in diffusion flames. *Journal of Fluid Mechanics*, **594**, 29–57.
12. **Balasubramanian, K. and R. I. Sujith** (2008b). Thermoacoustic instability in a Rijke tube: Non-normality and nonlinearity. *Phys. Fluids*, **20**(4), 044103.

13. **Benzi, R., A. Sutera, and A. Vulpiani** (1981). The mechanism of stochastic resonance. *Journal of Physics A: mathematical and general*, **14**(11), L453.
14. **Bhavi, R. S., I. Pavithran, A. Roy, and R. I. Sujith** (2023). Abrupt transitions in turbulent thermoacoustic systems. *J. Sound Vib.*, **547**, 117478.
15. **Billon, A., V. Valeau, and A. Sakout** (2005). Two feedback paths for a jet-slot oscillator. *Journal of Fluids and Structures*, **21**(2), 121–132.
16. **Blasius, B., A. Huppert, and L. Stone** (1999). Complex dynamics and phase synchronization in spatially extended ecological systems. *Nature*, **399**(6734), 354–359.
17. **Blekhman, I. I., P. S. Landa, and M. G. Rosenblum** (1995). Synchronization and chaotization in interacting dynamical systems. *Applied Mechanics Reviews*, **48**, 733–752.
18. **Blevins, R. D.** (1985). The effect of sound on vortex shedding from cylinders. *Journal of Fluid Mechanics*, **161**, 217–237.
19. **Blomshield, F.**, Historical perspective of combustion instability in motors-case studies. *In 37th Joint Propulsion Conference and Exhibit*. 2001.
20. **Bloxside, G., A. Dowling, and P. Langhorne** (1988). Reheat buzz: an acoustically coupled combustion instability. part 2. theory. *Journal of fluid mechanics*, **193**, 445–473.
21. **Boccaletti, S., J. Kurths, G. Osipov, D. L. Valladares, and C. S. Zhou** (2002). The synchronization of chaotic systems. *Physics Reports*, **366**(1-2), 1–101.
22. **Bonciolini, G., D. Ebi, E. Boujo, and N. Noiray**, Subcritical thermoacoustic bifurcation in turbulent combustors: Effects of inertia. *In 26th International Colloquium on the Dynamics of Explosions and Reactive Systems (ICDERS 2017), Boston , USA*. 2017.
23. **Bonciolini, G., A. Faure-Beaulieu, C. Bourquard, and N. Noiray** (2021). Low order modelling of thermoacoustic instabilities and intermittency: Flame response delay and nonlinearity. *Combust. Flame*, **226**, 396–411.
24. **Börgers, C.**, *An introduction to modeling neuronal dynamics*, volume 66. Springer, 2017.
25. **Boujo, E., C. Bourquard, Y. Xiong, and N. Noiray** (2020). Processing time-series of randomly forced self-oscillators: the example of beer bottle whistling. *Journal of Sound and Vibration*, **464**, 114–981.
26. **Bourquard, C., A. Faure-Beaulieu, and N. Noiray** (2021). Whistling of deep cavities subject to turbulent grazing flow: intermittently unstable aeroacoustic feedback. *Journal of Fluid Mechanics*, **909**, A19.

27. **Brøns, M.** and **K. Bar-Eli** (1991). Canard explosion and excitation in a model of the Belousov-Zhabotinsky reaction. *J. Phys. Chem.*, **95**(22), 8706–8713.
28. **Bruggeman, J., A. Wijnands,** and **J. Gorter**, Self sustained low frequency resonance in low-Mach-number gas flow through pipe-lines with side-branch cavities: a semi-empirical model. *In 10th Aeroacoustics Conference*. 1986.
29. **Burnley, V.** and **F. Culick** (2000). Influence of random excitations on acoustic instabilities in combustion chambers. *AIAA J.*, **38**(8), 1403–1410.
30. **Byrne, R.**, Longitudinal pressure oscillations in ramjet combustors. *In 19th Joint Propulsion Conference*. 1983.
31. **Campa, G.** and **M. P. Juniper**, Obtaining bifurcation diagrams with a thermoacoustic network model. *In Turbo Expo: Power for Land, Sea, and Air*, volume 44687. American Society of Mechanical Engineers, 2012.
32. **Candel, S.** (2002). Combustion dynamics and control: progress and challenges. *Proceedings of the combustion institute*, **29**(1), 1–28.
33. **Candel, S., D. Durox, S. Ducruix, A.-L. Birbaud, N. Noiray,** and **T. Schuller** (2009). Flame dynamics and combustion noise: Progress and challenges. *Int. J. Aeroacoustics*, **8**(1), 1–56.
34. **Chanaud, R. C.** and **A. Powell** (1965). Some experiments concerning the hole and ring tone. *The Journal of the Acoustical Society of America*, **37**(5), 902–911.
35. **Chen, T. H., L. P. Goss, D. D. Trump,** and **W. J. Schmoll** (1990). Studies of a turbulent premixed flame using CARS-LDV diagnostics. *J. Propuls. Power*, **6**(2), 106–114.
36. **Clavin, P., J. Kim,** and **F. Williams** (1994). Turbulence-induced noise effects on high-frequency combustion instabilities. *Combust. Sci. and Tech.*, **96**(1-3), 61–84.
37. **Coffey, W. T.** and **Y. P. Kalmykov**, *The Langevin equation: With Applications to Stochastic Problems in Physics, Chemistry and Electrical Engineering*. World Scientific, 2012, 3 edition.
38. **Crocco, L.** and **S.-I. Cheng** (1956). Theory of combustion instability in liquid propellant rocket motors. Technical report, Princeton Univ Nj.
39. **Culick, F. E.** and **P. Kuentzmann** (2006). Unsteady motions in combustion chambers for propulsion systems. Technical report, NATO Research and Technology Organization Neuilly-Sur-Seine (France).
40. **Culick, F. E.** and **V. Yang** (1995). Overview of combustion instabilities in liquid-propellant rocket engines. *Progress in Astronautics and Aeronautics*, **169**, 3–38.

41. **Culick, F. E. C.**, Combustion instabilities in liquid-fuelled propulsion systems. *In AGARD Conference proceedings*, volume 450. 1988.
42. **Davis, D.** (1981). Coaxial dump ramjet combustor combustion instabilities. part I. Parametric Test Data. Technical report, AIR FORCE WRIGHT AERONAUTICAL LABS WRIGHT-PATTERSON AFB OH.
43. **Deng, B.** (2004). Food chain chaos with canard explosion. *Chaos*, **14**(4), 1083–1092.
44. **Desroches, M., T. J. Kaper, and M. Krupa** (2013). Mixed-mode bursting oscillations: Dynamics created by a slow passage through spike-adding canard explosion in a square-wave burster. *Chaos*, **23**(4).
45. **Diener, M.** (1984). The canard unchained or how fast/slow dynamical systems bifurcate. *Math. Intell.*, **6**(3), 38–49.
46. **Douglass, J. K., L. Wilkens, E. Pantazelou, and F. Moss** (1993). Noise enhancement of information transfer in crayfish mechanoreceptors by stochastic resonance. *Nature*, **365**(6444), 337–340.
47. **Dowling, A. P.** (1997). Nonlinear self-excited oscillations of a ducted flame. *Journal of Fluid Mechanics*, **346**, 271–290.
48. **Dowling, A. P. and J. E. F. Williams**, *Sound and sources of sound*. Ellis Horwood, 1983.
49. **Dranovsky, M. L.**, *Combustion instabilities in liquid rocket engines: testing and development practices in Russia*. American Institute of Aeronautics and Astronautics, 2007.
50. **Ducruix, S., D. Durox, and S. Candel** (2000). Theoretical and experimental determinations of the transfer function of a laminar premixed flame. *Proceedings of the combustion institute*, **28**(1), 765–773.
51. **Dunlap, R. and R. S. Brown** (1981). Exploratory experiments on acoustic oscillations driven by periodic vortex shedding. *AIAA Journal*, **19**(3), 408–409.
52. **Eckhaus, W.**, Relaxation oscillations including a standard chase on french ducks. *In F. Verhulst* (ed.), *Asymptotic Analysis II. Lecture notes in Math.*, volume 985. Springer Berlin Heidelberg, Berlin, Heidelberg, 1983. ISBN 978-3-540-39612-3.
53. **Eckmann, J. P., S. O. Kamphorst, and D. Ruelle** (2017). Recurrence plots of dynamical systems. *Journal of Fluid Mechanics*, **827**, 664–693.
54. **Etikyala, S. and R. I. Sujith** (2017). Change of criticality in a prototypical thermoacoustic system. *Chaos*, **27**(2), 023106.
55. **Fabre, B., J. Gilbert, A. Hirschberg, and X. Pelorson** (2012). Aeroacoustics of musical

- instruments. *Annual Review of Fluid Mechanics*, **44**(1), 1–25.
56. **Ffowcs, J. E.** and **B. C. Zhao** (1989). The active control of vortex shedding. *Journal of Fluids and Structures*, **3**, 115–122.
 57. **Flandro, G.** and **H. Jacobs**, Vortex generated sound in cavities. *In Aeroacoustics Conference*. 1973.
 58. **Fleifil, M., A. M. Annaswamy, Z. Ghoneim, and A. F. Ghoniem** (1996). Response of a laminar premixed flame to flow oscillations: A kinematic model and thermoacoustic instability results. *Combust. Flame*, **106**(4), 487–510.
 59. **Fraser, A. M.** and **H. L. Swinney** (1986). Independent coordinates for strange attractors from mutual information. *Physical Review A*, **33**(2), 1134.
 60. **George, N. B., V. R. Unni, M. Raghunathan, and R. I. Sujith** (2018). Spatiotemporal dynamics during the transition to thermoacoustic instability: effect of varying turbulence intensities. *International Journal of Spray and Combustion Dynamics*, **10**(4), 337–350.
 61. **Glass, L.** (2001). Synchronization and rhythmic processes in physiology. *Nature*, **410**(6825), 277–284.
 62. **Godavarthi, V., P. Kasthuri, S. Mondal, R. I. Sujith, N. Marwan, and J. Kurths** (2020). Synchronization transition from chaos to limit cycle oscillations when a locally coupled chaotic oscillator grid is coupled globally to another chaotic oscillator. *Chaos: An Interdisciplinary Journal of Nonlinear Science*, **30**(3), 033121.
 63. **Godavarthi, V., S. A. Pawar, V. R. Unni, R. I. Sujith, N. Marwan, and J. Kurths** (2018). Coupled interaction between unsteady flame dynamics and acoustic field in a turbulent combustor. *Chaos: An Interdisciplinary Journal of Nonlinear Science*, **28**(11), 113111.
 64. **Gopalakrishnan, E.** and **R. I. Sujith** (2014). Influence of system parameters on the hysteresis characteristics of a horizontal Rijke tube. *Int. J. Spray Combust. Dyn.*, **6**(3), 293–316.
 65. **Gopalakrishnan, E., J. Tony, E. Sreelekha, and R. I. Sujith** (2016). Stochastic bifurcations in a prototypical thermoacoustic system. *Phys. Rev. E*, **94**(2), 022203.
 66. **Goswami, B., N. Marwan, G. Feulner, and J. Kurths** (2013). How do global temperature drivers influence each other? *The European Physical Journal Special Topics*, **222**(3), 861–873.
 67. **Gotoda, H., H. Nikimoto, T. Miyano, and S. Tachibana** (2011). Dynamic properties of combustion instability in a lean premixed gas-turbine combustor. *Chaos*, **21**(1), 013124.
 68. **Gotoda, H., Y. Shinoda, M. Kobayashi, Y. Okuno, and S. Tachibana** (2014). Detection

and control of combustion instability based on the concept of dynamical system theory. *Phys. Rev. E*, **89**(2), 022910.

69. **Griffin, O. M.** and **M. S. Hall** (1991). Review—Vortex Shedding Lock-on and Flow Control in Bluff Body Wakes. *Journal of Fluids Engineering*, **113**(4), 526–537.
70. **Griffin, O. M.** and **S. E. Ramberg** (1974). The vortex-street wakes of vibrating cylinders. *Journal of Fluid Mechanics*, **66**(3), 553–576.
71. **Guan, Y., V. Gupta,** and **L. K. Li** (2020). Intermittency route to self-excited chaotic thermoacoustic oscillations. *J. Fluid Mech.*, **894**.
72. **Gunnoo, H., N. Abcha,** and **A. Ezersky** (2016). Frequency lock-in and phase synchronization of vortex shedding behind circular cylinder due to surface waves. *Physics Letters A*, **380**(7-8), 863–868.
73. **Gupta, V., A. Saurabh, C. O. Paschereit,** and **L. Kabiraj** (2017). Numerical results on noise-induced dynamics in the subthreshold regime for thermoacoustic systems. *Journal of Sound and Vibration*, **390**, 55–66.
74. **Han, X.** and **Q. Bi** (2012). Slow passage through canard explosion and mixed-mode oscillations in the forced Van der Pol's equation. *Nonlinear Dyn.*, **68**, 275–283.
75. **Heagy, J. F., T. L. Carroll,** and **L. M. Pecora** (1994). Synchronous chaos in coupled oscillator systems. *Physical Review E*, **50**(3), 1874.
76. **Higgins, B.** (1802). On the sound produced by a current of hydrogen gas passing through a tube. *Journal of natural philosophy, chemistry and the arts*, **1**(129-131), 2.
77. **Hirschberg, A.** and **S. W. Rienstra**, *An Introduction to Aeroacoustics*. Eindhoven University of Technology, 2004.
78. **Hong, J. G., K. C. Oh, U. D. Lee,** and **H. D. Shin** (2008). Generation of low-frequency alternative flame behaviors in a lean premixed combustor. *Energy Fuels*, **22**(5), 3016–3021.
79. **Hourigan, K., M. C. Welsh, M. C. Thompson,** and **A. N. Stokes** (1990). Aerodynamic sources of acoustic resonance in a duct with baffles. *Journal of Fluids and Structures*, **4**(4), 345–370.
80. **Howe, M. S.** (1975). Contributions to the theory of aerodynamic sound, with application to excess jet noise and the theory of the flute. *Journal of Fluid Mechanics*, **71**(4), 625–673.
81. **Howe, M. S.** (1980). The dissipation of sound at an edge. *Journal of Sound and Vibration*, **70**(3), 407–411.

82. **Huang, X. Y.** and **D. S. Weaver** (1991). On the active control of shear layer oscillations across a cavity in the presence of pipeline acoustic resonance. *Journal of Fluids and Structures*, **5**(2), 207–219.
83. **Huang, Y.** (2015). *Advanced methods for validating combustion instability predictions using pressure measurements*. Ph.D. thesis, Purdue University.
84. **Huygens, C.** (1665). Attachment to a letter to constantyn huygens, his father in: O.c. 5, letter no. 1335 of 26 February,, 243–244.
85. **Izhikevich, E. M.** (2000). Neural excitability, spiking and bursting. *Int. J. Bifurc. Chaos*, **10**(06), 1171–1266.
86. **Jahnke, C. C.** and **F. E. Culick** (1994). Application of dynamical systems theory to nonlinear combustion instabilities. *Journal of propulsion and power*, **10**(4), 508–517.
87. **Juniper, M. P.** (2011). Triggering in the horizontal rijke tube: non-normality, transient growth and bypass transition. *Journal of Fluid Mechanics*, **667**, 272–308.
88. **Juniper, M. P.** (2012). Triggering in thermoacoustics. *Int. J. Spray Combust. Dyn.*, **4**(3), 217–237.
89. **Kabiraj, L.** (2012). *Intermittency and route to chaos in thermoacoustic oscillations*. Ph.D. thesis, Indian Institute of Technology, Madras.
90. **Kabiraj, L., A. Saurabh, N. Karimi, A. Sailor, E. Mastorakos, A. P. Dowling, and C. O. Paschereit** (2015a). Chaos in an imperfectly premixed model combustor. *Chaos*, **25**(2), 023101.
91. **Kabiraj, L., A. Saurabh, H. Nawroth, and C. O. Paschereit** (2015b). Recurrence analysis of combustion noise. *AIAA Journal*, **53**(5), 1199–1210.
92. **Kabiraj, L., A. Saurabh, P. Wahi, and R. I. Sujith** (2012a). Route to chaos for combustion instability in ducted laminar premixed flames. *Chaos: An Interdisciplinary Journal of Nonlinear Science*, **22**(2).
93. **Kabiraj, L., R. Steinert, A. Saurabh, and C. O. Paschereit** (2015c). Coherence resonance in a thermoacoustic system. *Physical Review E*, **92**(4), 042909.
94. **Kabiraj, L.** and **R. I. Sujith** (2012). Nonlinear self-excited thermoacoustic oscillations: intermittency and flame blowout. *Journal of Fluid Mechanics*, **713**, 376–397.
95. **Kabiraj, L., R. I. Sujith, and P. Wahi** (2012b). Bifurcations of self-excited ducted laminar premixed flames. *J. Eng. Gas Turbines Power.*, **134**(3).
96. **Kabiraj, L., N. Vishnoi, and A. Saurabh** (2020). A review on noise-induced dynamics of thermoacoustic systems. *Dynamics and Control of Energy Systems*, 265–281.

97. **Kamin, M., J. Mathew, and R. I. Sujith** (2019). A numerical study of an acoustic–hydrodynamic system exhibiting an intermittent prelude to instability. *International Journal of Aeroacoustics*, **18**(4-5), 536–553.
98. **Karthik, B., S. Chakravarthy, and R. I. Sujith**, The effect of orifice thickness on the vortex-acoustic interaction in a duct. *In 7th AIAA/CEAS Aeroacoustics Conference and Exhibit*. 2001.
99. **Karthik, B., S. R. Chakravarthy, and R. I. Sujith** (2008). Mechanism of pipe-tone excitation by flow through an orifice in a duct. *International Journal of Aeroacoustics*, **7**(3-4), 321–347.
100. **Kasthuri, P., S. A. Pawar, R. Gejji, W. Anderson, and R. I. Sujith** (2022). Coupled interaction between acoustics and unsteady flame dynamics during the transition to thermoacoustic instability in a multi-element rocket combustor. *Combustion and Flame*, **240**, 112047.
101. **Kasthuri, P., V. R. Unni, and R. I. Sujith** (2019). Bursting and mixed mode oscillations during the transition to limit cycle oscillations in a matrix burner. *Chaos*, **29**(4), 043117.
102. **Keanni, R., K. Yu, and J. Daily**, Evidence of a strange attractor in ramjet combustion. *In 27th Aerospace Sciences Meeting*. 1989.
103. **Kennel, M. B., R. Brown, and H. D. I. Abarbanel** (1992). Determining embedding dimension for phase-space reconstruction using a geometrical construction. *Physical Review A*, **45**(6), 3403.
104. **Kheirkhah, S., J. M. Cirtwill, P. Saini, K. Venkatesan, and A. M. Steinberg** (2017). Dynamics and mechanisms of pressure, heat release rate, and fuel spray coupling during intermittent thermoacoustic oscillations in a model aeronautical combustor at elevated pressure. *Combust. Flame*, **185**, 319–334.
105. **Knoop, P., F. Culick, and E. Zukoski** (1997). Extension of the stability of motions in a combustion chamber by nonlinear active control based on hysteresis. *Combustion science and technology*, **123**(1-6), 363–376.
106. **Komarek, T. and W. Polifke** (2010). Impact of swirl fluctuations on the flame response of a perfectly premixed swirl burner. *Journal of Engineering for Gas Turbines and Power*, **132**(6), 061503.
107. **Koo, J.** (2011). *Adjoint sensitivity analysis of the intercontinental impacts of aviation emissions on air quality and health*. Ph.D. thesis, Massachusetts Institute of Technology.
108. **Krebs, W., G. Walz, and S. Hoffmann**, Thermoacoustic analysis of annular combustor. *In 5th AIAA/CEAS Aeroacoustics Conference and Exhibit*. 1999.
109. **Kriesels, P. C., M. C. A. M. Peters, A. Hirschberg, A. P. J. Wijnands, A. Iafrati,**

- G. Riccardi, R. Piva, and J. C. Bruggeman** (1995). High amplitude vortex-induced pulsations in a gas transport system. *Journal of Sound and Vibration*, **184**(2), 343–368.
110. **Krupa, M. and P. Szmolyan** (2001). Relaxation oscillation and canard explosion. *J. Differ. Equ.*, **174**(2), 312–368.
111. **Krylov, N. M. and N. N. Bogoliubov**, *Introduction to Non-Linear Mechanics. (AM-11)*. Princeton University Press, Princeton, 2016.
112. **Külshammer, C. and H. Büchner** (2002). Combustion dynamics of turbulent swirling flames. *Combustion and flame*, **131**(1-2), 70–84.
113. **Kumar, P., D. K. Verma, P. Parmananda, and S. Boccaletti** (2015). Experimental evidence of explosive synchronization in mercury beating-heart oscillators. *Phys. Rev. E*, **91**(6), 062909.
114. **Lakshmanan, M. and D. V. Senthilkumar**, *Dynamics of nonlinear time-delay systems*. Springer Science & Business Media, 2011.
115. **Leconte, J.** (1858). On the influence of musical sounds on the flame of a jet of coal-gas. *The London, Edinburgh, and Dublin Philosophical Magazine and Journal of Science*, **15**(99), 235–239.
116. **Lee, M., K. T. Kim, V. Gupta, and L. K. Li** (2021). System identification and early warning detection of thermoacoustic oscillations in a turbulent combustor using its noise-induced dynamics. *Proc. Combust. Inst.*, **38**(4), 6025–6033.
117. **Lefebvre, A. H. and D. R. Ballal**, *Gas turbine combustion: alternative fuels and emissions*. CRC press, 2010.
118. **Lei, S. and A. Turan** (2010). Nonlinear/chaotic modeling and control of combustion instabilities. *International Journal of Bifurcation and Chaos*, **20**(04), 1245–1254.
119. **Levine, J. N. and J. D. Baum** (1983). A numerical study of nonlinear instability phenomena in solid rocketmotors. *AIAA Journal*, **21**(4), 557–564.
120. **Li, X., D. Zhao, and B. Shi** (2019). Coherence resonance and stochastic bifurcation behaviors of simplified standing-wave thermoacoustic systems. *The Journal of the Acoustical Society of America*, **145**(2), 692–702.
121. **Li, X., D. Zhao, and X. Yang** (2017). Experimental and theoretical bifurcation study of a nonlinear standing-wave thermoacoustic system. *Energy*, **135**, 553–562.
122. **Lieuwen, T. C.** (2002). Experimental investigation of limit-cycle oscillations in an unstable gas turbine combustor. *J. Propuls. Power*, **18**(1), 61–67.
123. **Lieuwen, T. C.**, *Unsteady Combustor Physics*. Cambridge University Press, Cambridge,

2021, 2 edition.

124. **Lieuwen, T. C.** and **V. Yang**, *Combustion Instabilities in Gas Turbine Engines: Operational Experience, Fundamental Mechanisms, and Modeling*. Progress in Aeronautics and Astronautics. American Institute of Aeronautics and Astronautics, Reston, Virginia, 2005.
125. **Liou, T.-M., W.-Y. Lien**, and **P.-W. Hwang** (1997). Flammability limits and probability density functions in simulated solid-fuel ramjet combustors. *Journal of Propulsion and Power*, **13**(5), 643–650.
126. **Lores, M. E.** and **B. T. Zinn** (1973). Nonlinear longitudinal combustion instability in rocket motors. *Combust. Sci. and Tech.*, **7**(6), 245–256.
127. **Macquisten, M.** (1995). Combustion oscillations in a twin-stream afterburner. *Journal of sound and vibration*, **188**(4), 545–560.
128. **Mariappan, S., P. Schmid**, and **R. I. Sujith**, Role of transient growth in subcritical transition to thermoacoustic instability in a horizontal rijke tube. *In 16th AIAA/CEAS Aeroacoustics Conference*. 2010.
129. **Marino, F., M. Ciszak, S. F. Abdalah, K. Al-Naimee, R. Meucci**, and **F. T. Arecchi** (2011). Mixed-mode oscillations via canard explosions in light-emitting diodes with optoelectronic feedback. *Phys. Rev. E*, **84**(4), 047201.
130. **Marwan, N.** (2011). How to avoid potential pitfalls in recurrence plot based data analysis. *International Journal of Bifurcation and Chaos*, **21**(04), 1003–1017.
131. **Marwan, N.** and **J. Kurths** (2002). Nonlinear analysis of bivariate data with cross recurrence plots. *Physics Letters A*, **302**(5-6), 299–307.
132. **Marwan, N., M. C. R., M. Thiel**, and **J. Kurths** (2007). Recurrence plots for the analysis of complex systems. *Physics Reports*, **438**(5-6), 237–329.
133. **Matsuura, K.** and **M. Nakano** (2011). Direct computation of a hole-tone feedback system at very low Mach numbers. *Journal of Fluid Science and Technology*, **6**(4), 548–561.
134. **Matveev, K. I.** (2003). *Thermoacoustic instabilities in the Rijke tube: Experiments and modeling*. Ph.D. thesis, California Institute of Technology, Pasadena, California.
135. **Matveev, K. I.** and **F. Culick** (2003). A model for combustion instability involving vortex shedding. *Combustion Science and Technology*, **175**(6), 1059–1083.
136. **Mawardi, O.** (1956). Aero-thermoacoustics (the generation of sound by turbulence and by heat processes). *Reports on Progress in Physics*, **19**(1), 156.

137. **McManus, K., T. Poinso**t, and **S. M. Candel** (1993). A review of active control of combustion instabilities. *Prog. Energy Combust. Sci.*, **19**(1), 1–29.
138. **Mettenleiter, M., E. Haile**, and **S. Candel** (2000). Adaptive control of aeroacoustic instabilities. *Journal of Sound and Vibration*, **230**(4), 761–789.
139. **Minorsky, N.**, *Nonlinear Oscillations*. D. Van Nostrand company, Inc., Princeton, New Jersey, 1962.
140. **Moeck, J. P., M. Bothien, S. Schimek, A. Lacarelle**, and **C. Paschereit**, Subcritical thermoacoustic instabilities in a premixed combustor. *In 14th AIAA/CEAS aeroacoustics conference (29th AIAA aeroacoustics conference), Vancouver, British Columbia, Canada*. 2008.
141. **Moehlis, J.** (2006). Canards for a reduction of the Hodgkin-Huxley equations. *J. Math. Biol.*, **52**, 141–153.
142. **Mohammed Al-Muslim, H., N. Ibrahim Al-Nasri**, and **M. Y. Al-Hashem** (2013). The danger of piping failure due to acoustic-induced fatigue in infrequent operations: Two case studies. *Journal of Pressure Vessel Technology*, **135**(6).
143. **Mondal, S., V. R. Unni**, and **R. I. Sujith** (2017). Onset of thermoacoustic instability in turbulent combustors: an emergence of synchronized periodicity through formation of chimera-like states. *J. Fluid Mech.*, **811**, 659–681.
144. **Mukherjee, N., M. Heckl, A. Bigongiari, R. Vishnu, P. Samadhan**, and **R. I. Sujith**, Nonlinear dynamics of a laminar V-flame in a combustor. *In 22nd Int. Congr. Sound Vib. ICSV, Florence, Italy*. 2015.
145. **Nagarajan, B., N. Baraiya**, and **S. Chakravarthy** (2019). Effect of inlet flow turbulence on the combustion instability in a premixed backward-facing step combustor. *Proceedings of the Combustion Institute*, **37**(4), 5189–5196.
146. **Nair, V.** and **R. I. Sujith** (2014). Multifractality in combustion noise: Predicting an impending combustion instability. *J. Fluid Mech.*, **747**, 635–655.
147. **Nair, V.** and **R. I. Sujith** (2015). A reduced-order model for the onset of combustion instability: Physical mechanisms for intermittency and precursors. *Proc. Combust. Inst.*, **35**(3), 3193–3200.
148. **Nair, V.** and **R. I. Sujith** (2016). Precursors to self-sustained oscillations in aeroacoustic systems. *International Journal of Aeroacoustics*, **15**(3), 312–323.
149. **Nair, V., G. Thampi, S. Karuppusamy, S. Gopalan**, and **R. I. Sujith** (2013). Loss of chaos in combustion noise as a precursor of impending combustion instability. *Int. J. Spray Combust. Dyn.*, **5**(4), 273–290.

150. **Nair, V., G. Thampi, and R. I. Sujith** (2014). Intermittency route to thermoacoustic instability in turbulent combustors. *J. Fluid Mech.*, **756**, 470–487.
151. **Nakiboğlu, G. and A. Hirschberg** (2012). Aeroacoustic power generated by multiple compact axisymmetric cavities: effect of hydrodynamic interference on the sound production. *Physics of Fluids*, **24**(6), 067101.
152. **Nicoud, F. and K. Wieczorek** (2009). About the zero Mach number assumption in the calculation of thermoacoustic instabilities. *Int. J. Spray Combust. Dyn.*, **1**(1), 67–111.
153. **Noiray, N.** (2017). Linear growth rate estimation from dynamics and statistics of acoustic signal envelope in turbulent combustors. *J. Eng. Gas Turbines Power.*, **139**(4).
154. **Noiray, N. and A. Denisov** (2017). A method to identify thermoacoustic growth rates in combustion chambers from dynamic pressure time series. *Proc. Combust. Inst.*, **36**(3), 3843–3850.
155. **Noiray, N. and B. Schuermans** (2013). Deterministic quantities characterizing noise driven Hopf bifurcations in gas turbine combustors. *Int. J. Non-Linear Mech.*, **50**, 152–163.
156. **Nomoto, H. and F. E. C. Culick** (1982). An experimental investigation of pure tone generation by vortex shedding in a duct. *Journal of Sound and Vibration*, **84**(2), 247–252.
157. **Oefelein, J. C. and V. Yang** (1993). Comprehensive review of liquid-propellant combustion instabilities in f-1 engines. *Journal of Propulsion and Power*, **9**(5), 657–677.
158. **Ouyang, H., W. Liu, and M. Sun** (2016). Parametric study of combustion oscillation in a single-side expansion scramjet combustor. *Acta Astronautica*, **127**, 603–613.
159. **Ouyang, H., W. Liu, and M. Sun** (2017). The influence of cavity parameters on the combustion oscillation in a single-side expansion scramjet combustor. *Acta Astronautica*, **137**, 52–59.
160. **Paschereit, C. O., B. Schuermans, W. Polifke, and O. Mattson** (2002). Measurement of transfer matrices and source terms of premixed flames. *J. Eng. Gas Turbines Power*, **124**(2), 239–247.
161. **Pavithran, I., P. R. Midhun, and R. I. Sujith** (2023). Tipping in complex systems under fast variations of parameters. *Chaos*, **33**(8).
162. **Pavithran, I., V. R. Unni, A. J. Varghese, R. I. Sujith, A. Saha, N. Marwan, and J. Kurths** (2020). Universality in the emergence of oscillatory instabilities in turbulent flows. *EPL*, **129**(2), 24004.
163. **Pawar, S. A., M. Raghunathan, K. Reeja, P. Midhun, and R. I. Sujith** (2021). Effect of preheating of the reactants on the transition to thermoacoustic instability in a bluff-body

- stabilized dump combustor. *Proc. Combust. Inst.*, **38**(4), 6193–6201.
164. **Pawar, S. A., A. Seshadri, V. R. Unni, and R. I. Sujith** (2017). Thermoacoustic instability as mutual synchronization between the acoustic field of the confinement and turbulent reactive flow. *Journal of Fluid Mechanics*, **827**, 664–693.
 165. **Perry, E. H.**, *Investigations of the T-burner and its role in combustion instability studies*. California Institute of Technology, 1970.
 166. **Pikovsky, A., A. Rosenblum, and J. Kurths**, *Synchronization: A Universal Concept in Nonlinear Sciences*. Cambridge University Press, 2003.
 167. **Polifke, W., A. Poncet, C. O. Paschereit, and K. Döbbling** (2001). Reconstruction of acoustic transfer matrices by instationary computational fluid dynamics. *Journal of Sound and Vibration*, **245**(3), 483–510.
 168. **Premraj, D., S. A. Pawar, L. Kabiraj, and R. I. Sujith** (2020). Strange nonchaos in self-excited singing flames. *Europhysics Letters*, **128**(5), 54005.
 169. **Putnam, A. A.**, *Combustion-Driven Oscillations in Industry*. American Elsevier Pub. Co., New York, 1971.
 170. **Rankin, J., M. Desroches, B. Krauskopf, and M. Lowenberg** (2011). Canard cycles in aircraft ground dynamics. *Nonlinear Dyn.*, **66**, 681–688.
 171. **Rayleigh, L.** (1878). The explanation of certain acoustical phenomena. *Nature*, **8**, 319–321.
 172. **Rockwell, D.** (1983). Oscillations of impinging shear layers. *AIAA Journal*, **21**(5), 645–664.
 173. **Rockwell, D. and E. Naudascher** (1979). Self-sustained oscillations of impinging free shear layers. *Annual Review of Fluid Mechanics*, **11**(1), 67–94.
 174. **Romano, M. C., M. Thiel, J. Kurths, I. Z. Kiss, and J. L. Hudson** (2005). Detection of synchronization for non-phase-coherent and non-stationary data. *EPL (Europhysics Letters)*, **71**(3), 466.
 175. **Romano, M. C., M. Thiel, J. Kurths, and W. von Bloh** (2004). Multivariate recurrence plots. *Physics Letters A*, **330**(3-4), 214–223.
 176. **Roy, A., S. Singh, A. Nair, S. Chaudhuri, and R. I. Sujith** (2021). Flame dynamics during intermittency and secondary bifurcation to longitudinal thermoacoustic instability in a swirl-stabilized annular combustor. *Proc. Combust. Inst.*, **38**(4), 6221–6230.
 177. **Roy, R. and K. S. Thornburg Jr** (1994). Experimental synchronization of chaotic lasers. *Physical Review Letters*, **72**(13), 2009.

178. **Sano, M. and T. Oyaizu** (2008). Transition process of frequencies of pure tone caused by vortex shedding in a pipeline containing a double orifice. *Journal of Environment and Engineering*, **3**(2), 228–239.
179. **Saurabh, A., L. Kabiraj, R. Steinert, and C. Oliver Paschereit** (2017). Noise-induced dynamics in the subthreshold region in thermoacoustic systems. *Journal of Engineering for Gas Turbines and Power*, **139**(3), 031508.
180. **Sawyer, R. F.** (2009). Science based policy for addressing energy and environmental problems. *Proceedings of the Combustion Institute*, **32**(1), 45–56.
181. **Schreiber, I. and M. Marek** (1982). Strange attractors in coupled reaction-diffusion cells. *Physica D: Nonlinear Phenomena*, **5**(2-3), 258–272.
182. **Seshadri, A., V. Nair, and R. I. Sujith** (2016). A reduced-order deterministic model describing an intermittency route to combustion instability. *Combust. Theory Model.*, **20**(3), 441–456.
183. **Shanbhogue, S. J., S. Chakravarthy, and R. I. Sujith**, *Aeroacoustics of rocket motors with FINOCYL grain*. AIAA, 2003.
184. **Singh, S., A. Roy, K. V. Reeja, A. Nair, S. Chaudhuri, and R. I. Sujith** (2021). Intermittency, secondary bifurcation and mixed-mode oscillations in a swirl-stabilized annular combustor: Experiments and modeling. *J. Eng. Gas Turbines Power.*, **143**(5), 051028.
185. **Sondhauss, C.** (1854). Ueber die beim ausströmen der luft entstehenden töne. *Annalen der Physik*, **167**(1), 126–147.
186. **Sterling, J. D.** (1993). Nonlinear analysis and modelling of combustion instabilities in a laboratory combustor. *Combustion Science and Technology*, **89**(1-4), 167–179.
187. **Stratonovich, R.**, *Topics in the Theory of Random Noise: General Theory of Random Processes Nonlinear Transformations of Signals and Noise*. Gordon & Breach, 1963.
188. **Stratonovich, R. L.**, *Topics in the Theory of Random Noise*. Gordon and Breach, Science Publishers, New York, 1967.
189. **Strogatz, S. H.**, *Nonlinear Dynamics and Chaos, With Applications to Physics, Biology, Chemistry, and Engineering*. CRC press, Boca Raton, Florida, 2018.
190. **Stubos, A. K., C. Benocci, E. Palli, G. K. Stoubos, and D. Olivari** (1999). Aerodynamically generated acoustic resonance in a pipe with annular flow restrictors. *Journal of Fluids and Structures*, **13**(6), 755–778.
191. **Subramanian, P., S. Mariappan, R. I. Sujith, and P. Wahi** (2010). Bifurcation analysis of thermoacoustic instability in a horizontal Rijke tube. *Int. J. Spray Combust. Dyn.*,

2(4), 325–355.

192. **Sujith, R. I. and S. Pawar**, *Thermoacoustic Instability: A Complex Systems Perspective*. Springer Series in Synergetics. Springer International Publishing, Cham, Switzerland, 2021. ISBN 9783030811341.
193. **Sujith, R. I. and V. R. Unni** (2020). Complex system approach to investigate and mitigate thermoacoustic instability in turbulent combustors. *Physics of Fluids*, **32**(6).
194. **Summerfield, M., E. W. Price, and L. D. Price**, *Nonsteady Burning and Combustion Stability of Solid Propellants*. AIAA, Reston, 1992.
195. **Takens, F.** (1981). Lecture notes in mathematics. by *D. A. Rand and L. S. Young* Springer, Berlin, **898**, 366.
196. **Tandon, S., S. A. Pawar, S. Banerjee, A. J. Varghese, P. Durairaj, and R. I. Sujith** (2020). Bursting during intermittency route to thermoacoustic instability: Effects of slow–fast dynamics. *Chaos*, **30**(10), 103112.
197. **Testud, P., Y. Aurégan, P. Moussou, and A. Hirschberg** (2009). The whistling potentiality of an orifice in a confined flow using an energetic criterion. *Journal of Sound and Vibration*, **325**(4-5), 769–780.
198. **Thonti, B., S. Tandon, P. Durairaj, and R. I. Sujith** (2024). Strange nonchaotic attractor in an unforced turbulent reactive flow system. *Chaos: An Interdisciplinary Journal of Nonlinear Science*, **34**(12).
199. **Tonon, D., A. Hirschberg, J. Golliard, and S. Ziada** (2011). Aeroacoustics of pipe systems with closed branches. *International Journal of Aeroacoustics*, **10**(2-3), 201–275.
200. **Tony, J., E. Gopalakrishnan, E. Sreelekha, and R. I. Sujith** (2015). Detecting deterministic nature of pressure measurements from a turbulent combustor. *Phys. Rev. E*, **92**(6), 062902.
201. **Ushakov, O., H.-J. Wünsche, F. Henneberger, I. Khovanov, L. Schimansky-Geier, and M. Zaks** (2005). Coherence resonance near a hopf bifurcation. *Physical review letters*, **95**(12), 123903.
202. **Varghese, A. J., A. Checkkin, R. Metzler, and R. I. Sujith** (2021). Capturing multifractality of pressure fluctuations in thermoacoustic systems using fractional-order derivatives. *Chaos: An Interdisciplinary Journal of Nonlinear Science*, **31**(3), 033108.
203. **Vishnoi, N., V. Gupta, A. Saurabh, and L. Kabiraj** (2024a). Effect of colored noise on precursors of thermoacoustic instability in model gas turbine combustors. *International Journal of Spray and Combustion Dynamics*, **16**(3), 80–92.
204. **Vishnoi, N., V. Gupta, A. Saurabh, and L. Kabiraj** (2024b). Effect of correlation time

of combustion noise on early warning indicators of thermoacoustic instability. *Chaos: An Interdisciplinary Journal of Nonlinear Science*, **34**(3).

205. **Wang, W., I. Z. Kiss, and J. L. Hudson** (2001). Clustering of arrays of chaotic chemical oscillators by feedback and forcing. *Physical Review Letters*, **86**(21), 4954.
206. **Wang, X., X. Han, H. Song, D. Yang, and C.-J. Sung** (2021). Multi-bifurcation behaviors of stability regimes in a centrally staged swirl burner. *Phys. Fluids*, **33**(9), 095121.
207. **Waugh, I. C. and M. P. Juniper** (2011). Triggering in a thermoacoustic system with stochastic noise. *International journal of spray and combustion dynamics*, **3**(3), 225–241.
208. **Wicker, J. M., W. D. Greene, S.-I. Kim, and V. Yang** (1996). Triggering of longitudinal combustion instabilities in rocket motors-nonlinear combustion response. *Journal of Propulsion and Power*, **12**(6), 1148–1158.
209. **Williamson, C. H. K. and A. Roshko** (1988). Vortex formation in the wake of an oscillating cylinder. *Journal of Fluids and Structures*, **2**(4), 355–381.
210. **Zakharova, A., T. Vadivasova, V. Anishchenko, A. Koseska, and J. Kurths** (2010). Stochastic bifurcations and coherencelike resonance in a self-sustained bistable noisy oscillator. *Physical Review E—Statistical, Nonlinear, and Soft Matter Physics*, **81**(1), 011106.
211. **Zdravkovich, M. M.** (1982). Modification of Vortex Shedding in the Synchronization Range. *Journal of Fluids Engineering*, **104**(4), 513–517.
212. **Zinn, B. T.**, *Pulse Combustion Applications: Past, Present and Future*. Springer Netherlands, Dordrecht, 1996. ISBN 978-94-009-1620-3, 113–137.
213. **Zou, Y., T. Pereira, M. Small, Z. Liu, and J. Kurths** (2014). Basin of attraction determines hysteresis in explosive synchronization. *PRL*, **112**(11), 114102.

CURRICULUM VITAE

NAME Ramesh Siddaruda Bhavi

DATE OF BIRTH 20 August 1996

EDUCATION QUALIFICATIONS

2016 **Bachelor of Engineering (B. E.)**

Institution PES Institute of Technology

Specialization Mechanical Engineering

2024 **M. S. and Ph. D. Dual Degree**

Institution Indian Institute of Technology Madras

Specialization Aerospace Engineering

Registration Date 7th September 2020

DOCTORAL COMMITTEE

Chairperson

Dr. H. S. N. Murthy
Professor and Head
Department of Aerospace Engineering

Guide

Dr. R. I. Sujith
Institute Professor and D. Srinivasan Institute Chair
Professor
Department of Aerospace Engineering

Members

Dr. Sunetra Sarkar
Professor
Department of Aerospace Engineering

Dr. Nagabhushana Rao Vadlamani
Professor
Department of Aerospace Engineering

Dr. Srinivasan K.
Professor
Department of Mechanical Engineering